

Harnessing Data Asymmetry: Manifold Learning in the Finsler World

Thomas Daggès^{1,2,3*} Simon Weber^{2,3,4} Daniel Cremers^{2,3} Ron Kimmel¹

Abstract

Manifold learning is a fundamental task at the core of data analysis and visualisation. It aims to capture the simple underlying structure of complex high-dimensional data by preserving pairwise dissimilarities in low-dimensional embeddings. Traditional methods rely on symmetric Riemannian geometry, thus forcing symmetric dissimilarities and embedding spaces, e.g. Euclidean. However, this discards in practice valuable asymmetric information inherent to the non-uniformity of data samples. We suggest to harness this asymmetry by switching to Finsler geometry, an asymmetric generalisation of Riemannian geometry, and propose a Finsler manifold learning pipeline that constructs asymmetric dissimilarities and embeds in a Finsler space. This greatly broadens the applicability of existing asymmetric embedders beyond traditionally directed data to any data. We also modernise asymmetric embedders by generalising current reference methods to asymmetry, like Finsler t-SNE and Finsler Umap. On controlled synthetic and large real datasets, we show that our asymmetric pipeline reveals valuable information lost in the traditional pipeline, e.g. density hierarchies, and consistently provides superior quality embeddings than their Euclidean counterparts.

1 Introduction

Manifold learning is a core task in data analysis. It seeks low-dimensional representations of high-dimensional data by preserving pairwise dissimilarities, capturing the underlying manifold. Classical methods share a three-stage pipeline: (i) *Data construction* – compute pairwise dissimilarities of data points, (ii) *Embedding definition* – choose how to measure embedding dissimilarities, and (iii) *Optimisation* – optimise the embedding to fit the dissimilarities. As the hidden data manifold is usually Riemannian, these methods target symmetric dissimilarities and embed in a canonical Riemannian space, typically Euclidean.

However, we advocate that, due to the sampling, equipping the manifold with an asymmetric Finsler metric is both more natural, generalising the Riemannian perspective [24], and captures additional valuable information that is lost in the symmetric setting (fig. 1). This novel asymmetric perspective is encouraged after noticing that existing methods construct asymmetric data dissimilarities, undesired when using Riemannian theory, requiring poorly justified post hoc averaging to fix the issue, discarding information in the process.

We thus construct asymmetric data dissimilarities and must then define and optimise their embedding. As Euclidean space is symmetric, it cannot represent asymmetry, so classical methods would fail. Recently, it was suggested to embed asymmetric data to a canonical Finsler space via Finsler MDS [37], but it is limited to oracle asymmetric data only. Thanks to our asymmetric data construction, we greatly broaden its, and

*✉ tom.dages@tum.de

¹Technion – Israel Institute of Technology

²Technical University of Munich

³Munich Center for Machine Learning

⁴University of Oxford

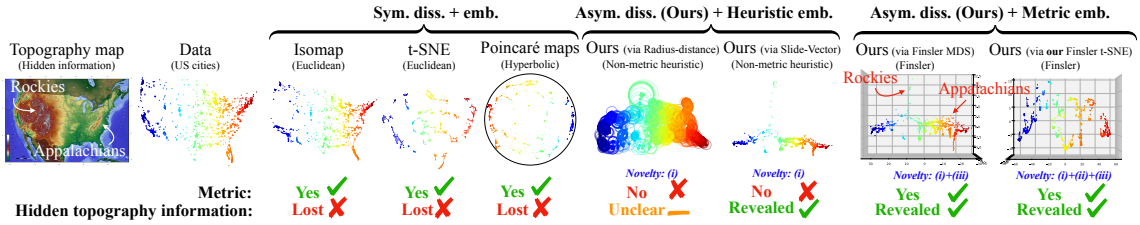


Figure 1: Motivation: how asymmetry can arise and why preserving it matters. We aim to recover the underlying smooth US manifold from US cities (latitude-longitude). Hidden external factors (e.g. mountain ranges) bias the sampling density: fewer cities lie in high-altitude regions. Reweighting distances by local density yields asymmetric dissimilarities that encode differences in geographical setting. Symmetrising and embedding in symmetric spaces (e.g. Isomap, t-SNE, Umap, Poincaré maps) discards this information. Our asymmetric dissimilarity construction can be fed to existing traditional asymmetric embedders (e.g. slide-vector, radius-distance), but these are heuristic and non-metric. Finsler geometry provides a principled metric framework, enabling the existing Finsler MDS [37] and our novel and more scalable Finsler t-SNE and Umap to better embed and reveal the hidden terrain.

generally any asymmetric embedder’s, applicability to any data. Additionally, Finsler MDS’ optimizer is slow, unstable, unscalable, and without extra perks like clustering. We propose to overcome these issues by adapting modern methods, like references t-SNE [77] and Umap [81], to asymmetry. Our contributions are as follows:

- (a) Reveal theory inconsistency in classical *data construction* and give a principled remedy towards avoiding asymmetry.
- (b) Embrace sampling-induced asymmetry in *data construction* via a Finsler lens, enriching our view on sampled data with information that symmetric methods cannot capture, and opening up applications of asymmetric methods, e.g. Finsler MDS, even to traditionally symmetric data.
- (c) Embed arbitrary data in the canonical Finsler space (Finsler *embedding definition* and *optimisation* stages). We generalise modern optimisation-based methods to asymmetric data and Finsler embeddings, and introduce in particular Finsler t-SNE and Finsler Umap.
- (d) We experimentally demonstrate the advantage of our asymmetric Finsler pipeline. Through visualisations, we show that Finsler embeddings not only recover the hidden manifold structure but also reveal additional information hidden in the sampling-induced asymmetry. In extensive classification benchmarks, we consistently outperform Euclidean baselines on label-related clustering metrics revealing the superior quality of our embeddings.

2 Related works

Our work blends manifold learning with Finsler geometry.

Manifold learning. This classical field [108, 68, 46, 120] seeks low-dimensional embeddings preserving pairwise dissimilarities [103]. The many methods are often grouped by whether they preserve structure locally [101, 43, 129, 6, 7, 131, 31, 30, 73, 74, 111, 52, 78, 112, 81, 118, 75], globally [122, 123, 14, 50], or both [92, 56, 104, 106, 114, 77, 16, 99, 1, 90, 105, 13, 62, 63, 65]. Most assume symmetric dissimilarities, excluding asymmetric data such as directed graphs or physical systems. Fewer works tackle asymmetry, either by artificially reweighting symmetric dissimilarities or leaving the metric setting. Traditionally,

they either a) decompose separately symmetric and skew-symmetric parts (ASYMSCAL [25, 26], Gower [32, 53]), or b) add per-point objects [126, 78, 53, 88, 113], e.g. circles in radius-distance models that add to the Euclidean embedding dissimilarity the difference in radius of each point’s circle [88, 113], or c) use global-vectors [72, 12, 89], e.g. in the slide-vector model [72] embedding dissimilarities are the Euclidean distance between a non-perturbed embedding point and a globally shifted one. These asymmetric embedders are not only heuristic but also non-metric, as for instance embeddings are not guaranteed to vary faithfully with data dissimilarity changes.

Recently, Finsler MDS [37] extended classical Multi-Dimensional Scaling (MDS) [108, 68, 35] to metric handling of asymmetric dissimilarities via Finsler geometry, but it targets inherently asymmetric data (e.g. current flows on a river) and was not made applicable to general datasets (e.g. images) usually treated as symmetric. It also relies on classical MDS rather than modern scalable methods like t-SNE [77] and Umap [81]. Beyond [37], we construct asymmetric dissimilarities on any data (i), unlocking all asymmetric embedders to any data, accelerate Finsler MDS optimisation (iii), and extend modern reference methods, e.g. t-SNE and Umap, to asymmetry (ii)-(iii), enabling large-scale embedding. To the best of our knowledge, no prior work, including [37], extends modern methods like t-SNE and Umap to asymmetric data, scales to large asymmetric datasets, or builds asymmetric dissimilarities on any data (e.g. image datasets).

Finsler computer vision. Finsler geometry [87, 5, 85, 11] provides a theoretical asymmetry framework. Remarkably, it has been largely unexplored in computer vision, with rare exceptions in robotics [96], image processing [21, 20, 23, 22, 125, 36], shape analysis [121], and manifold learning [37].

3 The traditional manifold learning pipeline

The goal of manifold learning is to find an embedding $y_1, \dots, y_N \in \mathbb{R}^m$ of N points $x_1, \dots, x_N \in \mathbb{R}^n$ into a low-dimensional space, i.e. $m < n$, while preserving a collection of data dissimilarities $\mathbf{D} \in \mathbb{R}_+^{N \times N}$. The original points x_i are often assumed to lie on a manifold $\mathcal{X} \subset \mathbb{R}^n$, equipped with a metric L given at point x on its tangent plane $\mathcal{T}_x \mathcal{X}$ by $L_x : \mathcal{T}_x \mathcal{X} \rightarrow \mathbb{R}_+$ and defining the concept of distance and in turn geodesic distance $d_L : \mathcal{X} \times \mathcal{X} \rightarrow \mathbb{R}_+$.

A major assumption in traditional techniques is that the dissimilarities are symmetric $\mathbf{D} = \mathbf{D}^\top$, as the metric L of the underlying manifold \mathcal{X} is naturally symmetric for most datasets consisting in a collection of independently sampled points, e.g. image classification datasets. As such, the data manifold is often assumed to be Riemannian and is to be embedded into a Riemannian space \mathbb{R}^m .

Riemannian manifolds. The manifold \mathcal{X} is Riemannian if it is equipped with a Riemannian metric R , which has quadratic form $R_x(u) = \sqrt{u^\top M(x)u} = \|u\|_{M(x)}$. The positive definite matrix $M(x)$ is the metric tensor and fully describes the metric. These metrics are symmetric as $R_x(-u) = R_x(u)$ for any tangent vector u . By integrating the length of infinitesimal tangent vectors $R_x(\gamma'(t)dt)$ of curves $\gamma(t)$ on \mathcal{X} , the Riemannian length of a curve is independent of its traversal direction, making Riemannian geodesic distances also symmetric.

In addition to dimensionality reduction, we usually aim to flatten the embedded data manifold in \mathbb{R}^m to show the simple intrinsic nature of the original data manifold \mathcal{X} . We thus opt for canonical embedding spaces with simple geometry, having geodesic curves given by the usual straight segments and simple closed formulas for distance calculations. The canonical Riemannian space is the Euclidean space, with distances computed in \mathbb{R}^m as $d_E(y_i, y_j) = \|y_j - y_i\|_2$.

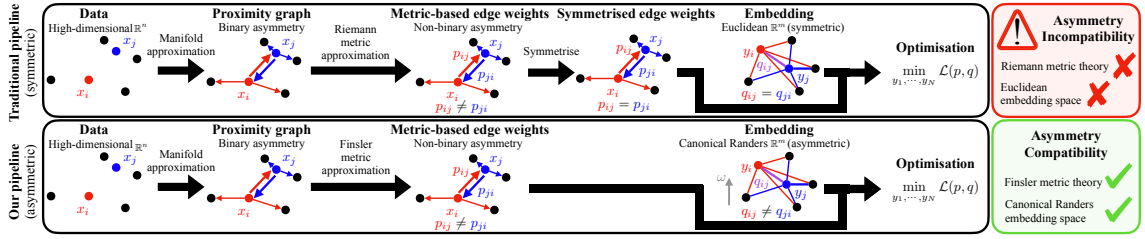


Figure 2: The traditional manifold learning pipeline leads to asymmetric data dissimilarities on sampled data due to directed proximity graphs and local distance transforms. As this violates the Riemannian manifold assumption and is incompatible with symmetric Euclidean space embeddings, heuristic symmetrisation of data dissimilarities is required yet theoretically unjustified. We propose to equip the data manifold with a Finsler metric allowing asymmetric dissimilarities. Embeddings are then performed in a canonical Finsler space, enabling us not only to accurately capture the structure of the data but also harness and reveal the natural asymmetry of the sampling.

Data construction. Traditional manifold learning methods follow a shared pipeline (see fig. 2). First, the smooth manifold is discretely approximated on the provided samples by a proximity graph, e.g. the universal kNN, radius, or rarer adaptive graphs [51, 115, 60, 34, 127, 33, 4, 44, 2, 130, 83, 3, 9, 8, 10, 59, 132], based on the ambient Euclidean distance. Taking the manifold metric as the Euclidean distance along close points, i.e. graph edges, $L_{x_i}(x_j - x_i) \approx \|x_j - x_i\|_2$ approximates in the first order the graph edges $x_j - x_i$ to lie on the tangent plane $\mathcal{T}_{x_i}\mathcal{X}$. Modern methods often tweak the metric to a new Riemannian metric R accounting for local sampling disparities, typically $R_{x_i}(x_j - x_i) \approx \frac{1}{\sigma_i}\|x_j - x_i\|_2$ with σ_i estimated from local densities. Data dissimilarities p_{ij} are then built by optionally remapping distances via a transformation h^p : $p_{ij} = h^p(R_{x_i}(x_j - x_i))$, in other words $p_{ij} = h_i^p(\|x_j - x_i\|_2)$ ¹. Commonly if j neighbours i ,

$$p_{ij} = \underbrace{\|x_j - x_i\|_2}_{\text{MDS [106], Isomap [114]}}; \underbrace{\text{SM}\left(-\frac{\|x_j - x_i\|_2^2}{2\sigma_i^2}\right)}_{\text{t-SNE [77]}}; \underbrace{e^{-\frac{\|x_j - x_i\|_2 - \rho_i}{\sigma_i}}}_{\text{Umap [81]}} \quad (1)$$

where ρ_i is another local estimate and SM is the softmax. If i does not conversely neighbour j , then p_{ji} is undefined. Populating the graph weights p_{ij} into a matrix provides the sparse dissimilarity matrix \mathbf{D} . Modern methods (t-SNE, Umap) use the sparsity for computational efficiency. Earlier works (MDS, Isomap), geodesically extend \mathbf{D} into a dense matrix with Dijkstra’s algorithm [41] on the neighbourhood graph to account for long range behaviours. But this operation is costly as it requires fixing the connectivity, and lengths of shortest paths are overestimated due to undersampling, requiring expensive additional effort to filter only consistent shortest paths [16, 15, 17, 105, 98, 99, 13]. Directed neighbourhood graphs like kNN lead to binary asymmetry² due to missing reverse edges. Local metric tweaking of R , with transforms h_i^p depending on i , yield “incompatible” [81] weights p_{ij} with non-binary asymmetry³, see fig. 3. As asymmetry violates the Riemannian assumption, the p_{ij} are arbitrarily symmetrised, commonly⁴

$$p_{ij} \leftarrow \underbrace{\frac{p_{ij} + p_{ji}}{2}, \max(p_{ij}, p_{ji})}_{\text{Classical MDS, Isomap}}; \underbrace{\frac{p_{ij} + p_{ji}}{2N}}_{\text{t-SNE}}; \underbrace{p_{ij} + p_{ji} - p_{ij}p_{ji}}_{\text{Umap}}. \quad (2)$$

Embedding definition. The canonical Riemannian embedding space is Euclidean, thus embedding distances are given by $d_{ij} \triangleq d_E(y_i, y_j) = \|y_j - y_i\|_2$, which can be transformed

¹And optional extra i -based transforms, e.g. Umap’s distance threshold.

²In binary asymmetry, either $p_{ij} = p_{ji}$ or one of them is undefined.

³In non-binary asymmetry, $p_{ij} \neq p_{ji}$ yet both are defined.

⁴If p_{ij} is defined but not p_{ji} , then p_{ji} is treated as 0 in symmetrisation.

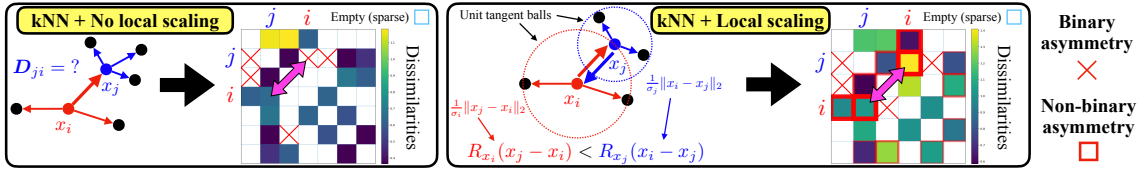


Figure 3: Left: binary asymmetry from absent reverse edges in directed proximity graphs. Right: non-binary asymmetry with reciprocal edges having differing distances from locally tweaking the metric and approximating geodesic with tangent space distances.

to dissimilarities $q_{ij} \leftarrow h^q(\|y_j - y_i\|_2)$, commonly

$$q_{ij} = \underbrace{d_{ij} \triangleq \|y_j - y_i\|_2}_{\text{MDS, Isomap}}; \underbrace{\frac{1}{\mathcal{Z}_y} (1 + \frac{d_{ij}^2}{\nu})^{-\frac{\nu+1}{2}}}_{\text{t-SNE}}; \underbrace{(1 + ad_{ij}^{2b})^{-1}}_{\text{Umap}}, \quad (3)$$

with parameters ν [117], a , and b and normalisation \mathcal{Z}_y . The q_{ij} are computed for all pairs and are symmetric (Euclidean space): h^q is independent of i .

Optimisation. An objective $\mathcal{L}(p, q)$ is minimised, e.g.

$$\mathcal{L} = \underbrace{\text{MSE}_w(p, q)}_{\text{MDS, Isomap}}; \underbrace{\text{KL}(p \parallel q)}_{\text{t-SNE}}; \underbrace{\text{CE}(p, q)}_{\text{Umap}}, \quad (4)$$

where KL, CE, and MSE_w are the KL-divergence [69], cross-entropy, and mean squared error with optional weights w to focus only on consistent pairs [99, 105, 13]. MDS is solved by iterative minimisation via the SMACOF algorithm [39, 12], but the cheaper kernel PCA (Isomap) is usually done in practice⁵. Gradient descent is done in t-SNE and Umap (with negative sampling for Umap). Efficient implementations, which are crucial for large datasets, require explicit closed-form gradient and update rules⁶ (section A.2).

4 Limitations of traditional manifold learning

We argue in this work that there are two fundamental issues with traditional methods relating to Riemannian metrics: (i) the *data construction* methodology cannot be Riemannian as it leads to asymmetry, and (ii) asymmetry is incompatible with the Euclidean *embedding definition* and *optimisation*. Also, symmetry discards information on the sampling itself.

Non-Riemannian methodology. A major issue with existing methods, claiming to be Riemannian, is that the *data construction* leads to asymmetric dissimilarities. This is prohibited in Riemannian geometry as Riemannian metrics are symmetric. Rather than switching to asymmetric tools, like Finsler geometry, that would account for the natural asymmetry of the data, unjustified heuristic fixes symmetrise them (eq. (2)), discarding information in the process. Yet even from a Riemannian perspective, this symmetrisation is problematic. While it can be acceptable for binary asymmetry, as it converts the directed neighbourhood graph to another valid undirected one, it is highly problematic with non-binary asymmetry, which we now focus on. The issue arises from combining local metric tweaking $R_{x_i}(x_j - x_i) = c(x_i)\|x_j - x_i\|_2$, e.g. $c(x_i) = \frac{1}{\sigma_i}$ (manifold with non-uniform isotropic metric $M(x) = c(x)I$), with approximating geodesic distances between close points with tangent space distances, $d_R(x_i, x_j) \approx R_{x_i}(x_j - x_i)$, leading to $p_{ij} = h^p(R_{x_i}(x_j - x_i))$. Since R is Riemannian, it must have symmetric manifold distances $d_R(x_i, x_j) = d_R(x_j, x_i)$. Yet tangent space distances R_{x_i} and R_{x_j} can greatly

⁵In Isomap, $w_{ij} = 1$ and distances p_{ij} , q_{ij} are squared in the objective.

⁶We found an error in the update rule of t-SNE with ν d.o.f. [117] that is also present in reference toolkits and libraries like Scikit-learn [93], see section A.2.1 and theorem 3.

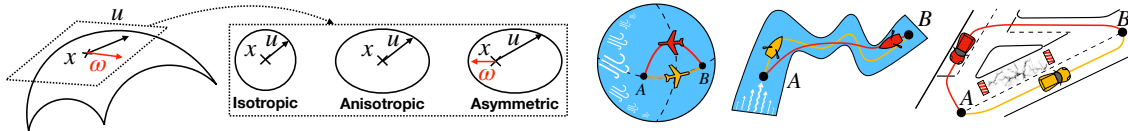


Figure 4: Metrics define distances in tangent spaces (left) via their convex unit tangent ball. Riemannian metrics – whether isotropic or anisotropic – remain symmetric due to symmetric unit tangent balls. Finsler metrics allow asymmetry, so geodesic paths and distances need not be symmetric (right). Courtesy of [121, 37, 36].

vary in non-uniform metrics, even between close points, if the local scaling $c(x_i)$ and $c(x_j)$ does. This problematic yet universal methodology puts into question the claimed rigorous Riemannian theoretical foundations existing methods might rely on, even when trying to justify post hoc symmetrisation fixes (eq. (2)) with layers of complex theory⁷. However, with our rigorous metric analysis and understanding of the logical flaw, we provide a novel Riemannian theory-justified methodology towards fixing the issue. The idea is that linear interpolation of the metric along the edge leads to replacing σ_i by the harmonic mean of σ_i and σ_j (see theorem 4 and corollary 1 in section B). While theoretically grounded, our Riemannian remedy avoiding asymmetry still loses important information compared to an asymmetric perspective: the asymmetric disparities from the sampling itself, e.g. from disparate sampling densities. Such important information is lost in all symmetric settings (see fig. 1). From now on, we propose to preserve this information and thus suggest to work with the naturally arising asymmetric dissimilarities $\mathbf{D}^\top \neq \mathbf{D}$, which requires to drop the Riemannian tools for asymmetric-compatible ones.

Incompatibility with asymmetry. Traditional pipelines assume symmetric dissimilarities $\mathbf{D}^\top = \mathbf{D}$ to embed data in the symmetric canonical Euclidean space \mathbb{R}^m (*embedding definition* and *optimisation* stages). As such, traditional Euclidean embedding methods would simply crash or at best discard the naturally arising asymmetry, losing the extra information on the discrete sampling distribution. Recently, [37] proposed Finsler geometry for asymmetry by replacing in the *embedding definition* the Euclidean with the asymmetric canonical Randers space \mathbb{R}^m . However, this method was only applicable to data with given asymmetry, like digraphs or physical systems with currents, but not arbitrary datasets traditionally considered symmetric yet having natural asymmetry as we have discussed (absent *data construction* stage to get asymmetric dissimilarities). Also, this method is slow and numerically unstable (*optimisation* stage). Additionally, it does not possess the benefits of recent reference symmetric methods, e.g. t-SNE or Umap, providing high speeds, numerical stability, and clustering properties. It is thus desirable to adapt the modern reference techniques to handle asymmetric data.

5 Asymmetric manifold learning

In this paper, we suggest to embrace the natural asymmetry arising from traditional pipelines. To do so, we need to drop the reliance on Riemannian geometry and work with its asymmetric generalisation instead: Finsler geometry.

Finsler geometry. Finsler manifolds [5] generalise Riemannian ones [24] and allow asymmetry. Such manifolds \mathcal{X} are equipped with a Finsler metric F , with $F_x : \mathcal{T}_x\mathcal{X} \rightarrow \mathbb{R}_+$ such that $F_x(u) = 0$ if and only if $u = 0$, it follows the triangular inequality, and is positive-homogeneous, i.e. $F_x(\lambda u) = \lambda F_x(u)$ for any $\lambda > 0$. Many families of parametric Finsler metrics exist [61, 79, 95, 80, 67]. We work with the common [121, 37, 36] Randers metric [95] for simplicity, $F_x(u) = \|u\|_{M(x)} + \omega(x)^\top u$ with $\|\omega(x)\|_{M^{-1}(x)} < 1$, where the

⁷Such as the probabilistic union averaging with fuzzy logic in Umap.

added linearity to a Riemannian part breaks the symmetry. Note that Riemannian metrics have $\omega \equiv 0$.

To embed asymmetric data in \mathbb{R}^m , [37] recently proposed to replace the canonical Riemannian metric (Euclidean) with a canonical Randers metric F^C having constant ω , typically chosen along the last dimension, perturbing the Euclidean metric: $F_x^C(u) = \|u\|_2 + \omega^\top u$. Note that it becomes Euclidean when $\omega = 0$ and is flat just like it as geodesics are the usual Euclidean segments. However, their lengths depend on the traversal direction, with a simple closed-form expression $d_{FC}(x, y) = \|y - x\|_2 + \omega^\top (y - x)$. Schematically, the canonical Randers space combines a Riemannian hyperplane \mathbb{R}^{m-1} with an orthogonal direction of asymmetry ω . For symmetric data, the embedding collapses to the $m - 1$ hyperplane. It is thus recommended to compare asymmetric embeddings to the canonical Randers space \mathbb{R}^{m+1} to symmetric embeddings in \mathbb{R}^m [37].

Canonical Randers space embeddings were found in [37] by replacing the Euclidean distances $q_{ij} = d_{ij}$ by the Finsler ones $q_{ij}^F = d_{FC}(y_i, y_j) \triangleq d_{ij}^F$, and minimising the MSE loss by the Finsler SMACOF algorithm. However, this algorithm is slow and memory expensive due to reshaping linear systems of equations to $N^2 \times N^2$ matrices, with unstable pseudo-inverse calculations in practice (unlike the original SMACOF). Although it theoretically handles asymmetry, it does not use any of the modern manifold learning knowledge for harnessing sparse dissimilarities and fast calculations as in t-SNE or Umap, which also provide scalability and clustering properties. Additionally, [37] did not provide any way to apply their method to traditionally considered symmetric manifolds, e.g. image datasets, drastically limiting their application scope to physically asymmetric data like current maps or small digraphs.

From symmetric to asymmetric manifolds. We now return to the traditional manifold learning pipeline and its *data construction*. Asymmetry naturally arose when combining local Riemannian metric tweaking with approximating geodesic with tangent lengths. Although it is an issue for Riemannian geometry, it naturally fits in a Finsler perspective, which we propose to adopt. This process in fact equips the data manifold \mathcal{X} with a Finsler metric F , where *geodesic* distances between close points are given by the scaled Riemannian *tangent* lengths $d_F(x_i, x_j) = R_{x_i}(x_j - x_i)$. We thus propose to keep the computed asymmetric dissimilarities $p_{ij} = h^p(R_{x_i}(x_j - x_i)) = h_i^p(\|x_j - x_i\|_2)$ without artificial symmetrisation. We can optionally extend p_{ij} geodesically on the directed neighbourhood graph if a dense dissimilarity matrix \mathbf{D} is needed, otherwise p_{ij} form a sparse \mathbf{D} . Should they be symmetric, i.e. R is uniform and h_i^p is independent of i , then the data manifold \mathcal{X} is equipped with a symmetric metric and symmetric Euclidean embeddings should be done. If not, then we should embed the Finsler manifold \mathcal{X} to an asymmetric Finsler space, e.g. the canonical Randers space. Switching to Finsler metrics not only resolves the theoretical issue with the traditional methodology, its bypassing of symmetrisation preserves valuable natural asymmetric information that encodes the sampling, e.g. density disparities.

Finsler manifold learning. We propose to generalise existing symmetric manifold learning methods to asymmetric data and Finsler embeddings while preserving their unique advantages and characteristics (*embedding definition* and *optimisation* stages). Our extension is general and can be applied to most methods, yet we focus as examples on the references t-SNE and Umap. Given traditional methods with symmetric embedding dissimilarities $q_{ij} = h^q(\|x_j - x_i\|_2)$ and Riemannian objectives $\mathcal{L}(p, q)$, we propose to generalise them to Finsler methods by embedding into the canonical Randers embedding space with asymmetric embedding dissimilarities $q_{ij}^F = h^q(d_{FC}(x_j - x_i))$, e.g.

$$q_{ij}^F = \underbrace{d_{ij}^F}_{\text{Finsler MDS [37]}} ; \underbrace{\frac{1}{z_y^F} \left(1 + \frac{(d_{ij}^F)^2}{\nu}\right)^{-\frac{\nu+1}{2}}}_{\text{Finsler t-SNE}} ; \underbrace{(1 + a(d_{ij}^F)^{2b})^{-1}}_{\text{Finsler Umap}}, \quad (5)$$

and then minimise the Finsler objective $\mathcal{L}(p, q^F)$, e.g.

$$\mathcal{L} = \underbrace{\text{MSE}_w(p, q^F)}_{\text{Finsler MDS [37]}}; \underbrace{\text{KL}(p \| q^F)}_{\text{Finsler t-SNE}}; \underbrace{\text{CE}(p, q^F)}_{\text{Finsler Umap}}. \quad (6)$$

Analysis of Euclidean objectives yields their minimisation⁸. Similar analysis of Finsler objectives generalises the update rules⁹. In t-SNE and Umap, explicit gradients are needed for efficient implementations in optimised code languages. Remarkably, gradients of canonical Finsler distances also share the same antisymmetry as Euclidean ones (theorem 5, section C), suggesting beyond the arguments in [37] that this is the proper generalisation of the Euclidean space. Calculations provide explicit gradients (theorems 1 and 2). Of note, updates are no longer just a combination of (asymmetric) forces along the rays connecting points, but also of external current forces¹⁰. The update rules then follow gradient descent with any optional tricks from the Euclidean methods, e.g. negative sampling [84, 112] for (Finsler) Umap.

Theorem 1 (Finsler t-SNE). *Let $\mathcal{L} = -\sum_{ij} p_{ij} \ln q_{ij}^F$ be the Finsler t-SNE loss with q_{ij}^F from eq. (5). Denoting $t_{ij}^F = (1 + \frac{(d_{ij}^F)^2}{\nu})^{-1}$ and $\delta_{pq^F}^{ij} = p_{ij} - q_{ij}^F$, then*

$$\frac{\partial \mathcal{L}}{\partial y_i} = \frac{\nu + 1}{\nu} \sum_j \left(\left[\delta_{pq^F}^{ij} t_{ij}^F \frac{d_{ij}^F}{d_{ij}} + \delta_{pq^F}^{ji} t_{ij}^F \frac{d_{ij}^F}{d_{ij}} \right] (y_i - y_j) + \left[-\delta_{pq^F}^{ij} t_{ij}^F d_{ij}^F + \delta_{pq^F}^{ji} t_{ij}^F d_{ij}^F \right] \omega \right).$$

Theorem 2 (Finsler Umap). *Let $\mathcal{L} = -\sum p_{ij} \ln q_{ij}^F + (1 - p_{ij}) \ln(1 - q_{ij}^F)$ be the Finsler Umap loss with q_{ij}^F from eq. (5). Denoting $c_{ij}^a = -\ln q_{ij}^F$ and $c_{ij}^r = -\ln(1 - q_{ij}^F)$ to be the asymmetric attractive and repulsive forces and $b' = 2b - 1$, then $\frac{\partial c_{ij}^a}{\partial y_i} = -\frac{\partial c_{ij}^a}{\partial y_j}$ and $\frac{\partial c_{ij}^r}{\partial y_i} = -\frac{\partial c_{ij}^r}{\partial y_j}$ with*

$$\frac{\partial c_{ij}^a}{\partial y_i} = 2ab \frac{(d_{ij}^F)^{b'}}{d_{ij}} q_{ij}^F (y_i - y_j) - 2ab (d_{ij}^F)^{b'} q_{ij}^F \omega \quad \text{and} \quad \frac{\partial c_{ij}^r}{\partial y_i} = \frac{-2b q_{ij}^F}{d_{ij} d_{ij}^F} (y_i - y_j) + \frac{2b q_{ij}^F}{d_{ij}^F} \omega.$$

Proof. We prove Theorems 1 and 2 in section C. □

Combining Finsler data and embedding perspectives. For any dataset, we can combine both our asymmetric understanding of the input data manifold, with extracted asymmetric dissimilarities $\mathbf{D} \neq \mathbf{D}^\top$, and our generalisation of existing manifold learning methods to Finsler embeddings. To the best of our knowledge, we are the first to provide this perspective. In particular, [37] proposed a Finsler embedding method for given asymmetric data, like physical systems or digraphs, but did not propose ways to find asymmetry on arbitrary datasets, like collections of images.

6 Experiments

We provide qualitative and quantitative experiments to showcase our approach. Full details – data, implementation, results – are in the appendix (sections E and F).

⁸Like closed-form spectral solutions (Isomap), advanced optimisation algorithms (SMACOF), or gradient descent and variants (t-SNE, Umap).

⁹Note that closed-form spectral solutions often do not generalise in the Finsler setting. More expensive iterative alternatives, e.g. the Finsler SMACOF or gradient descent procedures, are then necessary (see section D).

¹⁰This echoes the time dynamics in currents, e.g. boats on a river, given by the Zermelo metric, which is a Randers metric [128, 107, 37].

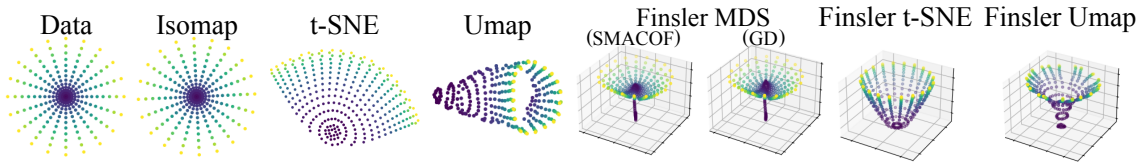


Figure 5: Toy planar data with non-uniform density, embedded with symmetric baselines and our Finsler methods using asymmetric dissimilarities. Variation in the z coordinate reveals asymmetric distances that quantitatively encode density differences, while a top view (xy only) preserves the manifold as in Isomap.

6.1 Synthetic datasets

As high-dimensional data is often sampled from unknown incomprehensible manifolds, evaluating embeddings is non-trivial. It is standard in the field to test new methods on synthetic data whose underlying manifold is known and understood. Such mandatory experiments offer fundamental insight into the quality of embeddings and how well they preserve manifolds. We test several synthetic setups.

6.1.1 Planar manifold.

Data. We use $N = 300$ points on the unit Euclidean disk in \mathbb{R}^2 , sampled on a uniform polar grid. In Cartesian coordinates this yields non-uniform density (denser at the centre).

Methods. We embed with symmetric baselines (Isomap, t-SNE, Umap) in \mathbb{R}^m with $m = 2$, matching the manifold dimension of \mathcal{X} . Following [37], Finsler embeddings use the canonical Randers space $\mathbb{R}^{m+1} = \mathbb{R}^3$ with an extra coordinate to encode asymmetry. To reveal density disparities, we use methods in our asymmetric pipeline (Finsler MDS, Finsler t-SNE, and Finsler Umap). Note that without our pipeline, the original Finsler MDS [37] would not run here as they did not provide ways to compute asymmetric dissimilarities on such data. We also run the original Finsler SMACOF and a new solution with gradient-descent (GD) on the Finsler stress, which scales to larger N and avoids pseudo-inverse instabilities we found in Finsler SMACOF.

Results. Although the underlying manifold is the Euclidean disk, asymmetric density-dependent dissimilarities p_{ij} endow it with a Finsler metric: higher local densities (lower σ_i) increase p_{ij} , so going from dense to sparse regions costs more than the reverse. Embedding with our asymmetric p_{ij} in the canonical Randers space exposes this (see fig. 5): high-density areas are mapped to lower z than sparse ones, while the disk geometry is preserved in top-down views along xy hyperplanes orthogonal to ω (upwards z axis). This density information is lost in symmetric embeddings. Isomap preserves the disk but does not explicitly reveal density variation, while the references t-SNE and Umap poorly represent the data. We rule out an artifact from the extra Randers coordinate by giving Euclidean (resp. Finsler) methods an extra (resp. minus) embedding dimension (section F.1.2). At larger N (section F.1.1), we see limits of Finsler MDS, the local asymmetric nature of purely local methods (Finsler Umap), and confirm that t-SNE outperforms Umap but is slower (Euclidean and Finsler).

6.1.2 Curved manifold.

Data. The data is $N \approx 2000$ points sampled on the Swiss roll: an intrinsically flat 2D manifold embedded in \mathbb{R}^3 with extrinsic curvature. Points are obtained by regular sampling of the unit square, then mapped to the rolled surface. This yields higher sample density where mean curvature is larger (toward the roll’s inside). See section E.1.2 for details.

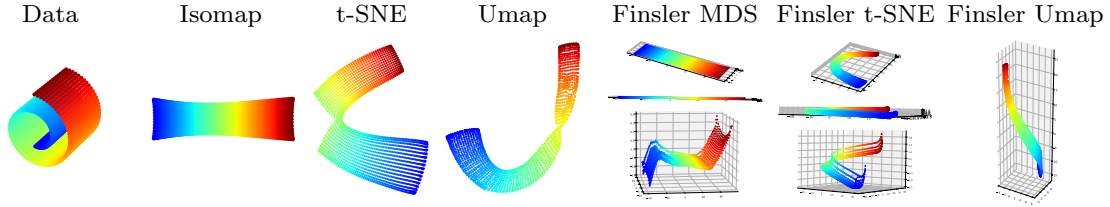


Figure 6: Swiss roll embeddings. Euclidean baselines aim only to preserve the manifold, with debatable success. Our asymmetric Finsler embeddings additionally reveal density asymmetry: dense points (blue) are embedded lower than sparse ones (red). For Finsler MDS and t-SNE we show, top to bottom, the embedding with equal axes, a rotated side view, and an unequal-axes view that magnifies height differences.

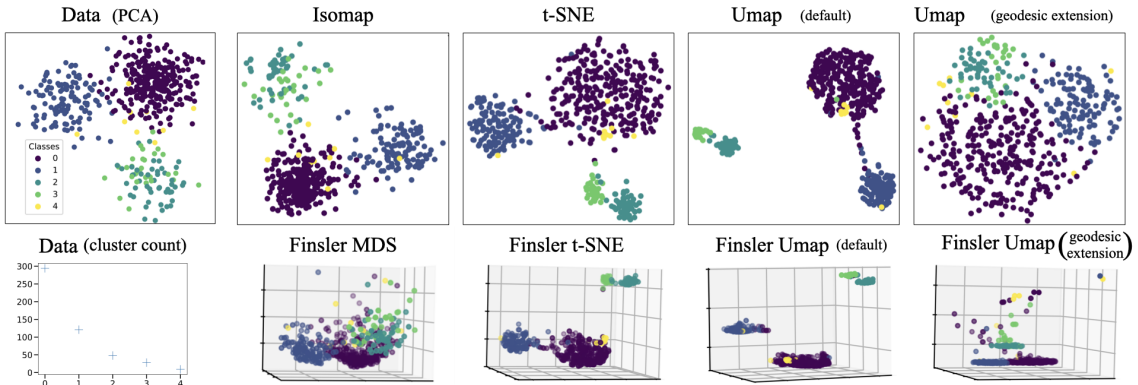


Figure 7: Our Finsler approach clusters and reveals cluster hierarchy, as sparser clusters are embedded higher. This is shown either locally (Finsler t-SNE, default Finsler Umap) or globally (Finsler MDS, extended Finsler Umap), and is absent in Euclidean methods.

Methods. We embed the Swiss roll with Isomap, t-SNE, and Umap (resp. Finsler MDS-GD, t-SNE, and Umap) in \mathbb{R}^2 (resp. \mathbb{R}^3). To enhance manifold preservation in (Finsler) Umap, we geodesically extend distances d_{ij} in the kNN graph ($k = 15$) and keep the 50 smallest edges per node to get a sparse graph.

Results. Our Finsler embeddings visually expose the density asymmetry: denser regions map lower than sparse ones (see fig. 6). In contrast, Euclidean methods do not reveal it, whether preserving the manifold (Isomap) or not (t-SNE, Umap). Finsler Umap highlights the asymmetry more than Finsler MDS and t-SNE, whose embeddings are near-flat and almost orthogonal to the z axis of asymmetry. Thus, our approach not only recovers the band-like structure in top-down views similar to Euclidean mappings but also adds density-based information lost in Euclidean methods.

Clustered manifold. In fig. 7, we demonstrate that our method can not only accurately cluster high-dimensional data, it also provides a semantic hierarchy between clusters based on their density. See section F.2 for full details.

6.2 Real datasets

6.2.1 US Cities.

As a warm-up, we embed $N = 2000$ mainland US cities (lat–lon) from US Zip codes [116] (fig. 1). Although altitude is absent from input coordinates, it biases city density and is thus encoded in asymmetric relationships in city densities. Symmetrising discards this information. As expected, symmetric Isomap, t-SNE (Euclidean), Poincaré maps

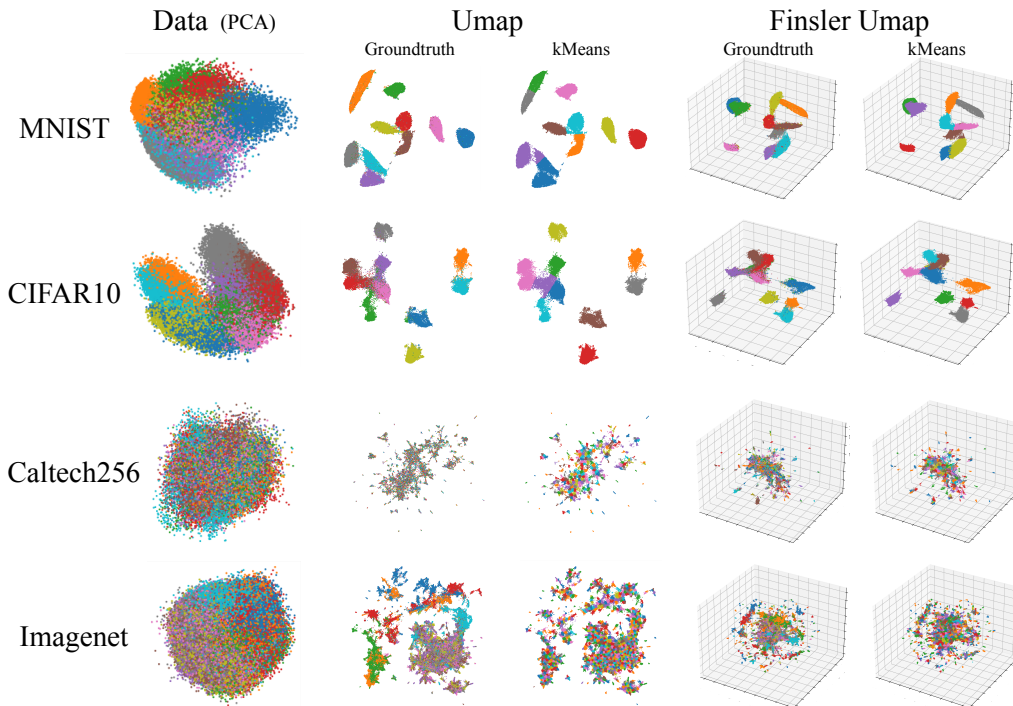


Figure 8: Embedding results on large classification datasets using the traditional Euclidean or our Finsler Umap. Using kMeans clustering on our Finsler embeddings more accurately matches groundtruth labels, implying that our Finsler pipeline not only reveals additional asymmetry information, but it also better preserves the data.

(Hyperbolic) [65] miss it, whereas asymmetric models – radius-distance, slide-vector, Finsler MDS, our Finsler t-SNE –, enabled here thanks to our *data construction*, preserve and reveal it.

6.2.2 Classification datasets.

The standard manifold learning test evaluates label alignment in unsupervised embeddings of classification datasets. Methods favouring clustering (t-SNE, Umap) over manifold preservation (classical MDS) tend to produce label-aligned clusters. Quality scores are estimated by clustering the embedding, e.g. kMeans [110, 76, 82, 48], and measuring overlap with groundtruth labels. Label-agnostic scores also exist to see if clusters are well-behaved, but nice-looking cluster shapes are unrelated to the data manifold, making them unreliable as embedding quality measurements.

Data. We evaluate 16 reference benchmarks: 1 tabular dataset (Iris) and 15 image datasets spanning various resolution, colour, size, and complexity (MNIST, Fashion-MNIST, Kuzushiji-MNIST, EMNIST, EMNIST-Balanced, CIFAR10, CIFAR100, DTD, Caltech101, Caltech256, OxfordFlowers102, Oxford-IIIT Pet, GTSRB, Imagenette, ImageNet). We do not subsample, e.g. we embed over one million images for ImageNet. As vanilla t-SNE [77] is slow, we ran it and its Finsler variant only on the smaller datasets. See section E.1.4 for details.

Scores. We use the Adjusted Mutual Information (AMI) [119], Adjusted Rank Index (ARI) [58], Normalized Mutual Information (NMI) [119], Homogeneity (HOM) [97], Completeness (COM) [97], V-Measure (V-M) [97], and Fowlkes-Mallows Index (FMI) [49] to measure the alignment of kMeans embedding clusters with groundtruth labels (with same number of clusters and labels). We also study label-unrelated scores and supervised classifier accuracy in section E.2.

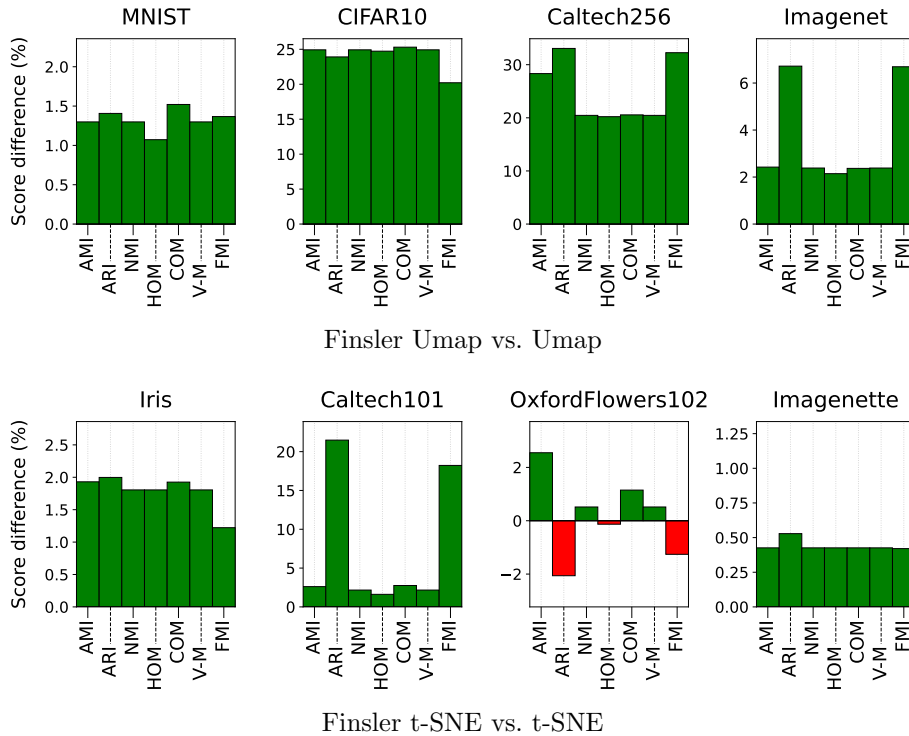


Figure 9: Percentage difference in mean performance between our Finsler methods and their traditional Euclidean baselines. Positive (resp. negative) differences, in green (resp. red), means we get better (resp. worse) scores comparing kMeans clusters with groundtruth class labels. See section F.3.1 for full results on all tested datasets, with visual summaries (fig. 14), raw performance values, and standard deviations (tables 2 and 3).

Methods. To measure the gain from accounting for sampling asymmetry and Finsler space embeddings, we compare the reference methods favouring clustering, t-SNE and Umap, with their Finsler counterparts. Default deterministic initialisation makes (Finsler) t-SNE deterministic – one run needed, unlike (Finsler) Umap as it relies on random negative sampling – we report the mean over 10 runs. Euclidean (resp. Finsler) methods embed in \mathbb{R}^m (resp. \mathbb{R}^{m+1}), with $m = 2$. We also report Euclidean (resp. Finsler) results in \mathbb{R}^3 (resp. \mathbb{R}^2) in section F.3.3, and include ablations on the embedding dimensionality m (section F.3.4) and on the levels of emphasis on asymmetry $\|\omega\|_2$ (section F.3.5).

Results. Across datasets, our asymmetric pipeline with Finsler embeddings consistently surpasses Euclidean baselines on label-related metrics (fig. 9), including supervised ones in section F.3.1, implying higher quality embeddings. Finsler Umap (resp. t-SNE) outperforms Umap (resp. t-SNE) on every dataset and label-related score¹¹. Finsler embeddings thus preserve the data more faithfully, though clusters may look less “nice” (see label-unrelated scores in section F.3.1). They also make the asymmetry explicit, which is lost information in Euclidean methods. We provide qualitative results on large datasets (fig. 8) showcasing better cluster-label alignment with our Finsler pipeline. For example in Caltech256, Umap sometimes formed clusters decorrelated with labels, but Finsler Umap did not. Full results for all datasets appear in section F.3 due to length constraints. Also our Finsler methods are robust to the choice of asymmetry emphasis $\|\omega\|_2$ (section F.3.5), with strong performance on a range of values.

¹¹Except OxfordFlowers102 where Finsler t-SNE is only on par ($\leq 2\%$) for some scores by a change in the third decimal (see table 3).

7 Conclusion

We propose a novel general manifold learning pipeline, which captures, harnesses, and reveals the asymmetry arising from discrete samples, e.g. from non-uniform densities. It is further motivated when observing that the traditional symmetric pipeline constructs asymmetric dissimilarities, requiring symmetrisation, discarding valuable information in the process. We deliberately construct asymmetric dissimilarities and embed in the canonical Finsler, rather than Euclidean, space, which supports asymmetry. Our approach greatly broadens the applicability of the rare existing asymmetric embedders, that were all limited to traditionally asymmetric data, to any data. We also generalise modern reference symmetric methods to handle asymmetric data, especially our Finsler t-SNE and Finsler Umap generalisation of t-SNE and Umap, providing asymmetric embedders for large scale data. Through extensive evaluations, from controlled well-understood small-scale settings to uncontrolled large-scale ones, we demonstrate that our asymmetric Finsler pipeline provides novel insights through visualisations and superior quality embeddings to their Euclidean counterparts.

Limitations and future work. We fix a specific Finsler metric for the embedding space, yielding increasing distortions the more the data’s structure deviates from it, as in the Euclidean case. We also provide a single asymmetry direction, yet applications might prefer disentangling more asymmetry directions, thus requiring other Finsler metrics. Without further information, our asymmetry is inferred from sampling densities. Yet, if points had features, we could derive from them other non-uniform local concepts, implying differently semantic asymmetries – an exciting avenue we plan to explore. Finally, Finsler geometry is not limited to manifold learning, yet remains largely uncharted in computer vision.

References

- [1] Aflalo, Y., Kimmel, R.: Spectral multidimensional scaling. *Proceedings of the National Academy of Sciences* **110**(45), 18052–18057 (2013) [2](#), [7](#)
- [2] Álvarez-Meza, A., Valencia-Aguirre, J., Daza-Santacoloma, G., Castellanos-Domínguez, G.: Global and local choice of the number of nearest neighbors in locally linear embedding. *Pattern Recognition Letters* **32**(16), 2171–2177 (2011) [4](#)
- [3] Amenta, N., Bern, M., Kamvysselis, M.: A new voronoi-based surface reconstruction algorithm. In: *Proceedings of the 25th annual conference on Computer graphics and interactive techniques*. pp. 415–421 (1998) [4](#)
- [4] Arias-Castro, E., Lerman, G., Zhang, T.: Spectral clustering based on local pca. *Journal of Machine Learning Research* **18**(9), 1–57 (2017) [4](#)
- [5] Bao, D., Chern, S.S., Shen, Z.: *An introduction to Riemann-Finsler geometry*, vol. 200. Springer Science & Business Media (2012) [3](#), [6](#)
- [6] Belkin, M., Niyogi, P.: Laplacian eigenmaps and spectral techniques for embedding and clustering. *Advances in neural information processing systems* **14** (2001) [2](#)
- [7] Belkin, M., Niyogi, P.: Laplacian eigenmaps for dimensionality reduction and data representation. *Neural computation* **15**(6), 1373–1396 (2003) [2](#), [6](#), [7](#), [11](#)
- [8] Belkin, M., Sun, J., Wang, Y.: Constructing laplace operator from point clouds in \mathbb{R}^d . In: *Proceedings of the twentieth annual ACM-SIAM symposium on Discrete algorithms*. pp. 1031–1040. SIAM (2009) [4](#)

- [9] Bernardini, F., Mittleman, J., Rushmeier, H., Silva, C., Taubin, G.: The ball-pivoting algorithm for surface reconstruction. *IEEE transactions on visualization and computer graphics* **5**(4), 349–359 (2002) [4](#)
- [10] Boissonnat, J.D., Guibas, L.J., Oudot, S.Y.: Manifold reconstruction in arbitrary dimensions using witness complexes. In: *Proceedings of the twenty-third annual symposium on Computational geometry*. pp. 194–203 (2007) [4](#)
- [11] Bonnans, J.F., Bonnet, G., Mirebeau, J.M.: A linear finite-difference scheme for approximating Randers distances on cartesian grids. *ESAIM: Control, Optimisation and Calculus of Variations* **28**, 45 (2022) [3](#)
- [12] Borg, I., Groenen, P.J.: *Modern multidimensional scaling: Theory and applications*. Springer Science & Business Media (2007) [3](#), [5](#)
- [13] Bracha, A., Dagès, T., Kimmel, R.: Wormhole loss for partial shape matching. *arXiv preprint arXiv:2410.22899* (2024) [2](#), [4](#), [5](#)
- [14] Brand, M.: Nonrigid embeddings for dimensionality reduction. In: *European Conference on Machine Learning*. pp. 47–59. Springer (2005) [2](#)
- [15] Bronstein, A.M., Bronstein, M.M., Kimmel, R.: Efficient computation of isometry-invariant distances between surfaces. *SIAM Journal on Scientific Computing* **28**(5), 1812–1836 (2006) [4](#)
- [16] Bronstein, A.M., Bronstein, M.M., Kimmel, R.: Generalized multidimensional scaling: a framework for isometry-invariant partial surface matching. *Proceedings of the National Academy of Sciences* **103**(5), 1168–1172 (2006) [2](#), [4](#)
- [17] Bronstein, A.M., Bronstein, M.M., Kimmel, R.: Robust expression-invariant face recognition from partially missing data. In: *Computer Vision—ECCV 2006: 9th European Conference on Computer Vision, Graz, Austria, May 7–13, 2006, Proceedings, Part III 9*. pp. 396–408. Springer (2006) [4](#)
- [18] Bronstein, M.M., Bronstein, A.M., Kimmel, R., Yavneh, I.: Multigrid multidimensional scaling. *Numerical linear algebra with applications* **13**(2-3), 149–171 (2006) [3](#)
- [19] Caliński, T., Harabasz, J.: A dendrite method for cluster analysis. *Communications in Statistics-theory and Methods* **3**(1), 1–27 (1974) [14](#)
- [20] Chen, D., Mirebeau, J.M., Cohen, L.D.: Global minimum for curvature penalized minimal path method. In: *Proc. of the British Machine Vision Conference (BMVC)*. pp. 86.1–86.12 (2015) [3](#)
- [21] Chen, D., Mirebeau, J.M., Cohen, L.D.: Finsler geodesics evolution model for region based active contours. In: *Proc. of the British Machine Vision Conference (BMVC)* (2016) [3](#)
- [22] Chen, D., Mirebeau, J.M., Cohen, L.D.: A new Finsler minimal path model with curvature penalization for image segmentation and closed contour detection. In: *IEEE Conference on Computer Vision and Pattern Recognition (CVPR)*. pp. 355–363 (2016) [3](#)
- [23] Chen, D., Mirebeau, J.M., Cohen, L.D.: Global minimum for a Finsler elastica minimal path approach. vol. 122, pp. 458–483 (2017) [3](#)
- [24] Chern, S.S.: Finsler geometry is just Riemannian geometry without the quadratic equation. *Notices of the American Mathematical Society* **43**(9), 959–963 (1996) [1](#), [6](#)

- [25] Chino, N.: A graphical technique for representing the asymmetric relationships between n objects. *Behaviormetrika* **5**, 23–40 (1978) [3](#)
- [26] Chino, N.: Asymmetric multidimensional scaling. *Journal of the Institute for Psychological and Physical Science* **3**(1), 101–107 (2011) [3](#)
- [27] Cimpoi, M., Maji, S., Kokkinos, I., Mohamed, S., Vedaldi, A.: Describing textures in the wild. In: *Proceedings of the IEEE conference on computer vision and pattern recognition*. pp. 3606–3613 (2014) [13](#)
- [28] Clanuwat, T., Bober-Irizar, M., Kitamoto, A., Lamb, A., Yamamoto, K., Ha, D.: Deep learning for classical japanese literature. *arXiv preprint arXiv:1812.01718* (2018) [13](#)
- [29] Cohen, G., Afshar, S., Tapson, J., Van Schaik, A.: Emnist: Extending mnist to handwritten letters. In: *2017 international joint conference on neural networks (IJCNN)*. pp. 2921–2926. IEEE (2017) [13](#)
- [30] Coifman, R.R., Lafon, S.: Diffusion maps. *Applied and computational harmonic analysis* **21**(1), 5–30 (2006) [2](#), [6](#), [7](#), [11](#)
- [31] Coifman, R.R., Lafon, S., Lee, A.B., Maggioni, M., Nadler, B., Warner, F., Zucker, S.W.: Geometric diffusions as a tool for harmonic analysis and structure definition of data: Diffusion maps. *Proceedings of the national academy of sciences* **102**(21), 7426–7431 (2005) [2](#)
- [32] Constantine, A., Gower, J.C.: Graphical representation of asymmetric matrices. *Journal of the Royal Statistical Society: Series C (Applied Statistics)* **27**(3), 297–304 (1978) [3](#)
- [33] Correa, C.D., Lindstrom, P.: Locally-scaled spectral clustering using empty region graphs. In: *Proceedings of the 18th ACM SIGKDD international conference on Knowledge discovery and data mining*. pp. 1330–1338 (2012) [4](#)
- [34] Costa, J.A., Girotra, A., Hero, A.O.: Estimating local intrinsic dimension with k -nearest neighbor graphs. In: *IEEE/SP 13th Workshop on Statistical Signal Processing, 2005*. pp. 417–422. IEEE (2005) [4](#)
- [35] Cox, T.F., Cox, M.A.: *Multidimensional scaling*. CRC press (2000) [3](#)
- [36] Dagès, T., Lindenbaum, M., Bruckstein, A.M.: Metric convolutions: A unifying theory to adaptive image convolutions. In: *Proceedings of the IEEE/CVF International Conference on Computer Vision*. pp. 13974–13984 (2025) [3](#), [6](#)
- [37] Dagès, T., Weber, S., Lin, Y.W.E., Talmon, R., Cremers, D., Lindenbaum, M., Bruckstein, A.M., Kimmel, R.: Finsler multi-dimensional scaling: Manifold learning for asymmetric dimensionality reduction and embedding. In: *Proceedings of the Computer Vision and Pattern Recognition Conference*. pp. 25842–25853 (2025) [1](#), [2](#), [3](#), [6](#), [7](#), [8](#), [9](#), [14](#), [15](#), [17](#), [22](#), [23](#)
- [38] Davies, D.L., Bouldin, D.W.: A cluster separation measure. *IEEE transactions on pattern analysis and machine intelligence* (2), 224–227 (2009) [14](#)
- [39] De Leeuw, J.: Application of convex analysis to multidimensional scaling. *Recent developments in statistics* pp. 133–145 (1977) [5](#), [3](#)
- [40] Deng, J., Dong, W., Socher, R., Li, L.J., Li, K., Fei-Fei, L.: Imagenet: A large-scale hierarchical image database. In: *2009 IEEE conference on computer vision and pattern recognition*. pp. 248–255. Ieee (2009) [13](#)

- [41] Dijkstra, E.W.: A note on two problems in connexion with graphs. *Numerische mathematik* **1**(1), 269–271 (1959) [4](#)
- [42] Dong, W., Moses, C., Li, K.: Efficient k-nearest neighbor graph construction for generic similarity measures. In: *Proceedings of the 20th international conference on World wide web*. pp. 577–586 (2011) [14](#)
- [43] Donoho, D.L., Grimes, C.: Hessian eigenmaps: Locally linear embedding techniques for high-dimensional data. *Proceedings of the National Academy of Sciences* **100**(10), 5591–5596 (2003) [2](#), [6](#)
- [44] Dybala, L., Zucker, S.W.: Ian: Iterated adaptive neighborhoods for manifold learning and dimensionality estimation. *Neural Computation* **35**(3), 453–524 (2023) [4](#)
- [45] Fei-Fei, L., Fergus, R., Perona, P.: Learning generative visual models from few training examples: An incremental bayesian approach tested on 101 object categories. In: *2004 conference on computer vision and pattern recognition workshop*. pp. 178–178. IEEE (2004) [13](#)
- [46] Fischl, B., Sereno, M.I., Dale, A.M.: Cortical surface-based analysis: Ii: inflation, flattening, and a surface-based coordinate system. *Neuroimage* **9**(2), 195–207 (1999) [2](#)
- [47] Fisher, R.A.: The use of multiple measurements in taxonomic problems. *Annals of eugenics* **7**(2), 179–188 (1936) [13](#)
- [48] Forgy, E.W.: Cluster analysis of multivariate data: efficiency versus interpretability of classifications. *biometrics* **21**, 768–769 (1965) [11](#)
- [49] Fowlkes, E.B., Mallows, C.L.: A method for comparing two hierarchical clusterings. *Journal of the American statistical association* **78**(383), 553–569 (1983) [11](#)
- [50] Funke, T., Guo, T., Lancic, A., Antulov-Fantulin, N.: Low-dimensional statistical manifold embedding of directed graphs. In: *8th International Conference on Learning Representations (ICLR 2020)*. vol. 3, pp. 2018–2035. Curran (2020) [2](#)
- [51] Gabriel, K.R., Sokal, R.R.: A new statistical approach to geographic variation analysis. *Systematic zoology* **18**(3), 259–278 (1969) [4](#)
- [52] Gou, J., Yuan, X., Xue, Y., Du, L., Yu, J., Xia, S., Zhang, Y.: Discriminative and geometry-preserving adaptive graph embedding for dimensionality reduction. *Neural Networks* **157**, 364–376 (2023) [2](#)
- [53] Gower, J.C.: The analysis of asymmetry and orthogonality. *Recent developments in statistics* pp. 109–123 (1977) [3](#)
- [54] Griffin, G., Holub, A., Perona, P., et al.: Caltech-256 object category dataset. Tech. rep., Technical Report 7694, California Institute of Technology Pasadena (2007) [13](#)
- [55] He, K., Zhang, X., Ren, S., Sun, J.: Deep residual learning for image recognition. In: *Proceedings of the IEEE conference on computer vision and pattern recognition*. pp. 770–778 (2016) [13](#)
- [56] Hotelling, H.: Analysis of a complex of statistical variables into principal components. *Journal of educational psychology* **24**(6), 417 (1933) [2](#)
- [57] Howard, J.: Imagenette: A smaller subset of imagenet (March 2019), <https://github.com/fastai/imagenette> [13](#)

- [58] Hubert, L., Arabie, P.: Comparing partitions. *Journal of classification* **2**(1), 193–218 (1985) [11](#)
- [59] İnkaya, T., Kayaligil, S., Özdemirel, N.E.: An adaptive neighbourhood construction algorithm based on density and connectivity. *Pattern Recognition Letters* **52**, 17–24 (2015) [4](#)
- [60] Jaromczyk, J., Toussaint, G.: Relative neighborhood graphs and their relatives. *Proceedings of the IEEE* **80**(9), 1502–1517 (1992) [4](#)
- [61] Javaloyes, M.A., Sánchez, M.: On the definition and examples of Finsler metrics. *arXiv preprint arXiv:1111.5066* (2011) [6](#)
- [62] Joharinad, P., Fahimi, H., Barth, L.S., Keck, J., Jost, J.: Isumap: Manifold learning and data visualization leveraging vietoris-rips filtrations. In: *Proceedings of the AAAI Conference on Artificial Intelligence*. vol. 39, pp. 17699–17706 (2025) [2](#)
- [63] Kim, J., Wang, X.: Inductive global and local manifold approximation and projection. *Transactions on Machine Learning Research* (2024) [2](#)
- [64] Kingma, D.P.: Adam: A method for stochastic optimization. *arXiv preprint arXiv:1412.6980* (2014) [15](#)
- [65] Klimovskaia, A., Lopez-Paz, D., Bottou, L., Nickel, M.: Poincaré maps for analyzing complex hierarchies in single-cell data. *Nature communications* **11**(1), 2966 (2020) [2](#), [11](#), [15](#)
- [66] Krizhevsky, A., Hinton, G., et al.: Learning multiple layers of features from tiny images (2009) [13](#)
- [67] Kropina, V.: On projective Finsler spaces with a metric of some special form. *Naučn. Dokl Vyss. Skoly. Fiz-Mat. Mauki* **2**, 38–42 (1959) [6](#)
- [68] Kruskal, J.B.: Multidimensional scaling by optimizing goodness of fit to a nonmetric hypothesis. *Psychometrika* **29**(1), 1–27 (1964) [2](#), [3](#)
- [69] Kullback, S., Leibler, R.A.: On information and sufficiency. *The annals of mathematical statistics* **22**(1), 79–86 (1951) [5](#)
- [70] Lam, S.K., Pitrou, A., Seibert, S.: Numba: A llvm-based python jit compiler. In: *Proceedings of the Second Workshop on the LLVM Compiler Infrastructure in HPC*. pp. 1–6 (2015) [15](#)
- [71] LeCun, Y., Bottou, L., Bengio, Y., Haffner, P.: Gradient-based learning applied to document recognition. *Proceedings of the IEEE* **86**(11), 2278–2324 (2002) [13](#)
- [72] de Leeuw, J., Heiser, W.: Theory of multidimensional scaling. *Handbook of statistics* **2**, 285–316 (1982) [3](#)
- [73] Lin, Y.W.E., Coifman, R.R., Mishne, G., Talmon, R.: Hyperbolic diffusion embedding and distance for hierarchical representation learning. In: *International Conference on Machine Learning*. pp. 21003–21025. PMLR (2023) [2](#)
- [74] Lin, Y.W.E., Coifman, R.R., Mishne, G., Talmon, R.: Tree-wasserstein distance for high dimensional data with a latent feature hierarchy. *arXiv preprint arXiv:2410.21107* (2024) [2](#)
- [75] Liu, Y.: Curvature augmented manifold embedding and learning. *arXiv preprint arXiv:2403.14813* (2024) [2](#)

- [76] Lloyd, S.: Least squares quantization in pcm. *IEEE transactions on information theory* **28**(2), 129–137 (1982) [11](#)
- [77] Van der Maaten, L., Hinton, G.: Visualizing data using t-sne. *Journal of machine learning research* **9**(11) (2008) [2](#), [3](#), [4](#), [11](#), [5](#), [13](#)
- [78] Martín-Merino, M., Muñoz, A.: Visualizing asymmetric proximities with SOM and MDS models. *Neurocomputing* **63**, 171–192 (2005) [2](#), [3](#)
- [79] Matsumoto, M.: On C-reducible Finsler spaces. *Tensor, NS* **24**, 29–37 (1972) [6](#)
- [80] Matsumoto, M.: A slope of a mountain is a Finsler surface with respect to a time measure. *Journal of Mathematics of Kyoto University* **29**(1), 17–25 (1989) [6](#)
- [81] McInnes, L., Healy, J., Melville, J.: Umap: Uniform manifold approximation and projection for dimension reduction. *arXiv preprint arXiv:1802.03426* (2018) [2](#), [3](#), [4](#), [14](#)
- [82] McQueen, J.B.: Some methods of classification and analysis of multivariate observations. In: *Proc. of 5th Berkeley Symposium on Math. Stat. and Prob.* pp. 281–297 (1967) [11](#)
- [83] Mekuz, N., Tsotsos, J.K.: Parameterless isomap with adaptive neighborhood selection. In: *Joint Pattern Recognition Symposium.* pp. 364–373. Springer (2006) [4](#)
- [84] Mikolov, T., Sutskever, I., Chen, K., Corrado, G.S., Dean, J.: Distributed representations of words and phrases and their compositionality. *Advances in neural information processing systems* **26** (2013) [8](#)
- [85] Mirebeau, J.M.: Efficient fast marching with Finsler metrics. *Numerische mathematik* **126**(3), 515–557 (2014) [3](#)
- [86] Nilsback, M.E., Zisserman, A.: Automated flower classification over a large number of classes. In: *2008 Sixth Indian conference on computer vision, graphics & image processing.* pp. 722–729. IEEE (2008) [13](#)
- [87] Ohta, S.i., Sturm, K.T.: Heat flow on Finsler manifolds. *Communications on Pure and Applied Mathematics: A Journal Issued by the Courant Institute of Mathematical Sciences* **62**(10), 1386–1433 (2009) [3](#)
- [88] Okada, A., Imaizumi, T.: Nonmetric multidimensional scaling of asymmetric proximities. *Behaviormetrika* **14**(21), 81–96 (1987) [3](#)
- [89] Okada, K.: A bayesian approach to asymmetric multidimensional scaling. *Behaviormetrika* **39**, 49–62 (2012) [3](#)
- [90] Pai, G., Bronstein, A., Talmon, R., Kimmel, R.: Deep isometric maps. *Image and Vision Computing* **123**, 104461 (2022) [2](#)
- [91] Parkhi, O.M., Vedaldi, A., Zisserman, A., Jawahar, C.: Cats and dogs. In: *2012 IEEE conference on computer vision and pattern recognition.* pp. 3498–3505. IEEE (2012) [13](#)
- [92] Pearson, K.: On lines and planes of closest fit to systems of points in space. *The London, Edinburgh, and Dublin philosophical magazine and journal of science* **2**(11), 559–572 (1901) [2](#)
- [93] Pedregosa, F., Varoquaux, G., Gramfort, A., Michel, V., Thirion, B., Grisel, O., Blondel, M., Prettenhofer, P., Weiss, R., Dubourg, V., et al.: Scikit-learn: Machine learning in python. *the Journal of machine Learning research* **12**, 2825–2830 (2011) [5](#), [1](#), [4](#), [14](#)

- [94] Radford, A., Kim, J.W., Hallacy, C., Ramesh, A., Goh, G., Agarwal, S., Sastry, G., Askell, A., Mishkin, P., Clark, J., et al.: Learning transferable visual models from natural language supervision. In: International conference on machine learning. pp. 8748–8763. PmLR (2021) [13](#)
- [95] Randers, G.: On an asymmetrical metric in the four-space of general relativity. *Physical Review* **59**(2), 195 (1941) [6](#)
- [96] Ratliff, N.D., Van Wyk, K., Xie, M., Li, A., Rana, M.A.: Generalized nonlinear and finsler geometry for robotics. In: 2021 IEEE International Conference on Robotics and Automation (ICRA). pp. 10206–10212. IEEE (2021) [3](#)
- [97] Rosenberg, A., Hirschberg, J.: V-measure: A conditional entropy-based external cluster evaluation measure. In: Proceedings of the 2007 joint conference on empirical methods in natural language processing and computational natural language learning (EMNLP-CoNLL). pp. 410–420 (2007) [11](#)
- [98] Rosman, G., Bronstein, A.M., Bronstein, M.M., Kimmel, R.: Topologically constrained isometric embedding. *Human Motion: Understanding, Modelling, Capture, and Animation* pp. 243–262 (2008) [4](#)
- [99] Rosman, G., Bronstein, M.M., Bronstein, A.M., Kimmel, R.: Nonlinear dimensionality reduction by topologically constrained isometric embedding. *International Journal of Computer Vision* **89**(1), 56–68 (2010) [2](#), [4](#), [5](#)
- [100] Rousseeuw, P.J.: Silhouettes: a graphical aid to the interpretation and validation of cluster analysis. *Journal of computational and applied mathematics* **20**, 53–65 (1987) [14](#)
- [101] Roweis, S.T., Saul, L.K.: Nonlinear dimensionality reduction by locally linear embedding. *science* **290**(5500), 2323–2326 (2000) [2](#), [6](#), [7](#), [11](#)
- [102] Saad, Y., Schultz, M.H.: GMRES: A generalized minimal residual algorithm for solving nonsymmetric linear systems. *SIAM Journal on scientific and statistical computing* **7**(3), 856–869 (1986) [17](#)
- [103] Saeed, N., Nam, H., Haq, M.I.U., Muhammad Saqib, D.B.: A survey on multidimensional scaling. *ACM Computing Surveys (CSUR)* **51**(3), 1–25 (2018) [2](#)
- [104] Schölkopf, B., Smola, A., Müller, K.R.: Nonlinear component analysis as a kernel eigenvalue problem. *Neural computation* **10**(5), 1299–1319 (1998) [2](#)
- [105] Schwartz, A., Talmon, R.: Intrinsic isometric manifold learning with application to localization. *SIAM Journal on Imaging Sciences* **12**(3), 1347–1391 (2019) [2](#), [4](#), [5](#)
- [106] Schwartz, E., Shaw, A., Wolfson, E.: A numerical solution to the generalized mapmaker’s problem: Flattening nonconvex polyhedral surfaces. *IEEE Transactions on Pattern Analysis and Machine Intelligence* **11**(9), 1005–1008 (1989) [2](#), [4](#), [3](#)
- [107] Shen, Z.: Finsler metrics with $K=0$ and $S=0$. *Canadian Journal of Mathematics* **55**(1), 112–132 (2003) [8](#)
- [108] Shepard, R.N.: The analysis of proximities: multidimensional scaling with an unknown distance function. i. *Psychometrika* **27**(2), 125–140 (1962) [2](#), [3](#)
- [109] Stallkamp, J., Schlipsing, M., Salmen, J., Igel, C.: Man vs. computer: Benchmarking machine learning algorithms for traffic sign recognition. *Neural networks* **32**, 323–332 (2012) [13](#)

- [110] Steinhaus, H., et al.: Sur la division des corps matériels en parties. *Bull. Acad. Polon. Sci* **1**(804), 801 (1956) [11](#)
- [111] Suzuki, R., Takahama, R., Onoda, S.: Hyperbolic disk embeddings for directed acyclic graphs. In: *International Conference on Machine Learning*. pp. 6066–6075. PMLR (2019) [2](#)
- [112] Tang, J., Liu, J., Zhang, M., Mei, Q.: Visualizing large-scale and high-dimensional data. In: *Proceedings of the 25th international conference on world wide web*. pp. 287–297 (2016) [2](#), [8](#)
- [113] Tanioka, K., Yadohisa, H.: Asymmetric mds with categorical external information based on radius model. *Procedia Computer Science* **140**, 284–291 (2018) [3](#)
- [114] Tenenbaum, J.B., Silva, V.d., Langford, J.C.: A global geometric framework for nonlinear dimensionality reduction. *science* **290**(5500), 2319–2323 (2000) [2](#), [4](#), [3](#), [6](#), [11](#)
- [115] Toussaint, G.T.: The relative neighbourhood graph of a finite planar set. *Pattern recognition* **12**(4), 261–268 (1980) [4](#)
- [116] [SimpleMaps.com](https://simplemaps.com/): US Zip Codes Database. <https://simplemaps.com/data/us-zips>, data updated as of February 10, 2026 [10](#)
- [117] Van Der Maaten, L.: Learning a parametric embedding by preserving local structure. In: *Artificial intelligence and statistics*. pp. 384–391. PMLR (2009) [5](#), [1](#), [2](#), [4](#)
- [118] Venna, J., Peltonen, J., Nybo, K., Aidos, H., Kaski, S.: Information retrieval perspective to nonlinear dimensionality reduction for data visualization. *Journal of Machine Learning Research* **11**(2) (2010) [2](#)
- [119] Vinh, N.X., Epps, J., Bailey, J.: Information theoretic measures for clusterings comparison: is a correction for chance necessary? In: *Proceedings of the 26th annual international conference on machine learning*. pp. 1073–1080 (2009) [11](#)
- [120] Wandell, B.A., Chial, S., Backus, B.T.: Visualization and measurement of the cortical surface. *Journal of cognitive neuroscience* **12**(5), 739–752 (2000) [2](#)
- [121] Weber, S., Dagès, T., Gao, M., Cremers, D.: Finsler-laplace-beltrami operators with application to shape analysis. In: *Proceedings of the IEEE/CVF Conference on Computer Vision and Pattern Recognition*. pp. 3131–3140 (2024) [3](#), [6](#)
- [122] Weinberger, K., Packer, B., Saul, L.: Nonlinear dimensionality reduction by semidefinite programming and kernel matrix factorization. In: *International Workshop on Artificial Intelligence and Statistics*. pp. 381–388. PMLR (2005) [2](#)
- [123] Weinberger, K.Q., Saul, L.K.: Unsupervised learning of image manifolds by semidefinite programming. *International journal of computer vision* **70**, 77–90 (2006) [2](#)
- [124] Xiao, H., Rasul, K., Vollgraf, R.: Fashion-mnist: a novel image dataset for benchmarking machine learning algorithms. *arXiv preprint arXiv:1708.07747* (2017) [13](#)
- [125] Yang, F., Chai, L., Chen, D., Cohen, L.: Geodesic via asymmetric heat diffusion based on Finsler metric. In: *Computer Vision–ACCV 2018: 14th Asian Conference on Computer Vision, Perth, Australia, December 2–6, 2018, Revised Selected Papers, Part V 14*. pp. 371–386. Springer (2019) [3](#)
- [126] Young, F.W.: An asymmetric euclidean model for multi-process asymmetric data. In: *US-Japan Seminar on MDS, San Diego, USA, 1975* (1975) [3](#)

- [127] Zelnik-Manor, L., Perona, P.: Self-tuning spectral clustering. *Advances in neural information processing systems* **17** (2004) 4
- [128] Zermelo, E.: Über das navigationsproblem bei ruhender oder veränderlicher windverteilung. *ZAMM-Journal of Applied Mathematics and Mechanics/Zeitschrift für Angewandte Mathematik und Mechanik* **11**(2), 114–124 (1931) 8
- [129] Zhang, Z., Wang, J.: MLLÉ: Modified locally linear embedding using multiple weights. *Advances in neural information processing systems* **19** (2006) 2, 6
- [130] Zhang, Z., Wang, J., Zha, H.: Adaptive manifold learning. *IEEE transactions on pattern analysis and machine intelligence* **34**(2), 253–265 (2011) 4
- [131] Zhang, Z., Zha, H.: Principal manifolds and nonlinear dimensionality reduction via tangent space alignment. *SIAM journal on scientific computing* **26**(1), 313–338 (2004) 2, 6
- [132] Zhu, Q., Feng, J., Huang, J.: Natural neighbor: A self-adaptive neighborhood method without parameter k. *Pattern recognition letters* **80**, 30–36 (2016) 4

Harnessing Data Asymmetry: Manifold Learning in the Finsler World

Supplementary Material

This supplementary is organised as follows.

- **Section A** further presents existing methods. In particular, it provides full details on the t-SNE and Umap methods and corrects a bug in the update rule of t-SNE that is present not only in the original paper [117] but also in common reference libraries like Scikit-learn [93].
- **Section B** provides our well-justified remedy to the symmetric manifold learning pipeline that avoids asymmetry altogether by proving theorem 4.
- **Section C** comprises in the proof of theorems 1 and 2, which are the full derivations of the update rules for our Finsler t-SNE and Finsler Umap.
- **Section D** presents how to generalise traditional spectral methods to asymmetry using Finsler geometry.
- **Section E** includes extensive implementation details for all experiments, including those in the supplementary material, allowing full independent reproducibility based on the paper alone.
- **Section F** contains further experiments, such as ablation studies, full visualisations, or raw performance tables.

For conciseness, we denote in row-stacked format $\mathbf{X} \in \mathbb{R}^{N \times n}$ as the data points x_1, \dots, x_N and $\mathbf{Y} \in \mathbb{R}^{N \times m}$ as the embedded points y_1, \dots, y_N .

Table 1: Summary and comparison of manifold learning pipelines, using either the traditional Euclidean perspective or our novel Finsler one. As standard approaches naturally lead to data asymmetry, thus requiring artificially symmetrising the data to remain within symmetric Riemannian geometry, our pipeline embraces this asymmetry and preserves it by embedding into a Finsler space rather than a Riemannian one. With this new perspective, we generalise the reference modern manifold learning methods to handle asymmetric data.

Geometry Metric (Canonical space)	Pipeline	Method
	Multi-dimensional scaling	Uniform manifold approximation
	Classical MDS [106]	Umap [81]
	Student t-distributed stochastic neighbour embedding	
	t-SNE [77, 117]	
Data dissimilarities	$p_{ij} = \ x_j - x_i\ _2$ (to be extended <i>geodesically</i>)	$p_{ij} = e^{-\frac{\ x_j - x_i\ _2 - \rho_i}{\sigma_i}}$
Symmetrisation	$p_{ij} \leftarrow \frac{p_{ij} + p_{ji}}{2}$ OR $\max(p_{ij}, p_{ji})$	$p_{ij} \leftarrow p_{ij} + p_{ji} - p_{ij}p_{ji}$
Embedding dissimilarities	$q_{ij} = \ y_j - y_i\ _2$	$q_{ij} = \frac{1}{1 + a\ y_j - y_i\ _2^{2b}}$
Optimisation objective	$\mathcal{L} = \sum w_{ij}(q_{ij} - p_{ij})^2$	$\mathcal{L} = -\sum p_{ij} \ln q_{ij} + (1 - p_{ij}) \ln(1 - q_{ij})$
Riemann (Euclidean)	SMACOF $\mathbf{Y}^{(k+1)} = V^T B(\mathbf{Y}^{(k)}) \mathbf{Y}^{(k)}$	Gradient descent with negative sampling $\frac{\partial \mathcal{L}}{\partial y_i} = 2 \sum_j p_{ij} \cdot \frac{\partial c_{ij}^a}{\partial y_i} + (1 - p_{ij}) \cdot \frac{\partial c_{ij}^b}{\partial y_i}$ $\left\{ \begin{array}{l} \frac{\partial c_{ij}^a}{\partial y_i} = \frac{2ab\ y_j - y_i\ _2^{2(b-1)}}{1 + a\ y_j - y_i\ _2^{2b}} (y_i - y_j) \\ \frac{\partial c_{ij}^b}{\partial y_i} = \frac{\ y_j - y_i\ _2^2 (1 + a\ y_j - y_i\ _2^{2b})}{-2b} (y_i - y_j) \\ \frac{\partial c_{ij}^a}{\partial y_j} = \frac{\partial c_{ij}^b}{\partial y_j} \text{ and } \frac{\partial c_{ij}^a}{\partial y_i} = -\frac{\partial c_{ij}^b}{\partial y_i} \end{array} \right.$
Update rule	$V_{ij} = \begin{cases} -w_{ij} & \text{if } i \neq j, \\ \sum_{k \neq i} w_{ik} & \text{if } i = j. \end{cases}$ $B_{ij}(\mathbf{Y}) = \begin{cases} -w_{ij} / \ y_j - y_i\ _2 & \text{if } i \neq j \\ -\sum_{k \neq i} B_{ik}(\mathbf{Y}) & \text{if } i = j. \end{cases}$	
Finsler MDS (Ours, extends [37])	Finsler t-SNE (Ours)	Finsler Umap (Ours)
Data dissimilarities	$p_{ij} = \ x_j - x_i\ _2$ (to be extended <i>geodesically</i>)	$p_{ij} = e^{-\frac{\ x_j - x_i\ _2 - \rho_i}{\sigma_i}}$
Embedding dissimilarities	$q_{ij}^f = d_{FC}(y_i, y_j) = \ y_j - y_i\ _2 + \omega^T (y_j - y_i)$	$q_{ij}^f = \frac{1}{1 + a d_{FC}(y_i, y_j)^{2b}}$
Optimisation objective	$\mathcal{L} = \sum w_{ij}(q_{ij}^f - p_{ij})^2$	$\mathcal{L} = -\sum p_{ij} \ln q_{ij}^f + (1 - p_{ij}) \ln(1 - q_{ij}^f)$
Finsler (Canonical Randers)	Finsler SMACOF $\text{vec}(\mathbf{Y}^{(k+1)}) = K^T \text{vec}(B(\mathbf{Y}^{(k)}) \mathbf{Y}^{(k)} - C)$	Gradient descent with negative sampling $\frac{\partial \mathcal{L}}{\partial y_i} = \sum_j p_{ij} \cdot \frac{\partial c_{ij}^a}{\partial y_i} + p_{ji} \frac{\partial c_{ij}^b}{\partial y_i} + (1 - p_{ij}) \cdot \frac{\partial c_{ij}^a}{\partial y_i} + (1 - p_{ji}) \cdot \frac{\partial c_{ij}^b}{\partial y_i}$ $\left\{ \begin{array}{l} \frac{\partial c_{ij}^a}{\partial y_i} = \begin{cases} -w_{ij} & \text{if } i \neq j, \\ \sum_{k \neq i} w_{ik} & \text{if } i = j. \end{cases} \\ \frac{\partial c_{ij}^b}{\partial y_j} = \begin{cases} -w_{ij} / d_{FC}(y_i, y_j) & \text{if } i \neq j \\ -\sum_{k \neq i} B_{ik}(\mathbf{Y}) & \text{if } i = j. \end{cases} \\ K = (I_m + \omega \omega^T) \otimes V \\ C = (W \odot D - W^T \odot D^T) \mathbb{1}_m \omega^T \end{array} \right.$ $\frac{\partial c_{ij}^a}{\partial y_i} = \frac{2ab(d_{FC}(y_i, y_j))^{2b-1}}{1 + a(d_{FC}(y_i, y_j))^{2b}} (y_i - y_j) - \frac{2ab(d_{FC}(y_i, y_j))^{2b-1}}{1 + a(d_{FC}(y_i, y_j))^{2b}} \omega$ $\frac{\partial c_{ij}^b}{\partial y_j} = \frac{2ab(d_{FC}(y_i, y_j))^{2b-1}}{(1 + a(d_{FC}(y_i, y_j))^{2b}) \ y_j - y_i\ _2} (y_i - y_j) - \frac{2ab(d_{FC}(y_i, y_j))^{2b-1}}{1 + a(d_{FC}(y_i, y_j))^{2b}} \omega$ $\frac{\partial c_{ij}^a}{\partial y_j} = -\frac{\partial c_{ij}^b}{\partial y_i} \text{ and } \frac{\partial c_{ij}^a}{\partial y_i} = -\frac{\partial c_{ij}^b}{\partial y_j}$

A More details on existing manifold learning methods

A.1 Update rules of classical MDS

The minimisation objective in classical MDS is the weighted stress function

$$\mathcal{L} = \sum w_{ij}(q_{ij} - p_{ij})^2 = \sum w_{ij}(\|y_j - y_i\|_{ij} - D_{ij})^2. \quad (7)$$

SMACOF. There is no closed-form solution to the stress function of Vanilla MDS [106], even for uniform weights $w_{ij} = 1$. For minimisation, the SMACOF algorithm [39, 12] is widely used. This essentially iteratively minimises a simple majorising function of the stress, where finding the minimisation of the majorising function is easy. In practice, starting from some arbitrary initialisation, the SMACOF algorithm iteratively decreases the stress until reaching a local minimum using the following update rule

$$\mathbf{Y}^{(k+1)} = V^\dagger B(\mathbf{Y}^{(k)}) \mathbf{Y}^{(k)}, \quad (8)$$

where

$$V_{ij} = \begin{cases} -w_{ij} & \text{if } i \neq j, \\ \sum_{k \neq i} w_{ik} & \text{if } i = j. \end{cases} \quad (9)$$

$$B_{ij}(\mathbf{Y}) = \begin{cases} -w_{ij} \frac{D_{ij}}{\|y_j - y_i\|} & \text{if } i \neq j \\ -\sum_{k \neq i} B_{ik}(\mathbf{Y}) & \text{if } i = j. \end{cases} \quad (10)$$

and V^\dagger is the pseudo-inverse of V . It can be proven that this strategy is equivalent to scaled gradient descent with constant step size [18].

It is well-known that the SMACOF algorithm is highly sensitive to initialisation. Thus, in the field, it is considered good practice to initialise with the Isomap embedding (corresponding to uniform weights $w_{ij} = 1$ and a relaxed optimisation objective).

Isomap. To achieve a simple closed-form solution, the stress function in classical MDS is often relaxed to the strain function, with uniform weights $w_{ij} = 1$. Applying a squaring of the dissimilarities $p_{ij} \leftarrow p_{ij}^2$ and $q_{ij} \leftarrow q_{ij}^2$, the strain objective is given by

$$\mathcal{L} = \sum (q_{ij} - p_{ij})^2 = \sum (\|y_j - y_i\|_2^2 - D_{ij}^2)^2 \quad (11)$$

Switching from the stress to strain makes the objective quadratic and thus simpler to optimise. Indeed, the strain can be rewritten using the Gram matrix of the centred data, and is given by double centring of the squared-distance matrix $\mathbf{G} = -\frac{1}{2} \mathbf{J} \mathbf{D}^{(2)} \mathbf{J}^\top$, where $\mathbf{J} = \mathbf{I} - \frac{1}{N} \mathbf{1}_N \mathbf{1}_N^\top$ is the centring projector and $(\mathbf{D}^{(2)})_{ij} = D_{ij}^2$ is the matrix of squared distances (see section A.3 for more details). This makes this relaxed version of classical MDS a kernel problem, with kernel \mathbf{G} . The solution is then provided by eigendecomposition of \mathbf{G} . When using geodesic dissimilarities \mathbf{D} , this approach is called Isomap [114]. Although slightly different from solving the initial raw stress function, Isomap is nevertheless accepted as the reference method in the field for solving the classical MDS problem when weights are uniform $w_{ij} = 1$: it provides almost identical (good) solutions in practice, while being much faster as it does not require iterative minimisation and avoiding getting stuck in frequent local minima of the stress function. In prior works, the MDS objective often interchangeably means the stress or the strain objective, leading to much confusion, as in [37].

A.2 Update rules of t-SNE and Umap

From the optimisation perspective, both t-SNE and Umap simply perform gradient descent on their objective. For fast implementations even on CPU hardware and to fully use the

sparsity of the data, analytically computed gradients are directly implemented, rather than relying on more costly algorithms such as backpropagation via the chain-rule. We here present the analytical gradients of both objectives.

A.2.1 t-SNE.

The optimisation objective in t-SNE is the KL-divergence between sparse data dissimilarities p_{ij} and the embedded dissimilarities q_{ij} given by a globally normalised Student distribution with ν degrees of freedom: $q_{ij} = \frac{t_{ij}}{\sum_{k \neq l} t_{kl}}$ where $t_{ij} = \left(1 + \frac{\|x_j - x_i\|_2^2}{\nu}\right)^{-\frac{\nu+1}{2}}$. Recall that the KL-divergence between p_{ij} and q_{ij} is given by

$$\mathcal{L} = \sum p_{ij} \ln \left(\frac{p_{ij}}{q_{ij}} \right). \quad (12)$$

In the original t-SNE work [77], degrees of freedom were not considered, i.e. $\nu = 1$, these only came with the follow-up work [117] and is the standard in modern libraries.

However, there are several mistakes in the proofs of the works of Van der Maaten and Hinton [77, 117]. While in the original work, double mistakes end up cancelling each other out, leading to a correct result, they perform another mistake in the follow-up work which is not cancelled out, leading to an incorrect update rule in the paper. Unfortunately, this implies that the analytical gradient used in most libraries, even reference ones like Scikit-learn [93], are incorrect.

As such, we propose to rederive in detail the calculation of the gradient and fix the t-SNE update rule.

Theorem 3 (Fixed t-SNE gradient). *The correct update rule for t-SNE with ν degrees of freedom is*

$$\frac{\partial \mathcal{L}}{\partial y_i} = 2 \frac{\nu + 1}{\nu} \sum_j (p_{ij} - q_{ij}) \left(1 + \frac{\|y_j - y_i\|_2^2}{\nu}\right)^{-1} (y_i - y_j)$$

Proof. Recall that p_{ij} are calculated from the data and are thus constants from the perspective of the optimisation. The quantities varying with respect to the embedding \mathbf{Y} are q_{ij} . Each q_{ij} depends on all t_{kl} , and thus on the embedding of all other points, which explains why the gradient in y_i depends on all other y_j and not just local ones in the original space (i.e. local x_j around x_i).

We can rewrite the KL-divergence as

$$\mathcal{L} = \sum p_{ij} \ln p_{ij} - \sum p_{ij} \ln q_{ij}. \quad (13)$$

The first term depends only on the data p_{ij} and is independent from the embedding. As such, minimising the KL-divergence is the same as minimising the simplified loss

$$\mathcal{L} = - \sum p_{ij} \ln q_{ij}. \quad (14)$$

Denote $d_{ij} = \|y_j - y_i\|_2$ for conciseness. Recalling¹² that $\frac{\partial d_{ij}}{\partial y_i} = \frac{y_i - y_j}{\|y_i - y_j\|_2}$, we have

$$\frac{\partial \mathcal{L}}{\partial y_i} = \sum_j \frac{\partial \mathcal{L}}{\partial d_{ij}} \frac{\partial d_{ij}}{\partial y_i} + \frac{\partial \mathcal{L}}{\partial d_{ji}} \frac{\partial d_{ji}}{\partial y_i} \quad (15)$$

$$= \sum_j \left(\frac{\partial \mathcal{L}}{\partial d_{ij}} + \frac{\partial \mathcal{L}}{\partial d_{ji}} \right) \frac{y_i - y_j}{\|y_i - y_j\|_2} \quad (16)$$

$$= 2 \sum_j \frac{\partial \mathcal{L}}{\partial d_{ij}} \frac{y_i - y_j}{\|y_i - y_j\|_2}. \quad (17)$$

¹²An incorrect formula for the differentiation of the distance was the reason for the first set of mistakes in the original work [77].

We now focus on the term $\frac{\partial \mathcal{L}}{\partial d_{ij}}$. Note that q_{ij} explicitly depends on every d_{kl} for all pairs (k, l) , due to the denominator $Z = \sum_{k \neq l} t_{kl}$ in q_{ij} . We then have

$$\frac{\partial \mathcal{L}}{\partial d_{ij}} = - \sum_{k \neq l} p_{kl} \left[\frac{\partial}{\partial d_{ij}} \left(-\frac{\nu+1}{2} \ln \left(1 + \frac{d_{kl}^2}{\nu} \right) \right) - \frac{\partial}{\partial d_{ij}} (\ln(Z)) \right] \quad (18)$$

$$= - \sum_{k \neq l} p_{kl} \left[-\frac{\nu+1}{2} \frac{1}{1 + \frac{d_{kl}^2}{\nu}} \frac{2d_{kl}}{\nu} \frac{\partial d_{kl}}{\partial d_{ij}} - \frac{1}{Z} \frac{\partial Z}{\partial d_{ij}} \right]. \quad (19)$$

Since we have $\frac{\partial d_{kl}}{\partial d_{ij}} = 1$ if $(i, j) = (k, l)$ and 0 otherwise, and since we also have $\frac{\partial Z}{\partial d_{ij}} = -\frac{\nu+1}{2} \left(1 + \frac{d_{ij}^2}{\nu} \right)^{-\frac{\nu+3}{2}} \frac{2d_{ij}}{\nu}$, and since $\sum_{k \neq l} p_{kl} = 1$, we have

$$\frac{\partial \mathcal{L}}{\partial d_{ij}} = \frac{\nu+1}{\nu} \frac{p_{ij} d_{ij}}{1 + \frac{d_{ij}^2}{\nu}} - \sum_{k \neq l} p_{kl} \frac{\nu+1}{\nu} \frac{d_{ij} \left(1 + \frac{d_{ij}^2}{\nu} \right)^{-\frac{\nu+3}{2}}}{Z} \quad (20)$$

$$= \frac{\nu+1}{\nu} (p_{ij} - q_{ij}) d_{ij} \left(1 + \frac{d_{ij}^2}{\nu} \right)^{-1}. \quad (21)$$

Returning to $\frac{\partial \mathcal{L}}{\partial y_i}$, and since $d_{ij} = \|y_i - y_j\|_2$ we get the desired result

$$\frac{\partial \mathcal{L}}{\partial y_i} = 2 \frac{\nu+1}{\nu} \sum_j (p_{ij} - q_{ij}) \left(1 + \frac{d_{ij}^2}{\nu} \right)^{-1} (y_i - y_j). \quad (22)$$

□

The correct derivation of the t-SNE update rule in theorem 3 contrasts with the formula derived by Van der Maaten and Hinton [117], which is

$$\begin{array}{c} \text{[Incorrect]} \\ \triangle \\ \frac{\partial \mathcal{L}}{\partial y_i} = 2 \frac{\nu+1}{\nu} \sum_j (p_{ij} - q_{ij}) \left(1 + \frac{d_{ij}^2}{\nu} \right)^{-\frac{\nu+1}{2}} (y_i - y_j). \\ \text{[Incorrect]} \\ \triangle \end{array} \quad (23)$$

The issue is the incorrect exponent of the term $\left(1 + \frac{d_{ij}^2}{\nu} \right)$, which should be -1 but was written $-\frac{\nu+1}{2}$ in [117], which is incorrect as soon as $\nu \neq 1$. This happens when the embedding dimension is $m \geq 3$ as the usual recipe is $\nu = \max(m-1, 1)$ ¹³. Common implementations of t-SNE, such as in the reference Scikit-learn library unfortunately carry on this mistake.

A.2.2 Umap.

The optimisation objective in Umap is the cross-entropy between the data dissimilarities p_{ij} and the embedded dissimilarities q_{ij} given by a (optionally tweaked) Student distribution with 1 degree of freedom but without global normalisation: $q_{ij} = (1 + a \|y_j - y_i\|_2^{2b})^{-1}$,

¹³In [117], the recipes $\nu = m-1$ so that planar embeddings have one degree of freedom, matching the original work [77]. In Scikit-learn, the max with 1 is taken avoid crashes when embedding to a one-dimensional space.

where a and b can tweak the distribution away from a rigorous Student distribution. Recall that the cross-entropy loss between p_{ij} and q_{ij} is given by

$$\mathcal{L} = \sum p_{ij} \ln \left(\frac{p_{ij}}{q_{ij}} \right) + (1 - p_{ij}) \ln \left(\frac{1 - p_{ij}}{1 - q_{ij}} \right). \quad (24)$$

Denote $c_{ij}^a = -\ln q_{ij}$ and $c_{ij}^r = -\ln(1 - q_{ij})$ the symmetric attractive and repulsive forces respectively. Due to the absence of global normalisation, unlike in t-SNE, q_{ij} only explicitly depends on y_i and y_j . The gradient of the objective is then

$$\frac{\partial \mathcal{L}}{\partial y_i} = 2 \sum_j p_{ij} \cdot \frac{\partial c_{ij}^a}{\partial y_i} + (1 - p_{ij}) \cdot \frac{\partial c_{ij}^r}{\partial y_i}, \quad (25)$$

with

$$\begin{cases} \frac{\partial c_{ij}^a}{\partial y_i} = \frac{2ab \|y_j - y_i\|_2^{2(b-1)}}{1 + a \|y_j - y_i\|_2^{2b}} (y_i - y_j) \\ \frac{\partial c_{ij}^a}{\partial y_j} = -\frac{\partial c_{ij}^a}{\partial y_i} \\ \frac{\partial c_{ij}^r}{\partial y_i} = \frac{-2b}{\|y_j - y_i\|_2^2 (1 + a \|y_j - y_i\|_2^{2b})} (y_i - y_j) \\ \frac{\partial c_{ij}^r}{\partial y_j} = -\frac{\partial c_{ij}^r}{\partial y_i} \end{cases} \quad (26)$$

The attractive forces contribute sparsely to the loss due to weighting with the sparse p_{ij} . On the other hand, the repulsive forces are dense. To speed up computation, Umap uses negative sampling to only compute repulsive forces on a small number of random samples. This makes Umap a random algorithm beyond initialisation. Additionally, Umap is efficiently implemented with multi-threading, which adds another level of randomness.

A.3 Spectral methods

Spectral methods in manifold learning are a special type of Euclidean methods where the objective function was carefully designed such that it can be rewritten as a kernel problem and thus be solved directly via (generalised) eigendecomposition of a matrix constructed from the data dissimilarities \mathbf{D} . Spectral methods can be designed using various paradigms, such as distance preservation in Isomap [114], local linear preservation, e.g. LLE-based methods [101, 43, 129, 131], and the Laplacian in Laplacian eigenmaps [7] and Diffusion maps [30]. From the perspective of this paper, it is important to understand that spectral methods can systematically be given by solving optimisation problems involving (squared) pairwise Euclidean distances between embedded points y_i (analogues to our embedding dissimilarities) and fitting to some pairwise data terms (analogues to our data dissimilarities).

Isomap. The secret in relaxing the stress to the strain is the use of quadratic distances. Stacking up the squared distances into a matrix $\mathbf{D}_Y^{(2)}$, i.e. $(\mathbf{D}_Y^{(2)})_{ij} = \|y_j - y_i\|_2^2$, and assuming that the embedding \mathbf{Y} is centred, expanding the squared distances leads to $\mathbf{J}\mathbf{D}_Y^{(2)}\mathbf{J} = -2\mathbf{Y}\mathbf{Y}^\top$. In other words the Gram matrix $\mathbf{G}_Y = \mathbf{Y}\mathbf{Y}^\top = -\frac{1}{2}\mathbf{J}\mathbf{D}_Y^{(2)}\mathbf{J}$. As the strain objective is given by $\mathcal{L} = \|\mathbf{J}(\mathbf{D}_Y^{(2)} - \mathbf{D}^{(2)})\mathbf{J}\|_F^2$, where here $\|\cdot\|_F$ is the Frobenius norm, Isomap minimises the objective $\mathcal{L} = 4\|\mathbf{G}_Y - \mathbf{G}\|_F^2$, where $\mathbf{G} = -\frac{1}{2}\mathbf{J}\mathbf{D}^{(2)}\mathbf{J}$. This is a typical kernel formulation. As \mathbf{G}_Y has rank at most m , since $\mathbf{Y} \in \mathbb{R}^m$, a closed-form solution is provided by taking the top m eigenvectors of \mathbf{G} . The main advantage of spectral methods is that they are solved by eigendecomposition of a matrix, rather than by more costly iterative solvers that also risk getting stuck in local minima. This can often come at the cost of less robustness, e.g. to noise, as eigenvectors tend to be unstable (unlike eigenvalues).

Laplacian eigenmaps. Denote Δ an estimated graph Laplacian matrix on the data, with mass matrix \mathbf{A} and stiffness \mathbf{W} on the neighbourhood graph equipped with edge weights $W_{ij} = e^{-\frac{\|x_j - x_i\|_2^2}{t}}$ for some small time scale t . The connectivity weights \mathbf{W} are analogues of the data dissimilarities p . Laplacian eigenmaps [7] proposes to embed the data by taking the eigenvectors associated to the smallest eigenvalues of the generalised eigendecomposition $\Delta f = \lambda \mathbf{A} f$. This spectral approach is the solution to an alternative optimisation problem. Laplacian eigenmaps solves the constrained optimisation $\text{tr}(\mathbf{Y}^\top \Delta \mathbf{Y})$ subject to the constraint $\mathbf{Y}^\top \mathbf{A} \mathbf{Y} = \mathbf{I}$. For simplicity, assume that $\Delta = \mathbf{A} - \mathbf{W}$ is the unnormalised graph Laplacian, with $A_i = \sum_j W_{ij}$, where W_{ij} (resp. A_i) populate the matrix \mathbf{W} (resp. the diagonal matrix \mathbf{A}). The constrained objective can then be rewritten as $\mathcal{L} = \frac{1}{2} \sum W_{ij} \|y_j - y_i\|_2^2 = \text{tr}(\mathbf{Y}^\top \Delta \mathbf{Y})$. Using different Laplacians will modify the y_i terms. For instance, for the symmetric graph Laplacian $\Delta = \mathbf{I} - \mathbf{A}^{-\frac{1}{2}} \mathbf{W} \mathbf{A}^{-\frac{1}{2}}$, this choice rescales the data terms in the objective as the constrained objective becomes $\mathcal{L} = \frac{1}{2} \sum W_{ij} \left\| \frac{y_j}{\sqrt{A_j}} - \frac{y_i}{\sqrt{A_i}} \right\|_2^2 = \text{tr}(\mathbf{Y}^\top \Delta \mathbf{Y})$.

Diffusion maps. Diffusion maps [30] are tightly connected to Laplacian eigenmaps [7]. Denote again Δ , \mathbf{A} , and \mathbf{W} to be some Laplacian, its mass matrix, and its stiffness matrix. Again, $W_{ij} = e^{-\frac{\|x_j - x_i\|_2^2}{t}}$. The idea behind diffusion maps is to normalise the Laplacian and then view it as a Markov process transition matrix \mathbf{P} simulating heat diffusion. With this perspective, the goal is to preserve diffusion distances, rather than raw distances. Denoting λ_k (in decreasing order) and ψ_k the eigenvalues and eigenvectors of \mathbf{P} , the squared diffusion distance at time step t is given by $D_t^2(x_i, x_j) = \sum_k \lambda_k^{2t} ((\psi_k)_j - (\psi_k)_i)^2$. It can be rewritten, using the Euclidean norm as $D_t^2(x_i, x_j) = \|\phi_t(x_i) - \phi_t(x_j)\|_2^2$, where $\phi_t(x_i) = (\lambda_1^t(\psi_1)_i, \lambda_2^t(\psi_2)_i, \dots)$. To preserve the diffusion distance in \mathbb{R}^m embeddings, diffusion maps simply suggests to take as embedding $\phi_t(x_i)$ truncated to its first m columns. Like other spectral approaches, this embedding can be seen as the solution to an alternative optimisation objective involving Euclidean distances between embedded points y_i . For simplicity, assume that the transition matrix \mathbf{P} is symmetric, otherwise we could involve the Π -weights of the stationary distribution for reversibility of the Markov process, i.e. $\Pi \mathbf{P} = \mathbf{P}^\top \Pi$ for the diagonal matrix Π with diagonal entries π_i , and symmetrise by $\mathbf{P}^t \leftarrow \Pi \mathbf{P}^t$. Similar to Laplacian eigenmaps, with $\mathbf{I} - \mathbf{P}^t$ instead of Δ , minimising the quadratic form $\mathcal{L} = \frac{1}{2} \sum \mathbf{P}_{ij}^t \|y_j - y_i\|_2^2 = \text{tr}(\mathbf{Y}^\top (\mathbf{I} - \mathbf{P}^t) \mathbf{Y})$ subject to $\mathbf{Y}^\top \mathbf{Y} = \Lambda^{2t}$ yields the diffusion maps solution ϕ_t (note that the constraint was scaled by the eigenvalues in order to get them to multiply the eigenfunctions). As such, diffusion maps is simply Laplacian eigenmaps using the Markov transition matrix as weights in the optimisation and a scaled constraint. An alternate view of diffusion maps is to see it as a special case of spectral MDS, which applies MDS to diffusion distances, as discussed in the original paper of spectral MDS [1].

Locally linear embeddings. In locally linear embeddings (LLE) and its variations, the goal is to preserve the locally linear structure of the data. Thus, rather than raw distance dissimilarities, LLE-based methods focus on local reconstruction weights, which are inherently connected to distances, expressing each point as a weighted average of its neighbours. In vanilla LLE [101], the objective to minimise is

$$\mathcal{L} = \sum_i \left\| y_i - \sum_j W_{ij} y_j \right\|_2^2, \quad (27)$$

where the local reconstruction weights W_{ij} , acting as analogues to p_{ij} , are given by solving the least squares problem for vertices j within the neighbourhood $\mathcal{N}(i)$ of i

$$\min_j \sum_{W_{ij}=1} \left\| x_i - \sum_{j \in \mathcal{N}(i)} W_{ij} x_j \right\|_2^2, \quad (28)$$

with closed-form solution provided by Lagrangian optimisation. Expanding the quadratic objective of LLE, it can be rewritten in matrix form as $\mathcal{L} = \|(\mathbf{I} - \mathbf{W})\mathbf{Y}\|_F^2 = \text{tr}(\mathbf{Y}^\top \mathbf{G}_\mathbf{W} \mathbf{Y})$, where \mathbf{W} has entries W_{ij} , $\mathbf{G}_\mathbf{W} = (\mathbf{I} - \mathbf{W})^\top (\mathbf{I} - \mathbf{W})$, and tr is the trace operator. This is a kernel problem, with kernel $\mathbf{G}_\mathbf{W}$. The solution to LLE is thus to take the eigenvectors of $\mathbf{G}_\mathbf{W}$ with lowest eigenvalues.

B Fixing the symmetric pipeline

We here provide a principled remedy to the traditional manifold learning pipeline that is theoretically justified by metric geometry and guarantees symmetric dissimilarities.

The goal is to find a better symmetric estimate of the manifold distance $d_R(x_i, x_j)$ between close points. We still approximate the shortest geodesic path $\gamma(t) : x_i \rightsquigarrow x_j$ as the Euclidean line $(1-t)x_i + tx_j$ between close points. For approximating its length $d_R(x_i, x_j) = |\gamma| = \int_0^1 \|\gamma'(t)\|_{M(\gamma(t))} dt$, instead of a single metric estimate $M(\gamma(0)) = c(x_i)I$, we propose to interpolate the metric $M(\gamma(t)) = (1-t)M(x_i) + tM(x_j)$. Integrating along the segment provides the following symmetric approximation.

Theorem 4. *Given an isotropic non-uniform Riemannian metric R , with $M(x) = c(x)I$, then the geodesic distance between close points x_i and x_j is approximately given by*

$$d_R(x_i, x_j) = \frac{c(x_i) + c(x_j)}{2} \|x_j - x_i\|_2 = d_R(x_j, x_i).$$

Proof. Denote $\gamma(t) = (1-t)x_i + tx_j$ with $t \in [0, 1]$ a parametrisation of the Euclidean segment $x_j - x_i$, and $\gamma(1-t) = tx_i + (1-t)x_j$ the segment in the opposite direction. The estimated linearly interpolated metric $M(\gamma(t))$ is given by

$$M(\gamma(t)) = (1-t)M(x_i) + tM(x_j). \quad (29)$$

The length of the curve $\gamma(t)$, denoted $|\gamma(t)|$, is given by

$$|\gamma(t)| = \int_0^1 \|\gamma'(t)\|_{M(\gamma(t))} dt \quad (30)$$

$$= \int_0^1 \|x_j - x_i\|_{(1-t)M(x_i) + tM(x_j)} dt \quad (31)$$

$$= \int_0^1 ((1-t)c(x_i) + tc(x_j)) \|x_j - x_i\|_2 dt \quad (32)$$

$$= \frac{c(x_i) + c(x_j)}{2} \|x_j - x_i\|_2. \quad (33)$$

As the interpolated metric is isotropic, it is symmetric, leading to symmetric distances, meaning that the estimated geodesic distance is the same in both directions of traversal $|\gamma(t)| = |\gamma(1-t)|$. \square

As such, linearly interpolating the metric leads to averaging out start and end-point metric scale. Since commonly $c(x_i) = \frac{1}{\sigma_i}$, our Riemannian fix suggests to replace σ_i in the calculation of p_{ij} by the harmonic mean σ_{ij} of σ_i and σ_j .

Corollary 1. *Given an isotropic non-uniform Riemannian metric R , with $M(x) = c(x)I$ and $c(x_i) = \frac{1}{\sigma_i}$, then the geodesic distance between close points x_i and x_j is approximately given by*

$$d_R(x_i, x_j) = \frac{1}{\sigma_{ij}} \|x_j - x_i\|_2 \quad \text{with} \quad \frac{1}{\sigma_{ij}} = \frac{1}{2} \left(\frac{1}{\sigma_i} + \frac{1}{\sigma_j} \right).$$

Dissimilarities p_{ij} constructed from the symmetric estimate $d_R(x_i, x_j)$ using $p_{ij} = h^p(d_R(x_i, x_j))$ are guaranteed to be symmetric, unlike the ones from the traditional pipeline

$p_{ij} = h^p(R_{x_i}(x_j - x_i))$ that incorrectly rely on tangent rather than geodesic estimates of the distance between close points.

Our rigorous estimation significantly differs from the omnipresent approach in the literature of approximating $|\gamma(t)|$ by $M(x_i)\|x_j - x_i\|_2$ and $|\gamma(1-t)|$ by $M(x_j)\|x_j - x_i\|_2$ ¹⁴, as this leads for non-uniform metrics to asymmetric distance estimates, which violates the Riemannian assumption. We have thus provided a remedy that is theoretically grounded in Riemannian geometry to compute symmetric dissimilarities.

C Update rules of Finsler t-SNE and Finsler Umap

We here prove theorems 1 and 2. An important preliminary result to carry on the calculations is the following.

Theorem 5 (Gradient canonical Finsler distances). *The gradients of the canonical Finsler distance are given by $\frac{\partial d_{FC}}{\partial x}(x, y) = \frac{x-y}{\|y-x\|_2} - \omega$ and $\frac{\partial d_{FC}}{\partial y}(x, y) = \frac{y-x}{\|y-x\|_2} + \omega$. In particular, $\frac{\partial d_{FC}}{\partial x} = -\frac{\partial d_{FC}}{\partial y}$.*

Although the result might look trivial as the proof is immediate, the fact that the gradient of the asymmetric canonical Randers distance shares the same antisymmetry as the gradient of the Euclidean distance is remarkable. It is another particularity of this Finsler metric making it an asymmetric analogue to the Euclidean space that was not observed in [37]. We can then explicitly compute the gradients for the Finsler t-SNE and Finsler Umap update rules.

We first derive the update rule for Finsler t-SNE.

Theorem 1 – Finsler t-SNE. For compactness, denote $d_{ij}^F = d_{FC}(y_i, y_j)$ to be the asymmetric Finsler distance in the canonical Randers space between the embedded points y_i and y_j . Following the proof of standard Euclidean t-SNE, we write

$$\frac{\partial \mathcal{L}}{\partial y_i} = \sum_j \frac{\partial \mathcal{L}}{\partial d_{ij}^F} \frac{\partial d_{ij}^F}{\partial y_i} + \frac{\partial \mathcal{L}}{\partial d_{ji}^F} \frac{\partial d_{ji}^F}{\partial y_i}. \quad (34)$$

Using theorem 5, we have $\frac{\partial d_{ij}^F}{\partial y_i} = \frac{y_i - y_j}{\|y_i - y_j\|_2} - \omega$ and $\frac{\partial d_{ji}^F}{\partial y_i} = \frac{y_i - y_j}{\|y_i - y_j\|_2} + \omega$. We then have

$$\frac{\partial \mathcal{L}}{\partial y_i} = \sum_j \left(\frac{\partial \mathcal{L}}{\partial d_{ij}^F} + \frac{\partial \mathcal{L}}{\partial d_{ji}^F} \right) \frac{y_i - y_j}{\|y_i - y_j\|_2} + \sum_j \left(-\frac{\partial \mathcal{L}}{\partial d_{ij}^F} + \frac{\partial \mathcal{L}}{\partial d_{ji}^F} \right) \omega. \quad (35)$$

We now focus on the term $\frac{\partial \mathcal{L}}{\partial d_{ij}^F}$, which behaves exactly like its counterpart in standard Euclidean t-SNE. Nevertheless, we redo the derivations for completeness. Denoting the denominator $Z = \sum_{k \neq l} t_{kl}^F$ in q_{ij}^F , we have

$$\frac{\partial \mathcal{L}}{\partial d_{ij}^F} = - \sum_{k \neq l} p_{kl} \left[\frac{\partial}{\partial d_{ij}^F} \left(-\frac{\nu+1}{2} \ln \left(1 + \frac{(d_{kl}^F)^2}{\nu} \right) \right) - \frac{\partial}{\partial d_{ij}^F} (\ln(Z)) \right] \quad (36)$$

$$= - \sum_{k \neq l} p_{kl} \left[-\frac{\nu+1}{2} \frac{1}{1 + \frac{(d_{kl}^F)^2}{\nu}} \frac{2d_{kl}^F}{\nu} \frac{\partial d_{kl}^F}{\partial d_{ij}^F} - \frac{1}{Z} \frac{\partial Z}{\partial d_{ij}^F} \right]. \quad (37)$$

¹⁴And often, as in t-SNE, $M(x_i) = \frac{1}{\sigma_i}$ so the asymmetric distance estimates $\frac{\|x_j - x_i\|_2}{\sigma_i}$ and $\frac{\|x_j - x_i\|_2}{\sigma_j}$ lead to asymmetric dissimilarities.

Since $\frac{\partial d_{kl}^F}{\partial d_{ij}^F} = 1$ if $(i, j) = (k, l)$ and 0 otherwise, $\frac{\partial Z}{\partial d_{ij}^F} = -\frac{\nu+1}{2} \left(1 + \frac{(d_{ij}^F)^2}{\nu}\right)^{-\frac{\nu+3}{2}} \frac{2d_{ij}^F}{\nu}$, and $\sum_{k \neq l} p_{kl} = 1$, we have

$$\frac{\partial \mathcal{L}}{\partial d_{ij}^F} = \frac{\nu+1}{\nu} \frac{p_{ij} d_{ij}^F}{1 + \frac{(d_{ij}^F)^2}{\nu}} - \sum_{k \neq l} p_{kl} \frac{\nu+1}{\nu} \frac{d_{ij}^F \left(1 + \frac{(d_{ij}^F)^2}{\nu}\right)^{-\frac{\nu+3}{2}}}{Z} \quad (38)$$

$$= \frac{\nu+1}{\nu} (p_{ij} - q_{ij}^F) d_{ij}^F \left(1 + \frac{(d_{ij}^F)^2}{\nu}\right)^{-1}. \quad (39)$$

Returning to $\frac{\partial \mathcal{L}}{\partial y_i}$, we get the desired result

$$\begin{aligned} \frac{\partial \mathcal{L}}{\partial y_i} &= \frac{\nu+1}{\nu} \sum_j \left[(p_{ij} - q_{ij}^F) t_{ij}^F \frac{d_{FC}(y_i, y_j)}{\|y_j - y_i\|_2} + (p_{ji} - q_{ji}^F) t_{ji}^F \frac{d_{FC}(y_j, y_i)}{\|y_i - y_j\|_2} \right] (y_i - y_j) \\ &+ \frac{\nu+1}{\nu} \sum_j \left[-(p_{ij} - q_{ij}^F) t_{ij}^F d_{FC}(y_i, y_j) + (p_{ji} - q_{ji}^F) t_{ji}^F d_{FC}(y_j, y_i) \right] \omega. \end{aligned}$$

□
□

We now derive the update rule for Finsler Umap.

Theorem 2 – Finsler Umap. The gradient of the objective is given by

$$\frac{\partial \mathcal{L}}{\partial y_i} = \sum_j p_{ij} \cdot \frac{\partial c_{ij}^a}{\partial y_i} + p_{ji} \frac{\partial c_{ji}^a}{\partial y_i} + (1 - p_{ij}) \cdot \frac{\partial c_{ij}^r}{\partial y_i} + (1 - p_{ji}) \cdot \frac{\partial c_{ji}^r}{\partial y_i}. \quad (40)$$

Denote $d_{ij}^F = d_{FC}(y_i, y_j)$ the canonical Randers distance between. We first focus on the attractive forces $c_{ij}^a = -\ln(q_{ij}^F)$. We have

$$\frac{\partial c_{ij}^a}{\partial y_i} = -\frac{1}{q_{ij}^F} \frac{\partial q_{ij}^F}{\partial d_{ij}^F} \frac{\partial d_{ij}^F}{\partial y_i} \quad (41)$$

$$= \frac{1 + a(d_{ij}^F)^{2b}}{(1 + a(d_{ij}^F)^{2b})^2} 2ab(d_{ij}^F)^{2b-1} \frac{\partial d_{ij}^F}{\partial y_i}. \quad (42)$$

Using theorem 5, we have

$$\frac{\partial c_{ij}^a}{\partial y_i} = \frac{2ab \frac{(d_{ij}^F)^{2b-1}}{\|y_i - y_j\|_2}}{1 + a(d_{ij}^F)^{2b}} (y_i - y_j) - \frac{2ab(d_{ij}^F)^{2b-1}}{1 + a(d_{ij}^F)^{2b}} \omega. \quad (43)$$

Likewise, a similar calculation provides

$$\frac{\partial c_{ij}^a}{\partial y_j} = \frac{2ab \frac{(d_{ij}^F)^{2b-1}}{\|y_i - y_j\|_2}}{1 + a(d_{ij}^F)^{2b}} (y_j - y_i) + \frac{2ab(d_{ij}^F)^{2b-1}}{1 + a(d_{ij}^F)^{2b}} \omega \quad (44)$$

$$= -\frac{\partial c_{ij}^a}{\partial y_i}. \quad (45)$$

We now focus on the repulsive forces $c_{ij}^r = -\ln(1 - q_{ij}^F)$. We have

$$\frac{\partial c_{ij}^r}{\partial y_i} = \frac{1}{1 - q_{ij}^F} \frac{\partial q_{ij}^F}{\partial d_{ij}^F} \frac{\partial d_{ij}^F}{\partial y_i} \quad (46)$$

$$= \frac{1}{1 - q_{ij}^F} \frac{-1}{(1 + a(d_{ij}^F)^{2b})^2} 2ab(d_{ij}^F)^{2b-1} \left(\frac{y_i - y_j}{\|y_i - y_j\|_2} - \omega \right) \quad (47)$$

$$= \frac{-2b(q_{ij}^F)^2}{(1 - q_{ij}^F)} \left((q_{ij}^F)^{-1} - 1 \right) (d_{ij}^F)^{-1} \left(\frac{y_i - y_j}{\|y_i - y_j\|_2} - \omega \right) \quad (48)$$

$$= -2bq_{ij}^F (d_{ij}^F)^{-1} \left(\frac{y_i - y_j}{\|y_i - y_j\|_2} - \omega \right) \quad (49)$$

$$= \frac{-2b}{(1 + a(d_{ij}^F)^{2b}) d_{ij}^F \|y_i - y_j\|_2} (y_i - y_j) + \frac{2b}{(1 + a(d_{ij}^F)^{2b}) d_{ij}^F} \omega. \quad (50)$$

Likewise, a similar calculation provides

$$\frac{\partial c_{ij}^r}{\partial y_j} = \frac{-2b}{(1 + a(d_{ij}^F)^{2b}) d_{ij}^F \|y_i - y_j\|_2} (y_j - y_i) - \frac{2b}{(1 + a(d_{ij}^F)^{2b}) d_{ij}^F} \omega \quad (51)$$

$$= -\frac{\partial c_{ij}^r}{\partial y_i}. \quad (52)$$

□
□

D Asymmetric Finsler generalisation of spectral methods in manifold learning

As mentioned in the main manuscript, we can generalise spectral methods to our Finsler setting. As discussed in section A.3, spectral methods, e.g. Isomap [114], Laplacian eigenmaps [7], diffusion maps [30], and LLE [101], can be reformulated as quadratic optimisation problems involving a minimisation on pairwise Euclidean distances between embedded points y_i . We propose to naively generalise such methods by replacing the Euclidean distance $\|\cdot\|_2$ involving embedded points y_i by the Finsler distance d_F of the embedding space, e.g. the canonical Randers space distance. While this simple switch generalises these methods to embed asymmetric data, it comes at a major downside: the solution of the new Finsler objectives are no longer given by a simple eigendecomposition. Indeed, the asymmetry breaks the kernel formulation: the Finsler generalisation of spectral methods is no longer given by spectral optimisation. Rather than an elegant closed-form solution, we must instead perform iterative minimisation, e.g. via gradient descent, which is slower and more susceptible to get stuck in local minima. For this reason, we did not implement these generalisations and focused instead on those that do not strongly distort the solvers, like Finsler t-SNE and Finsler Umap.

As examples, here are some generalised Finsler objectives \mathcal{L} that can be minimised by gradient descent. By doing so we generalise spectral methods to asymmetry.

Finsler Isomap. Our proposed Finsler objective generalising Isomap to asymmetry is $\mathcal{L} = \sum w_{ij} (d_F^2(y_i, y_j) - \mathbf{D}_{ij}^2)^2$. Note that unlike in the Euclidean case, we can include non-uniform weights w_{ij} , as this does not impact the solver¹⁵. This method is similar to Finsler MDS, by minimising the Finsler strain rather than the Finsler stress. As in the

¹⁵In the Euclidean case, non-uniform weights make the problem no longer spectral and iterative optimisation must be performed.

Euclidean case, both methods should lead to similar results, but this time Finsler Isomap is not solved with a closed-form solution. Instead, gradient descent should be performed. In contrast, Finsler MDS speeds up the descent via the Finsler SMACOF algorithm, which produces faster descent than raw gradient descent. As such, we recommend Finsler MDS rather than Finsler Isomap.

Finsler Laplacian eigenmaps. Generalising Laplacian eigenmaps to asymmetry, we aim to minimise the Finsler objective $\mathcal{L} = \frac{1}{2} \sum W_{ij} d_F^2(s_i y_i, s_j y_j)$, where s_i is an optional scaling factor to account for different choices of Laplacians: $s_i = 1$ for the unnormalised graph Laplacian and $s_i = \frac{1}{\sqrt{A_i}}$ for the symmetric graph Laplacian. The optimisation should be constrained to $\mathbf{Y}^\top \mathbf{A} \mathbf{Y} = \mathbf{I}$, which can be enforced by Lagrangian optimisation. The final proposed objective is thus $\mathcal{L} = \frac{1}{2} \sum W_{ij} d_F^2(s_i y_i, s_j y_j)^2 + \lambda \|\mathbf{Y}^\top \mathbf{A} \mathbf{Y} - \mathbf{I}\|_F^2$ for some scalar λ ¹⁶. Gradient descent would be performed on the Lagrangian formulation. Note that in our Finsler case and unlike in the Euclidean case, the weights W_{ij} may be asymmetric.

Finsler diffusion maps. Generalising diffusion maps to asymmetry, we aim to minimise the Finsler objective $\mathcal{L} = \frac{1}{2} \sum \mathbf{P}_{ij}^t d_F^2(y_i, y_j)$, subject to the constraint $\mathbf{Y}^\top \mathbf{Y} = \mathbf{\Lambda}^{2t}$. To enforce this, we propose a Lagrangian formulation objective $\mathcal{L} = \frac{1}{2} \sum \mathbf{P}_{ij}^t d_F^2(y_i, y_j) + \lambda \|\mathbf{Y}^\top \mathbf{Y} - \mathbf{\Lambda}^{2t}\|_F^2$ for some scalar λ , as in Finsler Laplacian eigenmaps, to be minimised with gradient descent. Note that in our Finsler and unlike in Euclidean case, the weights W_{ij} may be asymmetric.

Finsler locally linear embeddings. Our proposed Finsler objective generalising the LLE method to asymmetry is $\mathcal{L} = \sum d_F^2(y_i, \sum_j W_{ij} y_j)$, where local weights W_{ij} are solution to the same constrained least-squares as in the Euclidean case. However, should the ambient space of the data be itself asymmetric, which would greatly justify the use of Finsler LLE over Euclidean LLE, for instance with a Finsler distance $d_F^{(X)}$ instead of the Euclidean distance, then the weights W_{ij} should be the solution to the following constrained optimisation problem: $\min (d_F^{(X)}(x_i, \sum_{j \in \mathcal{N}(i)} W_{ij} x_j))^2$ with $\sum_j W_{ij} = 1$ for all i . Both the Finsler LLE main objective and the optional Finsler variant defining the local weights W_{ij} can be solved via gradient descent.

E Implementation details

E.1 Data

E.1.1 Disk data.

The points are grid-sampled using uniform polar coordinates (ρ_i, θ_i) , with 20 angles θ_i and $\frac{\rho}{20} = 15$ radii ρ_i .

E.1.2 Swiss roll.

The Swiss roll manifold is parametrised in the unit square by $(u, v) \in [0, 1]^2$. The Swiss roll transformation used in this paper is given by $x = (\tilde{u} \cos(\tilde{u}), \tilde{v}, \tilde{u} \sin(\tilde{u}))^\top \in \mathbb{R}^3$, where the stretched parametrisation is $\tilde{u} = 3\pi(u + \frac{1}{2})$ and $\tilde{v} = 20v$. The points were sampled by uniformly grid sampling (u, v) in the unit square $[0, 1]^2$ using $n = \left\lfloor \frac{5}{2} \sqrt{\tilde{n}} \right\rfloor \times \left\lfloor \frac{2}{5} \sqrt{\tilde{n}} \right\rfloor$ samples. For $\tilde{N} = 2000$ this leads to $N = 1887$ effectively sampled points on the Swiss roll.

¹⁶ Which can be treated as a hyperparameter.

E.1.3 Persistence data.

This corresponds to the clustered manifold experiment in section F.2. For N samples, we first generate the labels of the datapoints. To do so, we generate non-integer and unbounded soft labels \tilde{c}_i using an exponential distribution $\tilde{c}_i \sim \text{Exp}(\lambda_{\text{exp}})$ with rate parameter λ_{exp} . We convert the unbounded soft labels to the bounded integer labels $c_i \in \{0, \dots, C-1\}$ for C number of Gaussians using $c_i = \text{clip}\left(\left\lfloor \frac{\tilde{c}_i}{Cq_{\text{exp}}(p)} \right\rfloor, 0, C-1\right)$, where $\text{clip}(\cdot, v_{\min}, v_{\max})$ is the clip function to min and maximum values v_{\min} and v_{\max} ¹⁷ and $q_{\text{exp}}(p)$ is the p_{exp} -th quantile of the exponential distribution and is given by $q_{\text{exp}}(p) = \frac{-\ln(1-p_{\text{exp}})}{\lambda_{\text{exp}}}$. In our experiments, $N = 500$, $\lambda_{\text{exp}} = 1$, $p_{\text{exp}} = 0.99$, and $C = 5$, which lead with our random seed to the following number of datapoints per Gaussian: 294, 121, 48, 28, 9.

We then generate the C random Gaussian distribution $\mathcal{N}(\mu_j, \Sigma_j)$ in the input data feature space \mathbb{R}^n used for sampling the random datapoints. We randomly sample the means $\mu_j \sim \mathcal{U}([0, 1]^n)$ uniformly in the unit cube of \mathbb{R}^n . We also randomly sample the symmetric positive definite covariance matrices Σ_j but we squash the eigenvalues using a rescaled sigmoid function in order to bound their scale. In practice, we uniformly generate $A_j \sim \mathcal{U}([0, 1]^{n \times n})$ a random matrix, from which we construct a random symmetric positive matrix $\tilde{\Sigma}_j = AA^\top$, albeit with unbounded eigenvalues and not necessarily definite. Denote B_j and $\tilde{\Lambda}_j$ as the unitary basis of eigenvectors and the eigenvalues of $\tilde{\Sigma}_j = B_j \tilde{\Lambda}_j B_j^\top$. We bound the scale of the eigenvalues by applying the scaled sigmoid function $\sigma_s(x) = \frac{s}{1+e^{-x}}$ to the eigenvalues of $\tilde{\Sigma}_j$, giving the new diagonal matrix $\sigma_s(\tilde{\Lambda}_j)$. To ensure that the resulting matrix is numerically definite (no close to zero eigenvalue), we perturb the eigenvalues by $\varepsilon > 0$. In summary, the random covariance matrices are given by $\Sigma_j = B_j \sigma_s(\tilde{\Lambda}_j) B_j^\top + \varepsilon I$, and we took $\varepsilon = 10^{-5}$ and $s = 0.1$ as the maximum eigenvalue scale in our experiments.

We then generate each input datapoint x_i by sampling the c_i -th random Gaussian $\mathcal{N}(\mu_{c_i}, \Sigma_{c_i})$ according to its randomly sampled label c_i .

E.1.4 Reference classification datasets.

The sixteen reference benchmarks we use are reference datasets in modern data learning. They form an extensive and particularly wide variety of classification datasets. Iris (150 tabular samples, 3 classes) [47] is the only non-image task. Stepping up from the smallest images, we first consider MNIST [71], Fashion-MNIST [124], Kuzushiji-MNIST [28], EMNIST (train split, 60000 images, 10 classes each) and EMNIST-Balanced (train split, 112 800 images, 47 classes) [29] of 28×28 -pixel grayscale characters. At the next resolution tier, CIFAR10 and CIFAR100 (train split) [66] each provide 50000 colour images of 32×32 pixels with 10 and 100 classes respectively; each picture is transformed to a 768-dimensional feature vector using a frozen CLIP [94] ViT-B32 pretrained on Imagenet as raw images are poorly embedded with traditional manifold learning techniques. Finally, we move to variable-resolution natural images represented by 2048-dimensional global-average-pooled features from a frozen Imagenet-pretrained ResNet50 [55]: DTD (train split, 1880 images, 47 classes) [27], Caltech101 (8677 images, 101 classes) [45], Caltech256 (30607 images, 257 classes) [54], OxfordFlowers102 (train split, 1020 images, 102 classes) [86], OxfordIIITPet (trainval split, 3680 images, 37 classes) [91], GTSRB (train split, 26640 images, 43 classes) [109], Imagenette (train split, 9469 images, 10 classes) [57] and the large-scale ImageNet (train split, 1281167 images, 1000 classes) [40]. No further processing is performed beyond the fixed CLIP or ResNet50 embedding step. Recall that as the original t-SNE algorithm [77] is slow, we only ran it and its Finsler variant on the smaller datasets.

¹⁷The purpose of the clip function is to bound the obtained integer values to at most $C-1$ by merging the largest unbounded integer labels to the last Gaussian with smallest number of datapoints.

E.2 Scores

Reference classification datasets. Our primary quantitative scores measure the fitting quality of kMeans clustering to the class labels of the data. They thus reflect how well we preserve the data manifold after embedding. However, the clustering community often uses other scores to measure the quality of their clustering, such as the Silhouette (SIL) [100], Davies-Bouldin Index (DBI) [38], and Calinski-Harabasz Index (CHI) [19]. However, these measures are unrelated to the data labels and solely evaluate if the clusters “look nice”¹⁸. As such, they do not reflect how well we preserve the data manifold after embedding. This makes the label-unrelated scores – SIL, DBI, and CHI – secondary compared to our primary label-related measures – AMI, ARI, NMI, HOM, COM V-M, and FMI. It is of no importance that a method provides clusters that “look nicer” if the clusters fit worse to the data labels and correspond less well to the reality of the data manifold. In the supplementary, we include to results the label-unrelated scores as an indication of the shape of our embedded clusters, but the primary and most interesting comparison quantities are the label-related ones.

In addition to the unsupervised kMeans clustering scores, whether related or not to the data labels, we also provide supervised scores, which are by definition label-related. They consist in the accuracy of trained simple classifiers on the embeddings. In our experiments, we use both a linear classifier and a 5 nearest neighbour classifier. As test accuracy depends on the train-test splits, we report the mean results for 2-repeated stratified 5-fold cross-validation (10 runs). While the unsupervised label-related scores are the primary scores in manifold learning, supervised scores bring additional insights to the performance of the methods.

E.3 Methods

All methods share the same initial precomputed kNN graph for computing data dissimilarities. Following what is done in Umap [81], we compute approximate nearest neighbours via the nearest neighbour descent algorithm [42] for k neighbours, with $k = 15$.

We use the default hyperparameters of t-SNE and Umap, and take the same for our Finsler t-SNE and Finsler Umap. In particular, the min distance hyperparameter is set to 0.1 (Umap and Finsler Umap) and the perplexity to 30 (t-SNE and Finsler t-SNE).

Optionally, in cases where manifold preservation is the main objective, we propose a refinement of the traditional Umap pipeline, to be incorporated as well in Finsler Umap, to geodesically extend the distances of the kNN graph and truncate the extended graph to keep only the k^+ smallest edges per node, with $k^+ > k$.

For both t-SNE and Umap, either the traditional Euclidean or our Finsler pipeline, dissimilarities are computed directly on the sparse kNN graph. For methods requiring geodesic extensions of the distances in the kNN graph, such as traditional MDS, like Isomap, and Finsler MDS, we need to connect the distance graph. To do so, we follow the methodology in Scikit-learn [93] for its Isomap implementation to greedily connect the closest pair of points in the Euclidean sense between any two connected components.

For initialisation, we followed the traditional recipes in the Euclidean case and generalised them to the Finsler case for our Finsler pipelines. Vanilla and Finsler t-SNE (resp. Umap) are initialised with the default deterministic PCA (resp. spectral) embedding. Vanilla and Finsler SMACOF, along with Finsler MDS using gradient descent, are initialised using Isomap. Such initialisation strategies are considered standard for the standard Euclidean methods (SMACOF, t-SNE and Umap). Following the methodology of [37], as the canonical Finsler space is the Euclidean hyperplane augmented with an axis of asymmetry, the initialisations in the Finsler methods are performed with one less dimension, to which is then added an extra dimension with 0 entry, and we then rotate

¹⁸Clusters are well-separated, condensed, spherically shaped...

the initialisation so that the new axis is along ω ¹⁹.

For Finsler MDS with our novel gradient descent implementation instead of the unstable and unscalable Finsler Smacof algorithm [37], we use an Adam optimiser [64] with default hyperparameters for 100 epochs, weight decay of 10^{-5} , and learning rate η . We also use cosine annealing as a learning rate scheduler with maximum temperature parameter of 100.

E.3.1 Disk data.

In this case, we run all pipelines with our default hyperparameters. The learning rate of Finsler MDS with gradient descent is set to $\eta = 0.001$.

E.3.2 Swiss roll.

To better preserve the manifold, we truncate the geodesic extension of the kNN graph with $k^+ = 50$. The learning rate of Finsler MDS with gradient descent is set to $\eta = 0.1$.

E.3.3 Persistence data.

To better preserve the manifold, we truncate the geodesic extension of the kNN graph with $k^+ = 300$. The learning rate of Finsler MDS with gradient descent is set to $\eta = 0.1$.

E.3.4 Classification datasets.

We took our default hyperparameters. On Imagenette, we additionally evaluated Poincaré maps [65] with default hyperparameters. It is a symmetric hyperbolic method, providing an alternative method for comparison that is non-Euclidean yet symmetric. We are not aware of non- or pseudo-Riemannian manifold learning methods and thus did not evaluate any.

E.4 Resources

All methods, whether the traditional Euclidean or our Finsler ones, do not require intensive resources: non-high end commercial CPUs are enough and no GPU is needed. To achieve this performance, advanced methods, like t-SNE and Umap and their Finsler variants, must be implemented efficiently. That is why we derive explicitly the calculation of gradients and use them in fast code, e.g. Numba’s [70] `jit` decorator in Umap. In terms of time, Euclidean and Finsler Umap are of same order of magnitude, whereas Finsler t-SNE is slower than its Euclidean counterpart. On Imagenette, using a Intel(R) Xeon(R) Gold 6348 CPU @ 2.60GHz, a single embedding (*Optimization stage*), for a default 200 iterations, takes 10s for Umap with random initialisation and 16s with the slower yet default spectral initialisation, whereas Finsler Umap takes 12s. For vanilla t-SNE, it takes around 2500s compared to 9700s for Finsler t-SNE.

F Further experiments

F.1 Toy planar data

We here perform two additional sets of experiments, regarding the number of datapoints and the embedding dimensionality. For both experiments, we present the results in fig. 10.

¹⁹When taking ω along the last axis, no rotation is needed.

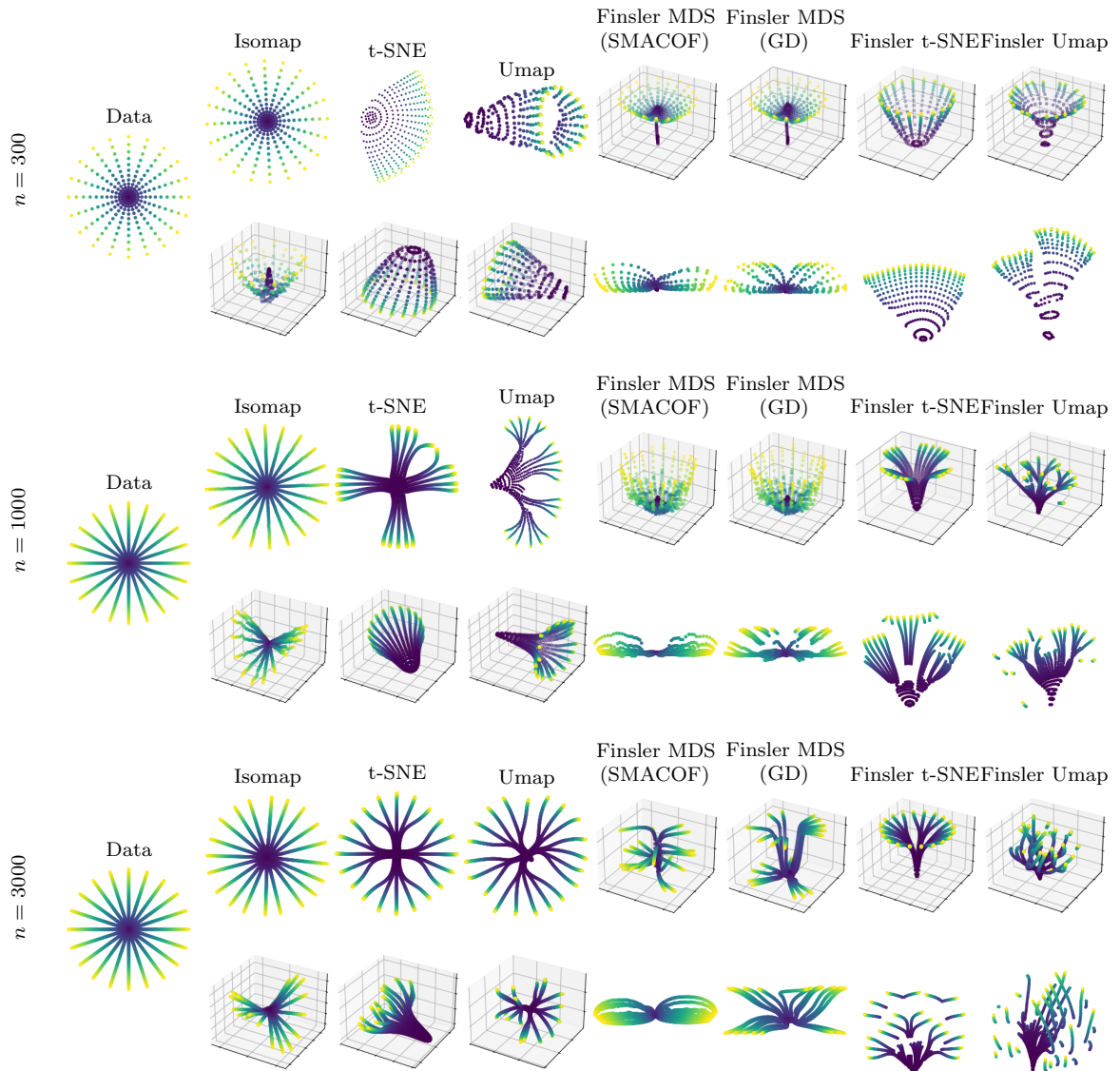


Figure 10: Embeddings of the toy planar data with non-uniform density. Each pair of rows corresponds to a different number of datapoints n , with $n = 300$ (top), $n = 1000$ (middle), and $n = 3000$ (bottom). Within each pair of plots, the top (resp. bottom) row corresponds to embedding results in the recommended (resp. unrecommended) embedding dimension, namely \mathbb{R}^2 (resp. \mathbb{R}^3) for symmetric methods and \mathbb{R}^3 (resp. \mathbb{R}^2) for asymmetric Finsler embeddings to the canonical Randers space. The last dimension of Finsler embeddings, i.e. the z -axis (resp. y -axis) in three-dimensional (resp. two-dimensional) embeddings fully encodes the asymmetry, providing more information on the data than vanilla methods like Isomap. On the other hand, traditional symmetric embedding methods do not reveal the density difference between points, unlike the Finsler embedding methods, even those that use fewer dimensions than recommended for a two-dimensional data manifold.

F.1.1 Number of datapoints.

In this experiment, we increase the number of points sampled on the unit disk from $N = 300$ to $N \in \{1000, 3000\}$, using all other parameters the same such as the number of neighbours in the kNN graph. We did not push beyond this limit as Finsler MDS greatly struggles when the number of data points scales. The first issue is the computation of a dense dissimilarity matrix \mathbf{D} due to geodesic distance calculations. As it is dense, this makes minimisation updates particular slow, for instance in the gradient descent method (GD), compared to more efficient methods like t-SNE or Umap that heavily rely on sparse dissimilarities p_{ij} to speed-up their updates. The Finsler SMACOF algorithm also heavily suffers from having many points. Unlike the original SMACOF algorithm, pseudo-inversion is required on a huge matrix of size $N^2 \times N^2$ instead of $N \times N$, which leads to many issues noticed by the original authors [37] such as instability and non-convergence. Instead, they had to rely on approximate pseudo-inverse solvers such as gmres [102] to bring down the computation time. Nevertheless, their method still cannot scale beyond a number of points of this order of magnitude, and we were not able to get any results beyond 3000 points with Finsler MDS.

By increasing the number of points, and keeping the same number of neighbours, we are artificially focusing on a more local graph. This leads to better preservation of individual branches²⁰ in traditional methods. However, t-SNE and Umap still poorly preserve the data manifold. This is because t-SNE and Umap are methods favouring clustering, with 4 main branch clusters in t-SNE and 3 main ones in Umap for $N = 3000$, rather than manifold preservation like Isomap. Isomap accurately scales with the number of points, although some deformation is visually apparent for $N = 3000$ as branches are no longer uniformly embedded angularly. Nevertheless, classical MDS is not able to provide any additional information, such as density-related information. Additionally, embedding using Isomap in a higher dimension leads to non flat embeddings, even though the original data can be perfectly embedded in a flat hyperplane of \mathbb{R}^3 , showing another weakness of this method.

At $N = 3000$, Finsler MDS becomes unstable, whether it be via the Finsler SMACOF [37] or our gradient descent implementation. This shows that Finsler MDS, while of high interest, should only be used on datasets with a small number of points, roughly around 1000 at most. For higher number of points, we must then switch to our Finsler t-SNE or Finsler Umap methods, which are based on the methods t-SNE and Umap that were designed to be used when greatly scaling up the number of datapoints. Though this will inevitably lead to a degradation in the preservation of the manifold, as these methods tend to artificially cluster, as previously discussed. That being said, both Finsler t-SNE and Finsler Umap both scale well with the number of points. As both methods are based on matching embedding dissimilarities to a sparse dissimilarity matrix, the embedding should be analysed locally rather than globally. Note though that t-SNE provides significantly better global behaviour than Umap thanks to its global normalisation of q_{ij} which comes at the cost of speed²¹. Keeping in mind the local analysis of the embeddings, lower density regions are locally embedded higher than higher density regions along the last axis (z in \mathbb{R}^3 and y in \mathbb{R}^2), providing the valuable extra information with respect to density differences that the traditional symmetric algorithms are not able to provide.

F.1.2 Embedding dimensionality.

In the seminal work [37] that introduced the canonical Randers space and how to embed asymmetric data into it, it was argued that the appropriate embedding space for Finsler

²⁰One branch corresponds to a fixed angle in polar coordinates.

²¹For a few orders of magnitude greater of N , t-SNE will be too slow for practical use and only Umap will be able to run in reasonable time among the presented method. While it is fast, we should keep in mind that it very poorly preserves the data manifold for high number of points.

embeddings is \mathbb{R}^{m+1} if comparing with symmetric methods embedding into the Euclidean space \mathbb{R}^m . This is because the canonical Randers space should be viewed as hyperplanes formed by the Euclidean space \mathbb{R}^m that are orthogonal to an extra dimension ω that fully encodes asymmetry. Thus, asymmetric datapoints lying along m -dimensional manifolds should be encoded into the canonical Randers space \mathbb{R}^{m+1} . As such, in the main paper we followed the same methodology and chose \mathbb{R}^3 as the embedding space for Finsler methods compared to \mathbb{R}^2 .

Nevertheless, we here also present, for various number of datapoints $N \in \{300, 1000, 3000\}$, the results obtained by embedding the traditional symmetric methods into the Euclidean space \mathbb{R}^3 and by embedding the Finsler methods into \mathbb{R}^2 , which is now viewed as a one-dimensional space \mathbb{R} formed by the x -axis and the y -axis encoding asymmetry. As the data manifold is two-dimensional, high deformations will necessarily occur in the canonical Randers space \mathbb{R}^2 as the one-dimensional hyperplane (a line) does not have a high enough dimension to represent accurately the two-dimensional data manifold (a disk).

Increasing the embedding dimension of traditional methods – Isomap, t-SNE, Umap – leads to incorrectly non-flat embeddings, as the original data viewed from a Riemannian perspective is perfectly flat, even for Isomap which seemed to almost perfectly embed the data in \mathbb{R}^2 for this toy problem. These new embeddings might somewhat resemble their Finsler counterparts embedded into \mathbb{R}^3 , which is to be expected as a similar type of objective is minimised. However, the Finsler versions are canonically aligned along the z -axis providing explicit information on the asymmetry in the data. On the other hand, the symmetric embeddings to \mathbb{R}^3 do not provide this information and instead the embedding is randomly rotated in \mathbb{R}^3 . Likewise, when decreasing the embedding dimensionality of Finsler methods, the original disk manifold is heavily deformed due to a one dimensional Euclidean hyperplane (x -axis) to encode a two-dimensional manifold (the disk), yet the asymmetry information is still explicitly presented through the positioning on the y -axis. In contrast, recommended embeddings to \mathbb{R}^2 of traditional methods often fails to accurately present the data, as in t-SNE or Umap, or manage to present the data accurately but without any further information.

These experiments show that the strengths of our Finsler embeddings do not result from the additional embedding dimension. They not only manage to accurately preserve the original data manifold similarly to their traditional symmetric counterparts, but they also provide additional quantitative and qualitative information regarding density differences (along geodesics) in the original data.

F.2 Toy clustered manifold

F.2.1 Data.

We draw $N = 500$ high-dimensional points in \mathbb{R}^{10} from 5 random Gaussians with exponentially decreasing sample counts. This simulates persistence data in which mixture components serve as sequential mutation states. Each agent mutates to the next state with small probability, independently of history, and mutations alter features. See section [E.1.3](#) for details.

Methods. We view the input data with PCA as it is high-dimensional. Euclidean (resp. Finsler) methods – Isomap, t-SNE, and Umap (resp. Finsler t-SNE and Umap) – embed in \mathbb{R}^2 (resp. \mathbb{R}^3). The data has hidden semantic labels, so good embeddings must form clusters to reveal them. We run Umap with and without geodesically extending the kNN graph (15 neighbours, 300 smallest edges retained) to promote global interactions and cluster hierarchy.

Results. Results appear in [figs. 7](#) and [11](#). Although the original manifold has no intrinsic asymmetry a priori, our asymmetric Finsler pipeline exposes a semantic hierarchy, either

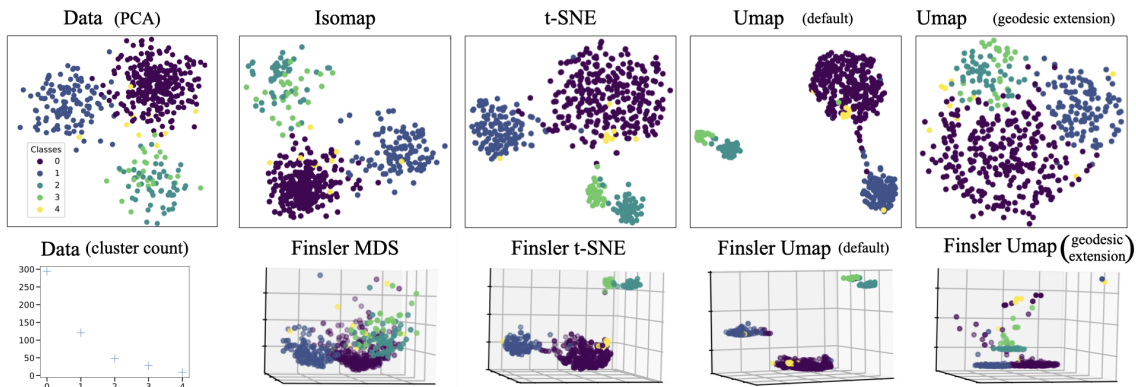


Figure 11: Embeddings of simulated mutation data with exponentially decreasing samples per groundtruth Gaussian. While traditional methods cluster, with more or less success, our Finsler approach both clusters correctly and encodes a cluster hierarchy via height, as sparser low-count clusters are embedded higher. This is shown either locally, when handling sparse dissimilarities (Finsler t-SNE, default Finsler Umap), or globally when using dense dissimilarities due to geodesic extensions of graph distances (Finsler MDS, extended Finsler Umap). This semantic hierarchy is absent in Euclidean methods. This figure is an enlarged version of fig. 7.

locally or globally: rare datapoints with more mutations (higher labels) are embedded higher than common ones with fewer mutations (lower labels). Euclidean baselines cluster but convey no hierarchy. The hierarchy is revealed thanks to asymmetric density sensitivity: as samples per Gaussian decrease, neighbourhood radii grow and cross-cluster neighbours become more likely. Dense Gaussians yield many close, same-cluster neighbours, whereas sparse Gaussians yield fewer and more distant ones, often from other clusters. Thus, our methods supplement clustering with the desired semantic ordering. These results demonstrate the potential of our approach to provide meaningful semantic information that can be useful in practice.

F.3 Reference classification datasets

F.3.1 Raw values, label-unrelated scores, and supervised scores.

In fig. 9, we summarised due to page-length constraints the results by presenting the percentage difference in mean performance²² on a few of evaluated datasets. See fig. 14 for the same plot on all evaluated datasets. Also, in tables 2 and 3, we present the raw obtained (mean and standard deviation) performance on all datasets.

Additionally, we also provide the label-unrelated scores, either in visual summary form in figs. 13 and 15 and in raw numbers in tables 2 and 3. As mentioned in the main part, our Finsler pipelines and embedding methods are systematically superior to their Euclidean counterparts on scores related to the groundtruth labels. However, on the secondary label-unrelated scores, either can be better. Recall though that it matters not to have inferior label-unrelated scores if our label-related ones are superior. When the Euclidean methods provide better label-unrelated scores, they systematically underperform compared to our Finsler ones on label-related ones. They thus tend to create “nicer looking” clusters that do not correspond to the original data manifold: points were artificially clustered together. Our Finsler approach thus provides significantly better quality embeddings that do not artificially distort the structure of the data manifold, unlike the Euclidean methods.

We also provide supervised accuracy scores in table 4. Both Finsler t-SNE and Finsler

²²The performance of our Finsler method minus that of the standard Euclidean one divided by the standard Euclidean one.

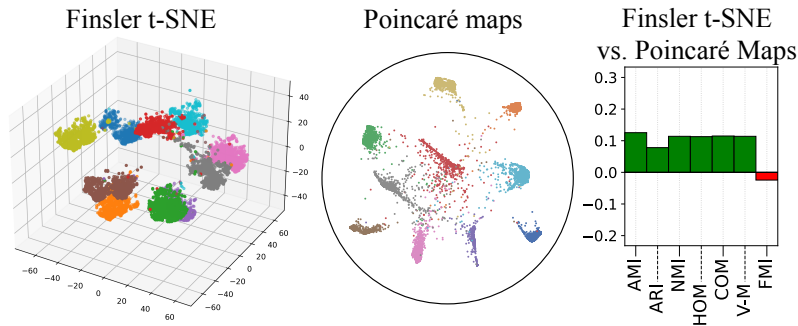


Figure 12: Imagenette: Finsler t-SNE vs. Poincaré maps, a non-Euclidean hyperbolic baseline. Right: percentage difference in kMeans scores (positive/green means Finsler t-SNE is better). The gains reveal that modelling asymmetry with Finsler geometry may capture structure better than other non-Euclidean embeddings.

Table 2: Mean clustering performance using kMeans on Umap and Finsler Umap data embeddings. The mean and standard deviation over 10 runs is presented. (+)/(-) signifies that higher/lower is better.

Dataset	Method	Label-related scores							Label-unrelated scores		
		AMI (+)	ARI (+)	NMI (+)	HOM (+)	COM (+)	V-M (+)	FMI (+)	SIL (+)	DBI (-)	CHI (+)
Iris	Umap	0.724 (± 0.248)	0.688 (± 0.241)	0.728 (± 0.245)	0.719 (± 0.243)	0.737 (± 0.247)	0.728 (± 0.245)	0.794 (± 0.159)	0.721 (± 0.019)	0.389 (± 0.025)	2526 (± 1202)
	Finsler Umap (Ours)	0.794 (± 0.024)	0.746 (± 0.032)	0.796 (± 0.023)	0.785 (± 0.026)	0.808 (± 0.020)	0.796 (± 0.023)	0.832 (± 0.020)	0.705 (± 0.036)	0.412 (± 0.047)	1471 (± 331)
MNIST	Umap	0.847 (± 0.017)	0.782 (± 0.040)	0.847 (± 0.017)	0.839 (± 0.019)	0.855 (± 0.015)	0.847 (± 0.017)	0.805 (± 0.035)	0.580 (± 0.018)	0.606 (± 0.033)	194060 (± 19078)
	Finsler Umap (Ours)	0.858 (± 0.012)	0.793 (± 0.032)	0.858 (± 0.012)	0.848 (± 0.014)	0.868 (± 0.011)	0.858 (± 0.012)	0.816 (± 0.028)	0.611 (± 0.029)	0.585 (± 0.060)	119299 (± 10201)
Fashion-MNIST	Umap	0.616 (± 0.009)	0.445 (± 0.028)	0.617 (± 0.009)	0.610 (± 0.011)	0.623 (± 0.008)	0.617 (± 0.009)	0.503 (± 0.024)	0.491 (± 0.017)	0.738 (± 0.039)	173803 (± 33633)
	Finsler Umap (Ours)	0.640 (± 0.012)	0.474 (± 0.030)	0.640 (± 0.012)	0.627 (± 0.014)	0.653 (± 0.014)	0.640 (± 0.012)	0.533 (± 0.024)	0.504 (± 0.014)	0.736 (± 0.030)	97213 (± 13424)
Kuzushiji-MNIST	Umap	0.644 (± 0.019)	0.497 (± 0.025)	0.644 (± 0.019)	0.636 (± 0.019)	0.653 (± 0.018)	0.644 (± 0.019)	0.551 (± 0.022)	0.556 (± 0.029)	0.627 (± 0.068)	117390 (± 10225)
	Finsler Umap (Ours)	0.653 (± 0.019)	0.504 (± 0.020)	0.653 (± 0.019)	0.643 (± 0.018)	0.663 (± 0.021)	0.653 (± 0.019)	0.558 (± 0.018)	0.571 (± 0.012)	0.646 (± 0.033)	60490 (± 6508)
EMNIST	Umap	0.848 (± 0.003)	0.790 (± 0.019)	0.848 (± 0.003)	0.842 (± 0.007)	0.854 (± 0.003)	0.848 (± 0.003)	0.812 (± 0.016)	0.608 (± 0.005)	0.569 (± 0.011)	175759 (± 5755)
	Finsler Umap (Ours)	0.887 (± 0.024)	0.865 (± 0.056)	0.887 (± 0.024)	0.884 (± 0.028)	0.891 (± 0.020)	0.887 (± 0.024)	0.879 (± 0.050)	0.633 (± 0.017)	0.563 (± 0.037)	114745 (± 8031)
EMNIST-Balanced	Umap	0.641 (± 0.004)	0.396 (± 0.008)	0.642 (± 0.004)	0.639 (± 0.004)	0.644 (± 0.004)	0.642 (± 0.004)	0.409 (± 0.008)	0.419 (± 0.004)	0.764 (± 0.014)	167572 (± 3708)
	Finsler Umap (Ours)	0.674 (± 0.007)	0.447 (± 0.012)	0.674 (± 0.007)	0.671 (± 0.007)	0.678 (± 0.007)	0.674 (± 0.007)	0.459 (± 0.012)	0.433 (± 0.012)	0.824 (± 0.012)	92918 (± 5118)
CIFAR10	Umap	0.654 (± 0.327)	0.619 (± 0.310)	0.654 (± 0.327)	0.651 (± 0.325)	0.656 (± 0.328)	0.654 (± 0.327)	0.658 (± 0.279)	0.585 (± 0.115)	0.570 (± 0.128)	239743 (± 98339)
	Finsler Umap (Ours)	0.817 (± 0.009)	0.767 (± 0.029)	0.817 (± 0.009)	0.812 (± 0.013)	0.822 (± 0.005)	0.817 (± 0.009)	0.791 (± 0.024)	0.647 (± 0.016)	0.516 (± 0.033)	187999 (± 11072)
CIFAR100	Umap	0.549 (± 0.183)	0.315 (± 0.105)	0.560 (± 0.179)	0.556 (± 0.178)	0.563 (± 0.180)	0.560 (± 0.179)	0.322 (± 0.104)	0.444 (± 0.036)	0.715 (± 0.030)	123871 (± 23089)
	Finsler Umap (Ours)	0.616 (± 0.002)	0.362 (± 0.005)	0.624 (± 0.002)	0.620 (± 0.003)	0.629 (± 0.002)	0.624 (± 0.002)	0.369 (± 0.005)	0.426 (± 0.002)	0.822 (± 0.013)	61756 (± 2073)
DTD	Umap	0.402 (± 0.202)	0.237 (± 0.119)	0.501 (± 0.169)	0.498 (± 0.168)	0.504 (± 0.170)	0.501 (± 0.169)	0.254 (± 0.116)	0.480 (± 0.006)	0.686 (± 0.011)	3690 (± 211)
	Finsler Umap (Ours)	0.463 (± 0.154)	0.274 (± 0.092)	0.551 (± 0.129)	0.546 (± 0.127)	0.555 (± 0.130)	0.551 (± 0.129)	0.291 (± 0.090)	0.449 (± 0.007)	0.782 (± 0.020)	1571 (± 43)
Caltech101	Umap	0.737 (± 0.246)	0.389 (± 0.130)	0.771 (± 0.214)	0.800 (± 0.222)	0.744 (± 0.206)	0.771 (± 0.214)	0.435 (± 0.139)	0.677 (± 0.006)	0.419 (± 0.008)	154548 (± 7934)
	Finsler Umap (Ours)	0.821 (± 0.004)	0.432 (± 0.016)	0.845 (± 0.003)	0.876 (± 0.003)	0.815 (± 0.004)	0.845 (± 0.003)	0.481 (± 0.016)	0.651 (± 0.007)	0.476 (± 0.017)	77907 (± 3926)
Caltech256	Umap	0.570 (± 0.290)	0.366 (± 0.183)	0.655 (± 0.238)	0.658 (± 0.239)	0.652 (± 0.237)	0.655 (± 0.238)	0.372 (± 0.184)	0.590 (± 0.005)	0.553 (± 0.010)	150961 (± 5464)
	Finsler Umap (Ours)	0.743 (± 0.001)	0.487 (± 0.009)	0.789 (± 0.001)	0.791 (± 0.001)	0.786 (± 0.001)	0.789 (± 0.001)	0.492 (± 0.009)	0.604 (± 0.011)	0.553 (± 0.010)	55076 (± 1848)
OxfordFlowers102	Umap	0.423 (± 0.212)	0.315 (± 0.158)	0.713 (± 0.105)	0.707 (± 0.104)	0.719 (± 0.106)	0.713 (± 0.105)	0.322 (± 0.157)	0.483 (± 0.007)	0.665 (± 0.014)	2583 (± 122)
	Finsler Umap (Ours)	0.571 (± 0.005)	0.429 (± 0.008)	0.785 (± 0.002)	0.775 (± 0.003)	0.795 (± 0.003)	0.785 (± 0.002)	0.437 (± 0.007)	0.483 (± 0.009)	0.722 (± 0.019)	3652 (± 526)
OxfordIIITPet	Umap	0.720 (± 0.362)	0.646 (± 0.323)	0.735 (± 0.342)	0.732 (± 0.341)	0.739 (± 0.344)	0.735 (± 0.342)	0.656 (± 0.315)	0.701 (± 0.006)	0.426 (± 0.024)	105243 (± 5334)
	Finsler Umap (Ours)	0.885 (± 0.005)	0.760 (± 0.016)	0.892 (± 0.005)	0.884 (± 0.006)	0.899 (± 0.005)	0.892 (± 0.005)	0.768 (± 0.015)	0.670 (± 0.013)	0.478 (± 0.040)	86351 (± 6526)
GTSRB	Umap	0.444 (± 0.223)	0.296 (± 0.104)	0.449 (± 0.220)	0.455 (± 0.223)	0.443 (± 0.217)	0.449 (± 0.220)	0.233 (± 0.100)	0.411 (± 0.008)	0.779 (± 0.018)	34781 (± 1412)
	Finsler Umap (Ours)	0.515 (± 0.010)	0.231 (± 0.010)	0.520 (± 0.010)	0.523 (± 0.010)	0.517 (± 0.010)	0.520 (± 0.010)	0.258 (± 0.010)	0.473 (± 0.007)	0.930 (± 0.024)	9529 (± 430)
Imagenette	Umap	0.750 (± 0.375)	0.756 (± 0.378)	0.751 (± 0.374)	0.751 (± 0.375)	0.751 (± 0.374)	0.751 (± 0.374)	0.781 (± 0.340)	0.830 (± 0.005)	0.253 (± 0.007)	161823 (± 11371)
	Finsler Umap (Ours)	0.846 (± 0.282)	0.852 (± 0.284)	0.846 (± 0.281)	0.867 (± 0.255)	0.828 (± 0.006)	0.268 (± 0.016)	97813 (± 6251)			
Imagenet	Umap	0.784 (± 0.000)	0.506 (± 0.001)	0.797 (± 0.000)	0.793 (± 0.000)	0.802 (± 0.000)	0.797 (± 0.000)	0.508 (± 0.001)	0.582 (± 0.002)	0.570 (± 0.003)	7315700 (± 51432)
	Finsler Umap (Ours)	0.803 (± 0.001)	0.540 (± 0.003)	0.816 (± 0.001)	0.810 (± 0.001)	0.821 (± 0.001)	0.816 (± 0.001)	0.542 (± 0.003)	0.615 (± 0.004)	0.565 (± 0.007)	1930520 (± 28049)

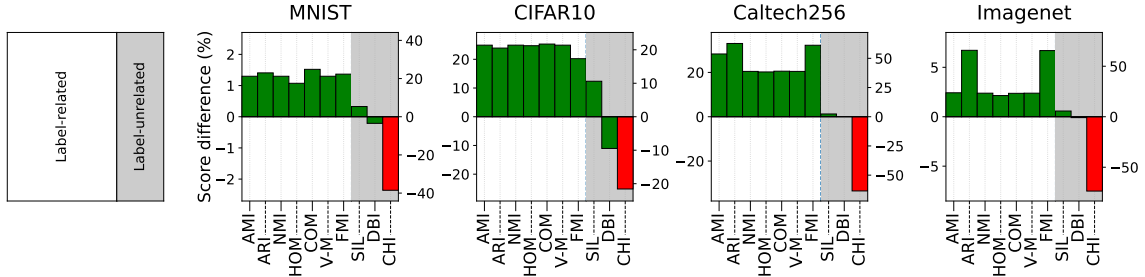
Umap consistently outperform their Euclidean baselines by large magnitudes²³. The supervised evaluation thus supports the findings from the unsupervised scores, namely that our asymmetric Finsler pipeline is beneficial compared to the traditional symmetric one.

F.3.2 Non-Euclidean symmetric method.

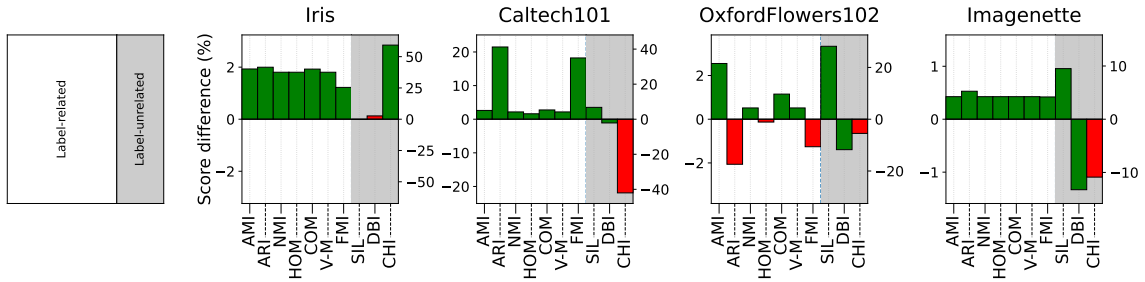
We provide the embedding results of the hyperbolic method Poincaré maps in fig. 12. Finsler t-SNE outperforms Poincaré maps on all scores²⁴. Thus, our Finsler approach yields better quality embeddings than the reference hyperbolic method in this experiment, and as demonstrated in the US cities experiment (fig. 1) it also reveals additional information that is discarded in symmetric methods, including Poincaré maps. Thus, not only is our Finsler pipeline superior to the traditional one, outperforming the modern reference methods (t-SNE and Umap), it can surpass competitive methods using non-trivial changes of geometry, such as hyperbolic geometry.

²³Or they are on par with the baselines.

²⁴Except the FMI where it is on par.



Finsler Umap vs. Umap



Finsler t-SNE vs. t-SNE

Figure 13: Percentage difference in mean performance between our Finsler methods and their traditional Euclidean baselines. Positive (resp. negative) differences, in green (resp. red) signifies we get better (resp. worse) scores evaluating the quality of kMeans clusters, either by comparing with groundtruth class labels or not. See fig. 15. Raw performance values and standard deviations are pushed to tables 2 and 3. This figure is the same as fig. 9, except that we added to the label-related scores, in white background, the label-unrelated scores, in grey background. Having better label-unrelated score with worse label-related scores is particular bad, as it means that the method is artificially creating “nicely looking” clusters that do not correspond to the reality of the data manifold. This never happens for our Finsler methods, as we systematically have better label-related measures.

Table 3: Clustering performance using kMeans on t-SNE and Finsler t-SNE embeddings across the smaller datasets. (+)/(-) signifies that higher/lower is better.

Dataset	Method	Label-related scores							Label-unrelated scores		
		AMI (+)	ARI (+)	NMI (+)	HOM (+)	COM (+)	V-M (+)	FMI (+)	SIL (+)	DBI (-)	CHI (+)
Iris	t-SNE	0.829	0.851	0.831	0.831	0.831	0.831	0.900	0.665	0.453	3028
	Finsler t-SNE (Ours)	0.845	0.868	0.846	0.846	0.847	0.846	0.911	0.664	0.465	4822
DTD	t-SNE	0.498	0.288	0.581	0.578	0.584	0.581	0.303	0.402	0.804	2492
	Finsler t-SNE (Ours)	0.504	0.294	0.585	0.580	0.590	0.585	0.310	0.408	0.859	1186
Caltech101	t-SNE	0.804	0.377	0.830	0.865	0.798	0.830	0.428	0.547	0.610	23151
	Finsler t-SNE (Ours)	0.825	0.458	0.848	0.879	0.820	0.848	0.506	0.584	0.597	13419
OxfordFlowers102	t-SNE	0.549	0.388	0.775	0.767	0.783	0.775	0.397	0.419	0.740	1788
	Finsler t-SNE (Ours)	0.563	0.380	0.779	0.766	0.792	0.779	0.392	0.537	0.653	1690
OxfordIIITPet	t-SNE	0.899	0.814	0.904	0.900	0.908	0.904	0.819	0.607	0.554	15824
	Finsler t-SNE (Ours)	0.903	0.821	0.908	0.904	0.913	0.908	0.826	0.618	0.556	13912
Imagenette	t-SNE	0.939	0.946	0.939	0.939	0.939	0.939	0.951	0.610	0.536	22051
	Finsler t-SNE (Ours)	0.943	0.951	0.943	0.943	0.943	0.943	0.955	0.668	0.465	19651

Table 4: Supervised accuracy on image benchmarks for two classifiers. We report mean test accuracy over 2-stratified 5-fold CV (10 runs). Best/ties are bold/underlined. Finsler variants consistently outperform Euclidean ones, as suggested already by the unsupervised scores.

Supervised Evaluator	Embedding	DTD	Caltech101	OxfordFlowers102	OxfordIIITPet	Imagenette
5-NN classifier	UMAP	0.51	0.87	0.55	0.92	<u>0.98</u>
	Finsler UMAP	0.56	0.88	0.62	0.93	<u>0.98</u>
	t-SNE	0.57	<u>0.88</u>	0.63	<u>0.92</u>	<u>0.98</u>
	Finsler t-SNE	0.58	<u>0.88</u>	0.62	<u>0.92</u>	<u>0.98</u>
Linear classifier	UMAP	0.34	0.53	0.37	0.80	0.97
	Finsler UMAP	0.43	0.66	0.48	0.87	0.98
	t-SNE	0.33	0.55	0.29	0.90	<u>0.98</u>
	Finsler t-SNE	0.42	0.76	0.38	0.91	<u>0.98</u>

F.3.3 Full visualisations.

We provide embedding visualisations on all datasets in fig. 16, extending fig. 8, for traditional Euclidean Umap and t-SNE and our Finsler Umap and Finsler t-SNE counterparts. A random embedding was chosen for both traditional Euclidean and our Finsler Umap.

Additionally, we also provide embedding visualisations in fig. 17 using unrecommended embedding dimensions, namely \mathbb{R}^3 for Euclidean-based methods, instead of \mathbb{R}^2 , and \mathbb{R}^2 for Finsler-based methods, instead of \mathbb{R}^3 . These experiments demonstrate that the success of Finsler-based methods is not due to the extra embedding dimension but to the asymmetric perspective on the data combined with the asymmetric structure of the embedding space.

F.3.4 Embedding dimensionality.

We evaluated both Umap and our Finsler Umap pipelines when increasing the embedding dimensionality²⁵ $d \in \{2, 5, 10, 50\}$ of the CIFAR10, OxfordFlowers102, and Imagenette datasets. We provide in table 5 quantitative kMeans clustering performance on these embeddings. When increasing the dimensions, our asymmetric approach still consistently yields better performance according to scores related to the labels, and thus to the data manifold. Nevertheless, the gap between the traditional Euclidean and our Finsler pipelines virtually vanishes in very high dimensions. This suggests that our unusual asymmetric perspective for analysing traditionally considered symmetric data is mostly beneficial when embedding data in low rather than high dimensions. Remember though that in manifold or representation learning, low dimensional, and not high dimensional, embeddings are the holy grail to search for. This means that our asymmetric Finsler perspective is not only

²⁵Recall that for dimensionality d , Umap embeds in \mathbb{R}^d while Finsler Umap embeds in \mathbb{R}^{d+1} , following the methodology of [37].

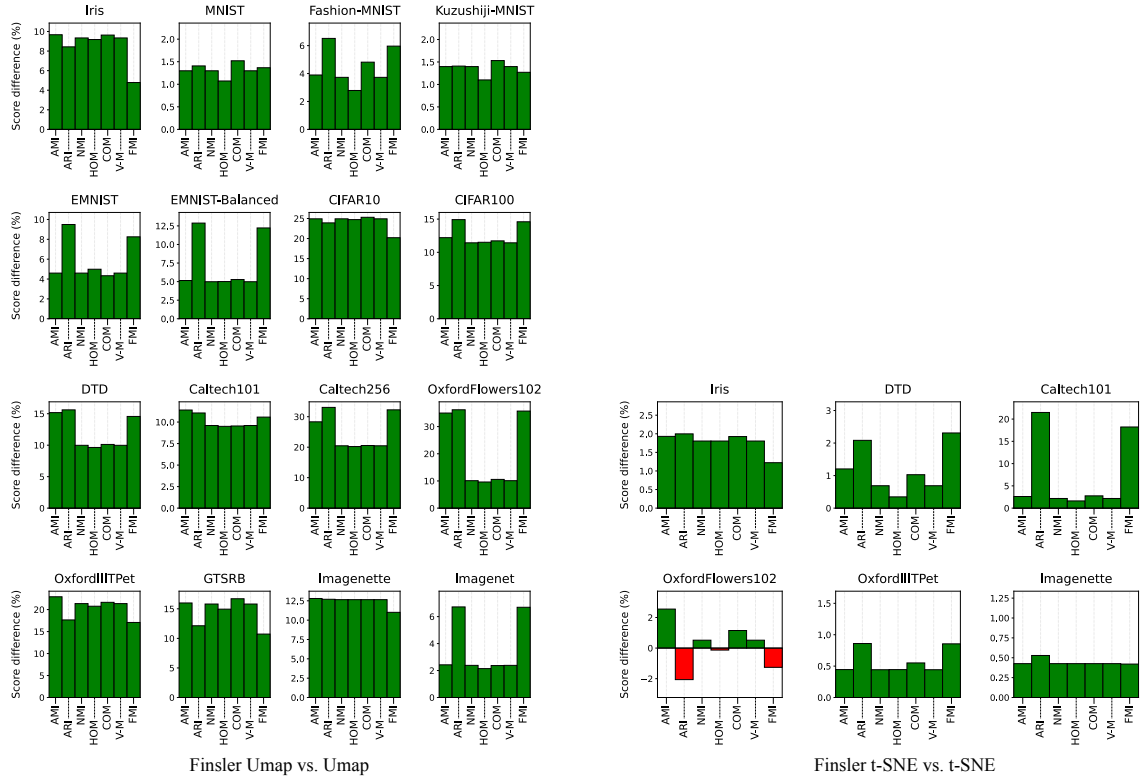


Figure 14: Complete version of fig. 9 for all tested datasets, presenting the percentage difference in mean performance between our Finsler methods and their traditional Euclidean baselines. Positive (resp. negative) differences, in green (resp. red) signifies we get better (resp. worse) scores comparing kMeans clustering with groundtruth class labels. Raw performance values are in tables 2 and 3.

beneficial, it is noticeably superior in the settings that matter in practice.

F.3.5 Levels of emphasis on asymmetry.

The canonical Randers space used as embedding space of the Finsler-based methods depends on the choice of linear drift component ω . While its orientation matters little, with the vertical upwards orientation being equivalent to any others by simply rotating the resulting embeddings, its magnitude $\|\omega\|_2 \in [0, 1)$ is however important. Increasing $\|\omega\|_2$ puts more emphasis on preserving asymmetry and fits well to cases with high levels of asymmetry. When $\omega \rightarrow 0$, the embedding space becomes approximately Euclidean, which suits cases of data with little asymmetry. As such, we recommend tuning $\|\omega\|_2$ to each task rather than choosing a default value, like $\|\omega\|_2 = 0.5$ as in the set of visual experiments in [37]. In the results reported in the main paper (tables 2 and 3), we reported the results obtained with $\|\omega\|_2 \in \{0.001, 0.01, 0.1, 0.5\}$ providing the highest mean AMI score. In tables 6 and 7, we provide full results for all tested $\|\omega\|_2$. For almost all datasets, the mean scores, and in particular the AMI, for most if not all tested levels of $\|\omega\|_2$ is superior to that of traditional Umap. These results demonstrate that our Finsler pipeline is robust to choices of $\|\omega\|_2$. They also reveal the benefit of appropriately tuning $\|\omega\|_2$ for each task in order to provide the embedding that best captures the data and its natural asymmetry.

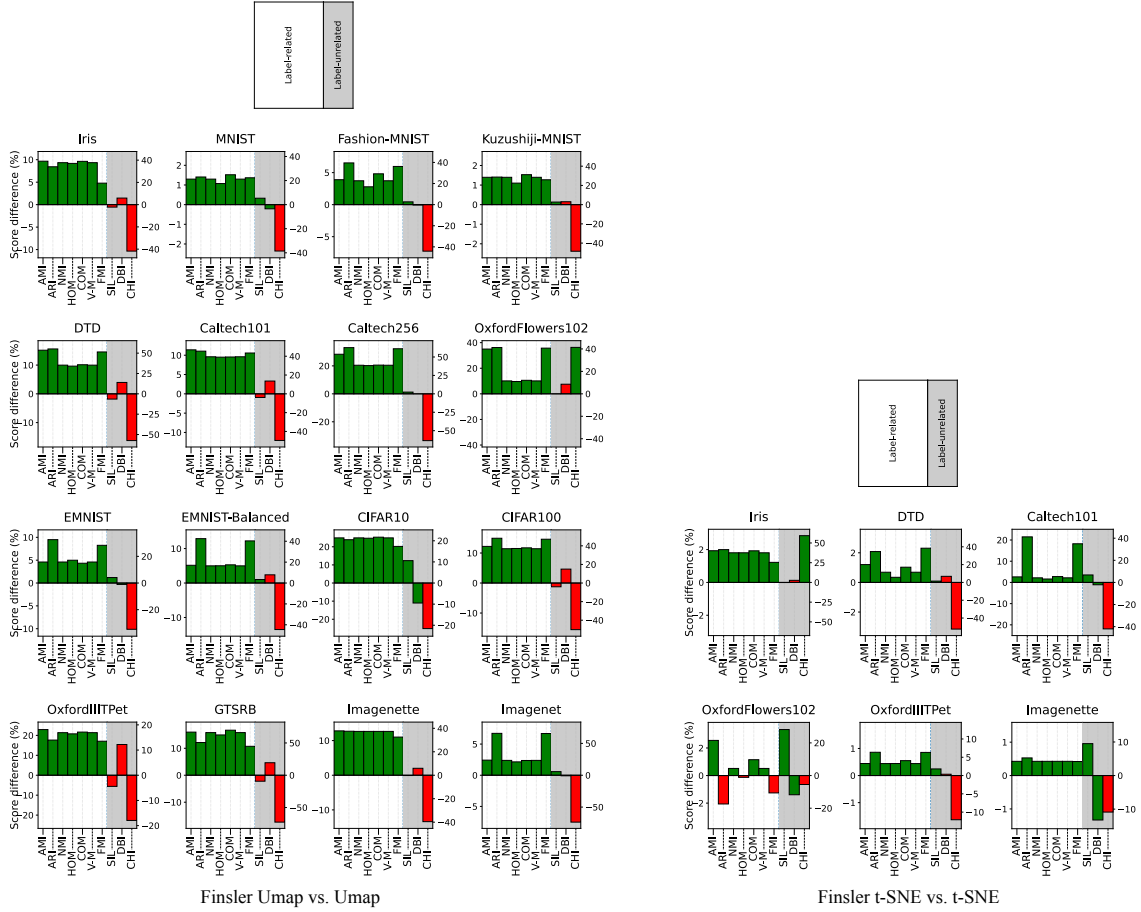


Figure 15: Complete version of fig. 13 for all datasets, presenting the percentage difference in mean performance between our Finsler methods and their traditional Euclidean baselines. Positive (resp. negative) differences, in green (resp. red) signifies we get better (resp. worse) evaluating the quality of kMeans clusters, either by comparing with groundtruth class labels or not. Raw performance values are in tables 2 and 3. This figure is the same as fig. 14, except that we added to the label-related scores, in white background, the label-unrelated scores, in grey background. Having better label-unrelated score with worse label-related scores is particular bad, as it means that the method is artificially creating “nicely looking” clusters that do not correspond to the reality of the data manifold. This never happens for our Finsler methods, as we systematically have better label-related measures.

Table 5: Mean clustering performance using kMeans on Umap and Finsler Umap data embeddings with varying dimensionality d . The mean and standard deviation over 10 runs is presented. (+)/(-) signifies that higher/lower is better.

Dataset	Method	Dimensionality d	Label-related scores							Label-unrelated scores		
			AMI (+)	ARI (+)	NMI (+)	HOM (+)	COM (+)	V-M (+)	FMI (+)	SIL (+)	DBI (-)	CH (+)
CIFAR10	Umap	2	0.654 (± 0.327)	0.619 (± 0.310)	0.654 (± 0.327)	0.651 (± 0.325)	0.656 (± 0.328)	0.654 (± 0.327)	0.658 (± 0.279)	0.585 (± 0.115)	0.570 (± 0.128)	239743 (± 98339)
	Finsler Umap (Ours)	2	0.817 (± 0.009)	0.767 (± 0.029)	0.817 (± 0.009)	0.812 (± 0.013)	0.822 (± 0.005)	0.817 (± 0.009)	0.791 (± 0.024)	0.647 (± 0.016)	0.516 (± 0.033)	187999 (± 11072)
	Umap	5	0.814 (± 0.011)	0.763 (± 0.023)	0.814 (± 0.011)	0.810 (± 0.012)	0.819 (± 0.009)	0.814 (± 0.011)	0.788 (± 0.020)	0.634 (± 0.013)	0.546 (± 0.038)	228691 (± 12209)
	Finsler Umap (Ours)	5	0.815 (± 0.011)	0.767 (± 0.025)	0.815 (± 0.011)	0.811 (± 0.013)	0.820 (± 0.009)	0.815 (± 0.011)	0.791 (± 0.021)	0.638 (± 0.015)	0.541 (± 0.045)	173549 (± 11579)
	Umap	10	0.816 (± 0.010)	0.770 (± 0.014)	0.816 (± 0.010)	0.812 (± 0.010)	0.820 (± 0.009)	0.816 (± 0.010)	0.794 (± 0.012)	0.637 (± 0.012)	0.538 (± 0.034)	233395 (± 9628)
	Finsler Umap (Ours)	10	0.816 (± 0.011)	0.759 (± 0.038)	0.816 (± 0.011)	0.809 (± 0.017)	0.823 (± 0.006)	0.816 (± 0.011)	0.785 (± 0.032)	0.632 (± 0.030)	0.555 (± 0.072)	160470 (± 20810)
OxfordFlowers102	Umap	50	0.807 (± 0.017)	0.752 (± 0.034)	0.807 (± 0.017)	0.801 (± 0.021)	0.813 (± 0.014)	0.807 (± 0.017)	0.778 (± 0.029)	0.630 (± 0.013)	0.561 (± 0.040)	217258 (± 30880)
	Finsler Umap (Ours)	50	0.816 (± 0.010)	0.763 (± 0.030)	0.816 (± 0.010)	0.810 (± 0.014)	0.822 (± 0.006)	0.816 (± 0.010)	0.788 (± 0.026)	0.641 (± 0.014)	0.540 (± 0.045)	143102 (± 8470)
	Umap	2	0.423 (± 0.212)	0.315 (± 0.158)	0.713 (± 0.105)	0.707 (± 0.104)	0.719 (± 0.106)	0.713 (± 0.105)	0.322 (± 0.157)	0.483 (± 0.007)	0.665 (± 0.014)	2583 (± 122)
	Finsler Umap (Ours)	2	0.571 (± 0.005)	0.429 (± 0.008)	0.785 (± 0.002)	0.775 (± 0.003)	0.795 (± 0.003)	0.785 (± 0.002)	0.437 (± 0.007)	0.483 (± 0.009)	0.722 (± 0.019)	3652 (± 526)
	Umap	5	0.568 (± 0.005)	0.428 (± 0.007)	0.785 (± 0.003)	0.776 (± 0.003)	0.793 (± 0.002)	0.785 (± 0.003)	0.436 (± 0.006)	0.429 (± 0.005)	0.849 (± 0.013)	683 (± 27)
	Finsler Umap (Ours)	5	0.587 (± 0.006)	0.441 (± 0.009)	0.793 (± 0.003)	0.783 (± 0.003)	0.803 (± 0.003)	0.793 (± 0.003)	0.449 (± 0.009)	0.443 (± 0.006)	0.830 (± 0.007)	633 (± 29)
Imagenette	Umap	10	0.569 (± 0.004)	0.428 (± 0.007)	0.785 (± 0.002)	0.776 (± 0.003)	0.793 (± 0.002)	0.785 (± 0.002)	0.436 (± 0.007)	0.419 (± 0.008)	0.880 (± 0.026)	618 (± 17)
	Finsler Umap (Ours)	10	0.589 (± 0.006)	0.440 (± 0.007)	0.793 (± 0.003)	0.783 (± 0.003)	0.804 (± 0.003)	0.793 (± 0.003)	0.449 (± 0.006)	0.432 (± 0.010)	0.846 (± 0.023)	690 (± 12)
	Umap	50	0.569 (± 0.006)	0.426 (± 0.009)	0.784 (± 0.003)	0.775 (± 0.004)	0.795 (± 0.003)	0.784 (± 0.003)	0.434 (± 0.009)	0.411 (± 0.009)	0.888 (± 0.019)	617 (± 17)
	Finsler Umap (Ours)	50	0.585 (± 0.006)	0.437 (± 0.010)	0.792 (± 0.003)	0.782 (± 0.004)	0.802 (± 0.003)	0.792 (± 0.003)	0.445 (± 0.009)	0.425 (± 0.007)	0.867 (± 0.018)	612 (± 24)
	Umap	2	0.759 (± 0.375)	0.756 (± 0.378)	0.751 (± 0.374)	0.751 (± 0.375)	0.751 (± 0.374)	0.751 (± 0.374)	0.781 (± 0.340)	0.880 (± 0.005)	0.867 (± 0.007)	161823 (± 11371)
	Finsler Umap (Ours)	2	0.846 (± 0.282)	0.852 (± 0.284)	0.846 (± 0.281)	0.867 (± 0.255)	0.828 (± 0.006)	0.298 (± 0.016)	97813 (± 46251)			
Imagenet	Umap	5	0.941 (± 0.001)	0.947 (± 0.001)	0.941 (± 0.001)	0.942 (± 0.001)	0.953 (± 0.000)	0.848 (± 0.002)	2.241 (± 0.004)			
	Finsler Umap (Ours)	5	0.941 (± 0.001)	0.948 (± 0.001)	0.942 (± 0.001)	0.942 (± 0.001)	0.941 (± 0.001)	0.941 (± 0.001)	0.942 (± 0.001)	0.953 (± 0.000)	0.840 (± 0.002)	9325 (± 2307)
	Umap	10	0.941 (± 0.001)	0.947 (± 0.001)	0.941 (± 0.001)	0.953 (± 0.000)	0.849 (± 0.001)	132728 (± 3277)				
	Finsler Umap (Ours)	10	0.941 (± 0.001)	0.948 (± 0.001)	0.941 (± 0.001)	0.953 (± 0.000)	0.834 (± 0.003)	2.241 (± 0.006)				
	Umap	50	0.941 (± 0.001)	0.947 (± 0.000)	0.941 (± 0.001)	0.953 (± 0.000)	0.848 (± 0.002)	127384 (± 2830)				
	Finsler Umap (Ours)	50	0.941 (± 0.001)	0.948 (± 0.000)	0.941 (± 0.001)	0.953 (± 0.000)	0.840 (± 0.001)	88716 (± 1271)				

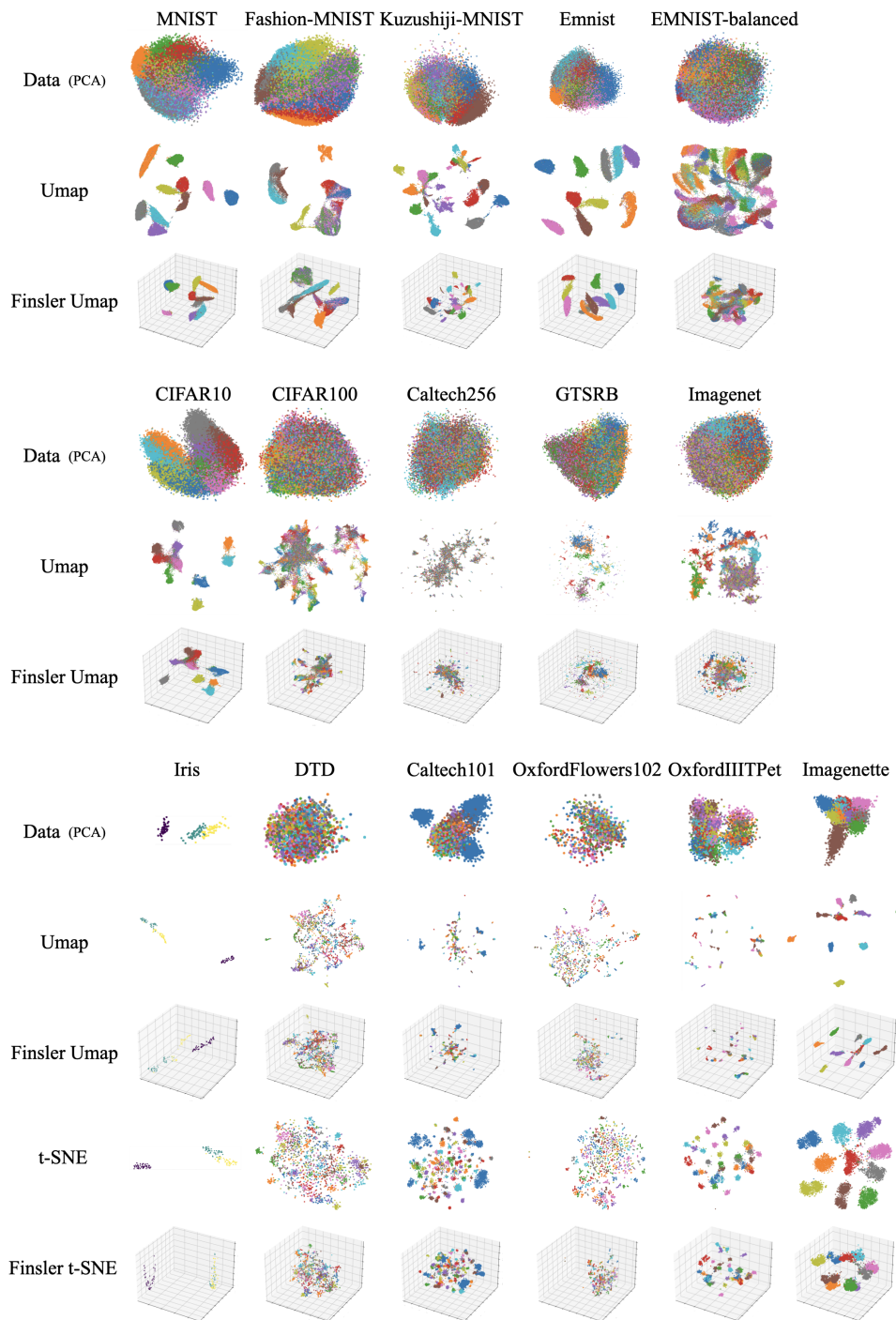


Figure 16: Embeddings results, using recommended embedding dimensions, on all our tested reference classification datasets using either traditional Euclidean methods or our Finsler pipelines.

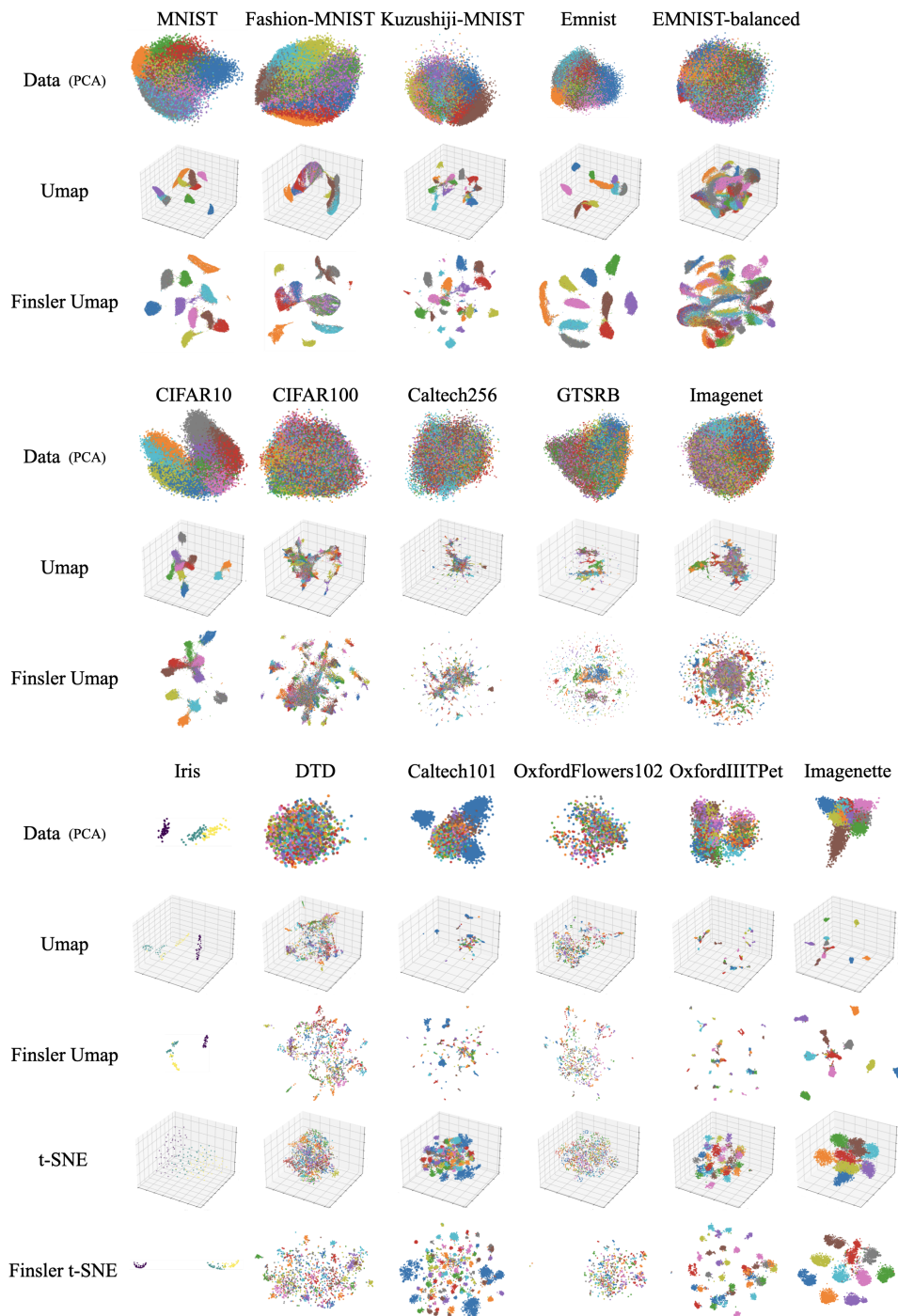


Figure 17: Embeddings results, using unrecommended embedding dimensions, on all our tested reference classification datasets using either traditional Euclidean methods or our Finsler pipelines.

Table 6: Mean clustering performance using kMeans on Umap and Finsler Umap data embeddings. We use various levels of emphasis for metric asymmetry, via $\|\omega\|_2 \in \{0.001, 0.01, 0.1, 0.5\}$, in the embedding space of the Finsler methods. The mean and standard deviation over 10 runs is presented. (+)/(-) signifies that higher/lower is better.

Dataset	Method	$\ \omega\ _2$	Label-related scores						Label-unrelated scores			
			AMI (+)	ARI (+)	NMI (+)	ROM (+)	COM (+)	V-M (+)	FMI (+)	SIL (-)	DBI (-)	CHI (+)
Iris	Umap	—	0.724 (±0.248)	0.688 (±0.241)	0.728 (±0.245)	0.719 (±0.243)	0.737 (±0.247)	0.728 (±0.245)	0.794 (±0.159)	0.721 (±0.019)	0.389 (±0.025)	2526 (±1202)
	Finsler Umap (Ours)	0.5	0.626 (±0.313)	0.584 (±0.293)	0.630 (±0.309)	0.620 (±0.304)	0.641 (±0.314)	0.630 (±0.309)	0.726 (±0.194)	0.742 (±0.063)	0.418 (±0.113)	912 (±778)
	Finsler Umap (Ours)	0.1	0.719 (±0.242)	0.677 (±0.228)	0.723 (±0.239)	0.713 (±0.236)	0.732 (±0.242)	0.723 (±0.239)	0.786 (±0.151)	0.731 (±0.021)	0.382 (±0.027)	1760 (±493)
	Finsler Umap (Ours)	0.01	0.722 (±0.243)	0.683 (±0.230)	0.726 (±0.240)	0.717 (±0.237)	0.735 (±0.243)	0.726 (±0.240)	0.790 (±0.152)	0.717 (±0.018)	0.402 (±0.031)	1485 (±275)
	Finsler Umap (Ours)	0.001	0.794 (±0.024)	0.746 (±0.032)	0.796 (±0.023)	0.785 (±0.026)	0.808 (±0.020)	0.796 (±0.023)	0.832 (±0.020)	0.705 (±0.036)	0.412 (±0.047)	1471 (±331)
MNIST	Umap	—	0.847 (±0.017)	0.782 (±0.040)	0.847 (±0.017)	0.839 (±0.019)	0.855 (±0.015)	0.847 (±0.017)	0.805 (±0.035)	0.580 (±0.018)	0.606 (±0.033)	104060 (±19078)
	Finsler Umap (Ours)	0.5	0.832 (±0.029)	0.757 (±0.052)	0.832 (±0.029)	0.823 (±0.032)	0.842 (±0.026)	0.832 (±0.029)	0.783 (±0.046)	0.550 (±0.028)	0.687 (±0.071)	96743 (±11252)
	Finsler Umap (Ours)	0.1	0.633 (±0.015)	0.456 (±0.017)	0.633 (±0.015)	0.621 (±0.014)	0.646 (±0.018)	0.633 (±0.015)	0.516 (±0.014)	0.503 (±0.020)	0.734 (±0.050)	107025 (±14459)
	Finsler Umap (Ours)	0.01	0.858 (±0.012)	0.793 (±0.032)	0.858 (±0.012)	0.848 (±0.014)	0.868 (±0.011)	0.858 (±0.012)	0.816 (±0.028)	0.611 (±0.029)	0.585 (±0.060)	119299 (±10201)
	Finsler Umap (Ours)	0.001	0.856 (±0.014)	0.801 (±0.040)	0.856 (±0.014)	0.850 (±0.017)	0.862 (±0.012)	0.856 (±0.014)	0.823 (±0.035)	0.604 (±0.021)	0.597 (±0.047)	126533 (±10462)
Fashion-MNIST	Umap	—	0.616 (±0.009)	0.445 (±0.028)	0.617 (±0.009)	0.610 (±0.011)	0.623 (±0.008)	0.617 (±0.009)	0.503 (±0.024)	0.491 (±0.017)	0.738 (±0.039)	173803 (±2963)
	Finsler Umap (Ours)	0.5	0.624 (±0.015)	0.440 (±0.034)	0.624 (±0.015)	0.614 (±0.018)	0.634 (±0.015)	0.624 (±0.015)	0.501 (±0.028)	0.499 (±0.013)	0.741 (±0.041)	100874 (±22041)
	Finsler Umap (Ours)	0.1	0.640 (±0.012)	0.474 (±0.030)	0.640 (±0.012)	0.627 (±0.014)	0.653 (±0.014)	0.640 (±0.012)	0.533 (±0.024)	0.504 (±0.014)	0.736 (±0.030)	97213 (±13424)
	Finsler Umap (Ours)	0.01	0.635 (±0.021)	0.474 (±0.022)	0.635 (±0.021)	0.626 (±0.017)	0.645 (±0.026)	0.635 (±0.021)	0.531 (±0.022)	0.488 (±0.028)	0.795 (±0.086)	98307 (±10707)
	Finsler Umap (Ours)	0.001	0.644 (±0.019)	0.497 (±0.025)	0.644 (±0.019)	0.636 (±0.019)	0.653 (±0.018)	0.644 (±0.019)	0.551 (±0.022)	0.556 (±0.029)	0.627 (±0.068)	117390 (±10225)
Kuzushiji-MNIST	Umap	—	0.644 (±0.021)	0.501 (±0.031)	0.644 (±0.021)	0.634 (±0.023)	0.654 (±0.020)	0.644 (±0.021)	0.555 (±0.027)	0.542 (±0.025)	0.692 (±0.051)	51443 (±6543)
	Finsler Umap (Ours)	0.5	0.653 (±0.019)	0.504 (±0.020)	0.653 (±0.019)	0.643 (±0.018)	0.663 (±0.021)	0.653 (±0.019)	0.558 (±0.018)	0.571 (±0.012)	0.646 (±0.033)	60490 (±6508)
	Finsler Umap (Ours)	0.1	0.635 (±0.011)	0.486 (±0.021)	0.635 (±0.011)	0.625 (±0.011)	0.645 (±0.011)	0.635 (±0.011)	0.542 (±0.017)	0.560 (±0.021)	0.664 (±0.061)	57863 (±7456)
	Finsler Umap (Ours)	0.01	0.652 (±0.020)	0.509 (±0.037)	0.652 (±0.020)	0.643 (±0.023)	0.661 (±0.017)	0.652 (±0.020)	0.562 (±0.031)	0.559 (±0.028)	0.680 (±0.058)	56887 (±7173)
	Finsler Umap (Ours)	0.001	0.848 (±0.003)	0.790 (±0.019)	0.848 (±0.003)	0.842 (±0.007)	0.854 (±0.003)	0.848 (±0.003)	0.812 (±0.016)	0.608 (±0.005)	0.569 (±0.011)	175750 (±5755)
EMNIST	Umap	—	0.641 (±0.004)	0.396 (±0.008)	0.642 (±0.004)	0.639 (±0.004)	0.644 (±0.004)	0.642 (±0.004)	0.409 (±0.008)	0.419 (±0.004)	0.764 (±0.014)	167572 (±3708)
	Finsler Umap (Ours)	0.5	0.674 (±0.007)	0.447 (±0.012)	0.674 (±0.007)	0.671 (±0.007)	0.678 (±0.007)	0.674 (±0.007)	0.459 (±0.012)	0.433 (±0.006)	0.824 (±0.012)	92918 (±5118)
	Finsler Umap (Ours)	0.1	0.668 (±0.003)	0.437 (±0.008)	0.669 (±0.003)	0.665 (±0.003)	0.672 (±0.003)	0.669 (±0.003)	0.450 (±0.007)	0.446 (±0.010)	0.839 (±0.024)	94983 (±4762)
	Finsler Umap (Ours)	0.01	0.869 (±0.027)	0.817 (±0.056)	0.869 (±0.027)	0.861 (±0.029)	0.877 (±0.026)	0.869 (±0.027)	0.837 (±0.050)	0.624 (±0.032)	0.570 (±0.075)	109198 (±14587)
	Finsler Umap (Ours)	0.001	0.887 (±0.024)	0.865 (±0.056)	0.887 (±0.024)	0.884 (±0.028)	0.891 (±0.020)	0.887 (±0.024)	0.879 (±0.050)	0.633 (±0.017)	0.563 (±0.037)	114745 (±8031)
EMNIST-Balanced	Umap	—	0.654 (±0.327)	0.619 (±0.310)	0.654 (±0.327)	0.651 (±0.325)	0.656 (±0.328)	0.654 (±0.327)	0.658 (±0.279)	0.585 (±0.115)	0.570 (±0.128)	239743 (±98339)
	Finsler Umap (Ours)	0.5	0.707 (±0.236)	0.643 (±0.217)	0.707 (±0.236)	0.698 (±0.233)	0.717 (±0.239)	0.707 (±0.236)	0.681 (±0.196)	0.541 (±0.082)	0.686 (±0.116)	102787 (±25852)
	Finsler Umap (Ours)	0.1	0.732 (±0.244)	0.689 (±0.231)	0.732 (±0.244)	0.728 (±0.243)	0.737 (±0.246)	0.732 (±0.244)	0.721 (±0.208)	0.607 (±0.104)	0.574 (±0.147)	159475 (±46970)
	Finsler Umap (Ours)	0.01	0.809 (±0.011)	0.752 (±0.029)	0.809 (±0.011)	0.802 (±0.014)	0.816 (±0.009)	0.809 (±0.011)	0.778 (±0.025)	0.639 (±0.018)	0.534 (±0.047)	174967 (±13199)
	Finsler Umap (Ours)	0.001	0.817 (±0.009)	0.767 (±0.029)	0.817 (±0.009)	0.812 (±0.013)	0.822 (±0.005)	0.817 (±0.009)	0.791 (±0.024)	0.647 (±0.016)	0.516 (±0.033)	187999 (±11072)
CIFAR10	Umap	—	0.549 (±0.183)	0.315 (±0.105)	0.560 (±0.179)	0.556 (±0.178)	0.563 (±0.180)	0.560 (±0.179)	0.322 (±0.104)	0.444 (±0.036)	0.715 (±0.030)	123871 (±23089)
	Finsler Umap (Ours)	0.5	0.549 (±0.183)	0.321 (±0.107)	0.560 (±0.179)	0.554 (±0.177)	0.565 (±0.181)	0.560 (±0.179)	0.329 (±0.107)	0.411 (±0.047)	0.845 (±0.050)	74769 (±17273)
	Finsler Umap (Ours)	0.1	0.554 (±0.185)	0.324 (±0.108)	0.564 (±0.181)	0.560 (±0.179)	0.569 (±0.182)	0.564 (±0.181)	0.332 (±0.107)	0.411 (±0.048)	0.833 (±0.056)	57757 (±13248)
	Finsler Umap (Ours)	0.01	0.555 (±0.185)	0.323 (±0.108)	0.565 (±0.181)	0.560 (±0.179)	0.569 (±0.182)	0.565 (±0.181)	0.331 (±0.107)	0.408 (±0.047)	0.835 (±0.058)	56631 (±13153)
	Finsler Umap (Ours)	0.001	0.616 (±0.002)	0.362 (±0.005)	0.624 (±0.002)	0.620 (±0.003)	0.629 (±0.002)	0.624 (±0.002)	0.369 (±0.005)	0.426 (±0.002)	0.822 (±0.013)	61756 (±2073)
CIFAR100	Umap	—	0.402 (±0.202)	0.237 (±0.119)	0.501 (±0.169)	0.498 (±0.168)	0.504 (±0.170)	0.501 (±0.169)	0.254 (±0.116)	0.480 (±0.006)	0.686 (±0.011)	3690 (±211)
	Finsler Umap (Ours)	0.5	0.448 (±0.148)	0.261 (±0.087)	0.539 (±0.124)	0.534 (±0.123)	0.543 (±0.125)	0.539 (±0.124)	0.278 (±0.085)	0.451 (±0.013)	0.812 (±0.025)	4364 (±816)
	Finsler Umap (Ours)	0.1	0.410 (±0.206)	0.242 (±0.121)	0.507 (±0.172)	0.503 (±0.171)	0.511 (±0.173)	0.507 (±0.172)	0.260 (±0.119)	0.447 (±0.005)	0.798 (±0.022)	1639 (±100)
	Finsler Umap (Ours)	0.01	0.463 (±0.154)	0.274 (±0.092)	0.551 (±0.129)	0.546 (±0.127)	0.555 (±0.130)	0.551 (±0.129)	0.291 (±0.090)	0.449 (±0.007)	0.782 (±0.020)	1571 (±43)
	Finsler Umap (Ours)	0.001	0.462 (±0.154)	0.272 (±0.091)	0.551 (±0.128)	0.547 (±0.127)	0.555 (±0.129)	0.551 (±0.128)	0.289 (±0.088)	0.448 (±0.008)	0.778 (±0.019)	1692 (±100)
DTD	Umap	—	0.737 (±0.246)	0.389 (±0.130)	0.771 (±0.214)	0.800 (±0.222)	0.744 (±0.206)	0.771 (±0.214)	0.435 (±0.139)	0.677 (±0.006)	0.419 (±0.008)	154548 (±7934)
	Finsler Umap (Ours)	0.5	0.736 (±0.245)	0.383 (±0.128)	0.771 (±0.213)	0.798 (±0.221)	0.745 (±0.206)	0.771 (±0.213)	0.427 (±0.136)	0.643 (±0.010)	0.490 (±0.017)	103875 (±4468)
	Finsler Umap (Ours)	0.1	0.738 (±0.246)	0.383 (±0.128)	0.772 (±0.213)	0.801 (±0.221)	0.745 (±0.206)	0.772 (±0.213)	0.429 (±0.137)	0.652 (±0.010)	0.479 (±0.015)	77854 (±5631)
	Finsler Umap (Ours)	0.01	0.821 (±0.004)	0.432 (±0.016)	0.845 (±0.003)	0.875 (±0.003)	0.815 (±0.004)	0.845 (±0.003)	0.481 (±0.016)	0.651 (±0.007)	0.476 (±0.017)	77907 (±3926)
	Finsler Umap (Ours)	0.001	0.739 (±0.246)	0.393 (±0.131)	0.774 (±0.214)	0.802 (±0.222)	0.747 (±0.207)	0.774 (±0.214)	0.438 (±0.140)	0.649 (±0.011)	0.473 (±0.022)	74462 (±3758)
Caltech101	Umap	—	0.579 (±0.290)	0.366 (±0.183)	0.655 (±0.238)	0.658 (±0.239)	0.652 (±0.237)	0.655 (±0.238)	0.372 (±0.184)	0.590 (±0.005)	0.553 (±0.010)	150961 (±5464)
	Finsler Umap (Ours)	0.5	0.664 (±0.221)	0.435 (±0.145)	0.723 (±0.182)	0.725 (±0.183)	0.722 (±0.182)	0.723 (±0.182)	0.440 (±0.145)	0.568 (±0.007)	0.644 (±0.014)	51845 (±2257)
	Finsler Umap (Ours)	0.1	0.743 (±0.001)	0.487 (±0.009)	0.789 (±0.001)	0.791 (±0.001)	0.786 (±0.001)	0.789 (±0.001)	0.492 (±0.009)	0.590 (±0.005)	0.604 (±0.011)	55076 (±1848)
	Finsler Umap (Ours)	0.01	0.667 (±0.222)	0.434 (±0.145)	0.726 (±0.183)	0.729 (±0.183)	0.724 (±0.182)	0.726 (±0.183)	0.440 (±0.145)	0.586 (±0.007)	0.608 (±0.012)	54395 (±1912)
	Finsler Umap (Ours)	0.001	0.742 (±0.001)	0.488 (±0.008)	0.788 (±0.001)	0.790 (±0.001)	0.786 (±0.001)	0.788 (±0.001)	0.494 (±0.008)	0.588 (±0.005)	0.609 (±0.008)	54591 (±1419)
Caltech256	Umap	—	0.423 (±0.212)	0.315 (±0.158)	0.713 (±0.105)	0.707 (±0.104)	0.719 (±0.106)	0.713 (±0.105)	0.322 (±0.157)	0.483 (±0.007)	0.665 (±0.014)	2583 (±122)
	Finsler Umap (Ours)	0.5	0.571 (±0.005)	0.429 (±0.008)	0.785 (±0.002)	0.775 (±0.003)	0.775 (±0.003)	0.785 (±0.002)	0.437 (±0.007)	0.483 (±0.009)	0.722 (±0.019)	3652 (±526)
	Finsler Umap (Ours)	0.1	0.514 (±0.171)	0.386 (±0.129)	0.757 (±0.086)	0.749 (±0.085)	0.765 (±0.086)	0.757 (±0.086)	0.394 (±0.128)	0.459 (±0.007)	0.751 (±0.021)	1134 (±41)
	Finsler Umap (Ours)	0.01	0.517 (±0.171)	0.388 (±0.129)	0.758 (±0.086)	0.750 (±0.085)	0.767 (±0.086)	0.758 (±0.086)	0.396 (±0.128)	0.457 (±0.009)	0.756 (±0.021)	1014 (±42)
	Finsler Umap (Ours)	0.001	0.516 (±0.170)	0.389 (±0.129)	0.758 (±0.086)	0.751 (±0.085)	0.766 (±0.086)	0.758 (±0.086)	0.397 (±0.129)	0.461 (±0.006)	0.746 (±0.016)	1043 (±40)
OxfordFlowers102	Umap	—	0.720 (±0.362)	0.646 (±0.323)	0.735 (±0.342)	0.732 (±0.341)	0.739 (±0.344)	0.735 (±0.342)	0.656 (±0.315)	0.701 (±0.006)	0.426 (±0.024)	105243 (±5334)
	Finsler Umap (Ours)	0.5	0.885 (±0.005)	0.760 (±0.016)	0.892 (±0.005)	0.884 (±0.006)	0.899 (±0.005)	0.892 (±0.005)	0.768 (±0.015)	0.670 (±0.013)	0.478 (±0.040)	86351 (±6526)
	Finsler Umap (Ours)	0.1	0.805 (±0.269)	0.702 (±0.235)	0							

Table 7: Mean clustering performance using kMeans on t-SNE and Finsler t-SNE data embeddings across the smaller datasets. We use various levels of emphasis for metric asymmetry, via $\|\omega\|_2 \in \{0.001, 0.01, 0.1, 0.5\}$, in the embedding space of the Finsler methods. (+)/(-) signifies that higher/lower is better.

Dataset	Method	$\ \omega\ _2$	Label-related scores							Label-unrelated scores		
			AMI (+)	ARI (+)	NMI (+)	HOM (+)	COM (+)	V-M (+)	FMI (+)	SIL (+)	DBI (-)	CHI (+)
Iris	t-SNE	—	0,829	0,851	0,831	0,831	0,831	0,831	0,900	0,665	0,453	3028
	Finsler t-SNE (Ours)	0,5	0,845	0,868	0,846	0,846	0,847	0,846	0,911	0,664	0,465	4822
	Finsler t-SNE (Ours)	0,1	0,835	0,851	0,837	0,836	0,837	0,837	0,900	0,659	0,465	5092
	Finsler t-SNE (Ours)	0,01	0,835	0,851	0,837	0,836	0,837	0,837	0,900	0,670	0,442	5063
	Finsler t-SNE (Ours)	0,001	0,835	0,851	0,837	0,836	0,837	0,837	0,900	0,663	0,450	5263
DTD	t-SNE	—	0,498	0,288	0,581	0,578	0,584	0,581	0,303	0,402	0,804	2492
	Finsler t-SNE (Ours)	0,5	0,497	0,290	0,579	0,573	0,584	0,579	0,306	0,440	0,819	1268
	Finsler t-SNE (Ours)	0,1	0,502	0,298	0,584	0,582	0,587	0,584	0,313	0,430	0,826	1306
	Finsler t-SNE (Ours)	0,01	0,496	0,288	0,578	0,574	0,583	0,578	0,305	0,424	0,831	1208
	Finsler t-SNE (Ours)	0,001	0,504	0,294	0,585	0,580	0,590	0,585	0,310	0,408	0,859	1186
Caltech101	t-SNE	—	0,804	0,377	0,830	0,865	0,798	0,830	0,428	0,547	0,610	23151
	Finsler t-SNE (Ours)	0,5	0,824	0,441	0,847	0,878	0,818	0,847	0,490	0,576	0,627	13206
	Finsler t-SNE (Ours)	0,1	0,823	0,434	0,846	0,879	0,816	0,846	0,484	0,581	0,596	13901
	Finsler t-SNE (Ours)	0,01	0,825	0,458	0,848	0,879	0,820	0,848	0,506	0,584	0,597	13419
	Finsler t-SNE (Ours)	0,001	0,818	0,412	0,842	0,876	0,811	0,842	0,464	0,554	0,638	13707
OxfordFlowers102	t-SNE	—	0,549	0,388	0,775	0,767	0,783	0,775	0,397	0,419	0,740	1788
	Finsler t-SNE (Ours)	0,5	0,556	0,381	0,776	0,764	0,788	0,776	0,392	0,510	0,712	1452
	Finsler t-SNE (Ours)	0,1	0,563	0,380	0,779	0,766	0,792	0,779	0,392	0,537	0,653	1690
	Finsler t-SNE (Ours)	0,01	0,557	0,388	0,776	0,763	0,789	0,776	0,400	0,528	0,650	1677
	Finsler t-SNE (Ours)	0,001	0,558	0,388	0,776	0,764	0,789	0,776	0,400	0,527	0,656	172846
OxfordIIITPet	t-SNE	—	0,899	0,814	0,904	0,900	0,908	0,904	0,819	0,607	0,554	15824
	Finsler t-SNE (Ours)	0,5	0,900	0,822	0,906	0,903	0,908	0,906	0,827	0,600	0,606	13946
	Finsler t-SNE (Ours)	0,1	0,899	0,790	0,904	0,894	0,915	0,904	0,798	0,624	0,544	12501
	Finsler t-SNE (Ours)	0,01	0,903	0,821	0,908	0,904	0,913	0,908	0,826	0,618	0,556	13912
	Finsler t-SNE (Ours)	0,001	0,898	0,796	0,904	0,896	0,912	0,904	0,803	0,610	0,585	13367
Imagenette	t-SNE	—	0,939	0,946	0,939	0,939	0,939	0,939	0,951	0,610	0,536	22051
	Finsler t-SNE (Ours)	0,5	0,943	0,951	0,943	0,943	0,943	0,943	0,955	0,668	0,465	19651
	Finsler t-SNE (Ours)	0,1	0,937	0,944	0,937	0,937	0,937	0,937	0,950	0,696	0,451	19732
	Finsler t-SNE (Ours)	0,01	0,936	0,944	0,936	0,936	0,936	0,936	0,950	0,703	0,446	19678
	Finsler t-SNE (Ours)	0,001	0,936	0,944	0,936	0,936	0,936	0,936	0,949	0,706	0,443	19994